

https://dspace.org/

Electrochemical corrosion measurement of solid state sintered silicon carbide (SSiC) and liquid phase sintered silicon carbide (LPSSiC) ceramic materials

Andrews, Anthony

2006-11-15T07:25:47Z
http://hdl.handle.net/10539/1721

Downloaded from a DSpace repository. https://dspace.org/

ELECTROCHEMICAL CORROSION MEASUREMENT OF SOLID STATE SINTERED SILICON CARBIDE (SSiC) AND LIQUID PHASE SINTERED SILICON CARBIDE (LPSSiC) CERAMIC MATERIALS

Anthony Andrews

A dissertation submitted to the Faculty of Engineering and the Built Environment, University of the Witwatersrand, in fulfilment of the requirements for the degree of Master of Science in Engineering.

Johannesburg, 2005

DECLARATION

I declare that this dissertation is my own, unaided work. It is being submitted for the degree of Master of Science in the University of the Witwatersrand, Johannesburg. It has not been submitted before for any degree or examination in any other University.

_____

(Signature of candidate)

_____ day of _____ 2005.

ABSTRACT

Silicon carbide ceramics have many attractive properties, one of which is their high degree of corrosion resistance. Even though corrosion is slow, it does occur. Standard procedures for corrosion testing such as the immersion method is limited due to the low corrosion rates of most of these materials: it does not elucidate the mechanism of corrosion, but only gives the rate and degree of dissolution. Electrochemical techniques offer the possibility to further elucidate corrosion mechanisms and establish the resistance stability of conducting or partially-conducting ceramic materials, thus enhancing the understanding of ceramic material behaviour. In conjunction with microstructural changes, the electrochemical corrosion behaviour of solid state sintered silicon carbide (SSiC) and liquid phase sintered silicon carbide (LPSSiC) have successfully been studied at room temperature in acidic and alkaline environments by using potentiodynamic polarisation measurements. Several hypotheses were proposed to assist in establishing the effect of silicon and carbon on the corrosion mechanisms of these materials. The effect of the secondary phase on the electrochemical corrosion of the LPSSiC was also investigated. Corrosion current densities of the LPSSiC materials were much lower than the SSiC materials in all test solutions. The SSiC materials showed pseudo-passive behaviour in HCl and HNO_3, due to the formation of thin layer of SiO_2 on the surface. The carbon in the SiC compound increased the corrosion current densities in all test solutions for SSiC materials. The electrochemical corrosion of LPSSiC is due to the dissolution of SiC and not the oxides; the chemical attack on the oxide phases is mainly by acid-base type of reactions, rather than electrochemical corrosion involving redox reactions.

DEDICATION

I dedicate this work to my parents, brothers and sisters, Beatrice, and all my lovely friends.

ACKNOWLEDGEMENTS

I would humbly express my heartfelt gratitude to the following people who each, in their own special way, made it possible for this dissertation to be completed:

Dr. Michelle Sephton, for her time and patience during the supervision of this dissertation and for her expertise on the subject.

Dr. Mathias Herrmann, for his time, patience and dynamic input.

José Prozzi, for his time and input, especially in getting quality SEM micrographs.

Aubrey Xoseka, for his assistance during the preparation of my samples.

All other friends in the department (and those who have passed through) for making my stay there a pleasant and memorable one.

African Network of Scientific and Technological Institutions (ANSTI), for their funding of my studies in South Africa.

Mum and Dad, for their unconditional support and tolerance during times of despair. And to Bea, thank you for your reliability!

TABLE OF CONTENTS

DECLARATION II

ABSTRACT III

DEDICATION IV

ACKNOWLEDGEMENTS V

TABLE OF CONTENTS VI

LIST OF FIGURES IX

LIST OF TABLES XVI

LIST OF SYMBOLS AND ABBREVIATIONS XVII

CHAPTER 1 INTRODUCTION 1

CHAPTER 2 LITERATURE SURVEY 4

2.1 INTRODUCTION 4

2.2 SILICON CARBIDE MATERIALS 4

2.3 SINTERED SILICON CARBIDE CERAMICS 6

2.3.1 Solid state sintering 9

2.3.2 Liquid phase sintering 11

2.4 PROPERTIES OF SSIC AND LPSSIC MATERIALS 12

2.4.1 Physical Properties 12

2.4.2 Chemical Properties 15

2.5 AQUEOUS CORROSION OF SSIC AND LPSSIC CERAMICS 16

2.5.1 Forms of Corrosion in Ceramic Materials 18

2.5.2 Corrosion of SSiC and LPSSiC Materials by Immersion Technique 19

2.5.3 Corrosion of SiC-based Ceramics by Electrochemical Technique 20

2.6 ELECTROCHEMICAL TESTING TECHNIQUES 21

CHAPTER 3 EXPERIMENTAL PROCEDURE 24

3.1 INTRODUCTION 24

3.2 MATERIALS 24

3.3 Image Analyses 24
3.4 Electrochemical Corrosion Measurements 25
3.5 Inductively Coupled Plasma Optical Emission Spectrometer 27

CHAPTER 4 MATERIAL CHARACTERISATION 28

4.1 Introduction 28
4.2 Material Compositions 28
4.3 Microstructural Analysis of SSiC Material (as-sintered) 29
4.4 Microstructural Analysis of LPSSiC Materials (as-sintered) 30

CHAPTER 5 CORROSION OF SOLID STATE SINTERED SILICON CARBIDE (SSIC) 34

5.1 Introduction 34
5.2 Electrochemical Behaviour 34
5.2.1 Corrosion behaviour in HCl 34
5.2.2 Corrosion behaviour in HNO_3 36
5.2.3 Corrosion behaviour in NaOH 38
5.2.4 Corrosion behaviour in distilled water 39
5.3 Corrosion Mechanisms of SSiC 42
5.3.1 Effect of Carbon 43
5.3.2 Effect of Silicon 54
5.3.3 Investigation of the Formation of SiO_2 / SiO_3^{2-} 60
5.4 Conclusion 63

CHAPTER 6 CORROSION OF LIQUID PHASE SINTERED SILICON CARBIDE (LPSSIC) 66

6.1 Introduction 66
6.2 Electrochemical Behaviour 66
6.2.1 Corrosion behaviour in HCl 66
6.2.2 Corrosion behaviour in HNO_3 69
6.2.3 Corrosion behaviour in NaOH 72
6.2.4 Corrosion behaviour in distilled water 75
6.3 Corrosion Mechanisms of LPSSiC Materials 79

6.3.1 Effect of the Secondary Phase *80*
6.4 Relative Dissolution of the Secondary Phase and the Silicon Carbide Phase 86
6.5 Conclusion 90
CHAPTER 7 SUMMARY 93
REFERENCES 95
APPENDIX A 98
Thermodynamic calculations of standard potentials of the cell reactions 98
APPENDIX B 103
The results of the surface composition of SSiC with SXPS 103

LIST OF FIGURES

Figure 2.1 Microstructurual changes that occur during firing of a powder compact. (a) Powder particles after pressing, (b) Particle coalescence and pore formation sintering begins, (c) As sintering proceeds, the pores change size and shape (adapted from German, 1996). 8

Figure 2.2 Schematic diagram of electrical resistivity of SiC material as a function of temperature (after Pelissier *et al*., 1998) 14

Figure 2.3 Three major classification schemes of corrosion of materials (Nickel, 1997) 17

Figure 2.4 Schematic potentiodynamic polarisation measurement setup diagram (after Jones, 1996) 22

Figure 2.5 Typical Tafel plot from polarisation experiment (ASTM G3 - 89)..... 23

Figure 3.1 Schematic diagram of the setup used for the potentiodyanmic polarisation tests..... 26

Figure 4.1 Secondary electron SEM micrograph of a polished section of SSiC (as-sintered). The following features are marked: (A) silicon carbide (light gray phase), (B) carbon inclusions (gray phase), and (C) porosity (dark areas)..... 29

Figure 4.2 XRD pattern of SSiC (as-sintered) showing residual carbon in the sample. The enlargement of peak "A" is shown in the insert. 30

Figure 4.3 Secondary electron SEM micrograph of a polished section of LPSSiC-1 (as-sintered). The following features are marked: (A) silicon carbide (light gray phase) and (B) secondary phases (white). 31

Figure 4.4 Secondary electron SEM micrograph of a polished section of LPSSiC-2 (as-sintered). The following features are marked: (A) silicon carbide (light gray phase), (B) secondary phase (white), and (C) porosity (dark areas). 31

Figure 4.5 XRD pattern of LPSSiC-1 (as-sintered) showing the different phases in the sample: 1- SiC modification; 2 - yttrium aluminate (YAG); 3 - alminium yttrium oxide ($Al_2Y_4O_9$). 32

Figure 4.6 XRD pattern of LPSSiC-2 (as-sintered) showing the different phases in the sample: 1 – SiC modification; 2 - yttrium aluminate (YAG); 3 - alumina (Al_2O_3). 33

Figure 5.1 Potentiodynamic polarisation scans of SSiC in 1 M HCl showing good reproducibility. Pseudo-passivity was observed at approximately +160 mV. The average corrosion current density is ~46 $\mu A/cm^2$. 35

Figure 5.2 Secondary electron SEM micrograph of SSiC after full potentiodynamic scan in 1 M HCl showing no significant surface damage. The following features are marked: (A) residual carbon and (B) porosity. 36

Figure 5.3 Potentiodynamic polarisation scans of SSiC in 1 M HNO_3 showing very good reproducibility. The average corrosion current density is ~58 $\mu A/cm^2$. . 37

Figure 5.4 Secondary electron SEM micrograph of SSiC after full potentiodynamic scan in 1 M HNO_3 showing no significant surface damage. The following features are marked: (A) residual carbon and (B) porosity. 37

Figure 5.5 Potentiodynamic polarisation scans of SSiC in 1 M NaOH showing good reproducibility. The average corrosion current density is ~33 $\mu A/cm^2$. 38

Figure 5.6 Secondary electron SEM micrograph of SSiC after full potentiodynamic scan in 1 M NaOH showing some surface damage around the porosities. The following features are marked: (A) residual carbon and (B) porosity 39

Figure 5.7 Potentiodynamic polarisation scans of SSiC in distilled water showing very good reproducibility. The average corrosion current density is ~3 $\mu A/cm^2$. 40

Figure 5.8 Secondary electron SEM micrograph of SSiC after full potentiodynamic scan in distilled water showing no surface damage. The following features are marked: (A) residual carbon and (B) porosity. 40

Figure 5.9 Average corrosion current densities of SSiC sample in different corrosive media. The slight shift in E_{corr} has not been accounted for in the graph above. . 41

Figure 5.10 Potentiodynamic polarisation scans of SSiC in 1 M HNO_3. Samples were held at +500 mV for 5, 10, 20, 30, and 60 minutes respectively and compared to

a normal scan in HNO_3 (without holding) showing decreasing corrosion current density as the holding time is increased. 44
Figure 5.11 Comparison of the corrosion current densities of SSiC in 1 M HNO_3 at different holding times. The corrosion current density decreased as holding time increased. 44
Figure 5.12 Secondary electron SEM micrograph of SSiC after full potentiodynamic scan in 1 M HNO_3. Before scan, the working electrode was held at +500 mV for 20 minutes. The following features are marked: (A) residual carbon and (B) porosity 45
Figure 5.13 Secondary electron SEM micrograph of SSiC after full potentiodynamic scan in 1 M HNO_3. Before scan, the working electrode was held at +500 mV for 60 minutes. The following features are marked: (A) residual carbon and (B) porosity 45
Figure 5.14 XRD pattern of SSiC before and after holding the sample in 1 M HNO_3 at +500 mV for 20 minutes before performing full potentiodynamic scan. The enlargement of peak "A" is shown in the insert. There was no change in the intensity (height) of the residual carbon 47
Figure 5.15 Raman spectra of SSiC (as-sintered) before corrosion. SiC-A: 50x objective, 0.5mm pinhole on "clear" area in microscope; SiC-B: same spot as SiC-A, different spectral region; SiC-C: same spot as SiC-A, different spectral region. 48
Figure 5.16 Raman spectra of SSiC after holding at +500 mV (vs. SCE) in 1 M HNO_3 for 60 minutes before polarisation scan. SiC-H: 50x objective, 0.5mm pinhole on "clear" area in microscope; SiC-I: same spot as SiC-H, different spectral region; SiC-J: same spot as SiC-H, different spectral region. 48
Figure 5.17 Raman spectrum at 50x objective on SSiC (black inclusion) after holding at +500 mV (vs. SCE) in 1 M HNO_3 for 60 minutes. 49
Figure 5.18 Potentiodynamic polarisation scans of SSiC in 1 M HCl showing good reproducibility. The electrolyte was de-aerated with CO_2 gas. Pseudo-passivity was observed at approximately +160 mV. 50

Figure 5.19 Potentiodynamic polarisation scans of SSiC in 1 M HCl indicating approximately the same corrosion current density and open circuit potential when de-aerating with N_2 or CO_2 gas. 51

Figure 5.20 Potentiodynamic polarisation scans of SSiC in 1 M NaOH/Na_2CO_3 showing good reproducibility. 52

Figure 5.21 Comparison of potentiodynamic polarisation scans of SSiC in 1 M NaOH and 1 M NaOH/Na_2CO_3 indicating lower corrosion current density and a slightly positive shift in open circuit potential when Na_2CO_3 is dissolved in NaOH. 53

Figure 5.22 Potentiodynamic polarisation scans of SSiC and pure Si in 1 M HCl showing higher corrosion current density for SSiC material. 54

Figure 5.23 Potentiodynamic polarisation scans of SSiC and pure Si in 1 M HNO_3 showing higher corrosion current density for SSiC material. 55

Figure 5.24 Potentiodynamic polarisation scans of SSiC and pure Si in 1 M NaOH showing higher corrosion current density for SSiC material. 55

Figure 5.25 Comparison of potentiodynamic polarisation scans of SSiC in the different corrosive media. 56

Figure 5.26 Comparison of potentiodynamic polarisation scans of Si in the different corrosive media. 57

Figure 5.27 An approximate potential-pH equilibrium diagram for the system silicon-water, at 25^{o}C, considering SiO_2 in the form of quartz (Pourbaix *et al*., 1958).. 58

Figure 5.28 Influence of pH on the solubility of SiO_2 at 25^{o}C. a, quartz; b, cristobalite; c, tridymite; d, vitreous silica; e, amorphous silica (Pourbaix *et al*., 1958) 59

Figure 5.29 Potentiodynamic polarisation scans of SSiC in 1 M HNO_3. Samples were held at +500 mV for 20 and 30 minutes, respectively and compared to a normal scan in 1 M HNO_3 (without holding). A sample was also held at +500 mV for 30 minutes in 1 M HNO_3, followed by 10 minutes immersion in HF, before performing a full scan. 61

Figure 5.30 Potentiodynamic polarisation scans of SSiC in 1 M NaOH. Samples were held at +500 mV for 30 minutes and compared to a normal scan in HNO_3 (without holding)..... 62

Figure 6.1 Potentiodynamic polarisation scans of LPSSiC-1 in 1 M HCl showing good reproducibility. The average corrosion current density is ~2 $\mu A/cm^2$ . .. 67

Figure 6.2 Secondary electron SEM micrograph of LPSSiC-1 after full potentiodynamic scan in 1 M HCl. Corrosion is visible at the secondary phase. 67

Figure 6.3 Potentiodynamic polarisation scans of LPSSiC-2 in 1 M HCl. Corrosion potential is not reproducible; however, the corrosion current densities are approximately the same. The average corrosion current density is ~0.07 $\mu A/cm^2$ 68

Figure 6.4 Secondary electron SEM micrograph of LPSSiC-2 after full potentiodynamic scan in 1 M HCl. Corrosion is visible at the secondary phase. 68

Figure 6.5 Potentiodynamic polarisation scans of LPSSiC-1 in 1 M HNO_3. Corrosion potential is not reproducible and shifts are unpredictable. However, the corrosion current densities are approximately the same. The average corrosion current density is ~6 $\mu A/cm^2$ 70

Figure 6.6 Secondary electron SEM micrograph of LPSSiC-1 after full potentiodynamic scan in 1 M HNO_3. Corrosion is visible at the secondary phase..... 71

Figure 6.7 Potentiodynamic polarisation scans of LPSSiC-2 in 1 M HNO_3. Corrosion potential shifts to more active values with each scan. However, the corrosion current densities are approximately the same. The average corrosion current density is ~0.09 $\mu A/cm^2$ 71

Figure 6.8 Secondary electron SEM micrograph of LPSSiC-2 after full potentiodynamic scan in 1 M HNO_3. Corrosion is visible at the secondary phase..... 72

Figure 6.9 Potentiodynamic polarisation scans of LPSSiC-1 in 1 M NaOH. Corrosion potential shifts, but corrosion current densities are nearly the same. The average corrosion current density is ~1.8 $\mu A/cm^2$ 73

Figure 6.10 Secondary electron SEM micrograph of LPSSiC-1 after full potentiodynamic scan in 1 M NaOH. Corrosion at the secondary phase is less than in 1 M HCl. 73

Figure 6.11 Potentiodynamic polarisation scans of LPSSiC-2 in 1 M NaOH. Corrosion potential shifts with each scan, however, corrosion current densities are similar. The average corrosion current density is ~0.06 $\mu A/cm^2$ 74

Figure 6.12 Secondary electron SEM micrograph of LPSSiC-2 after full potentiodynamic scan in 1 M NaOH. Corrosion at the secondary phase is less than for LPSSiC-1. 74

Figure 6.13 Potentiodynamic polarisation scans of LPSSiC-1 in distilled water. Corrosion potential shifts to more active values with subsequent scans on the same sample re-polished. However, the corrosion current densities are nearly the same. The average corrosion current density is ~0.2 $\mu A/cm^2$ 75

Figure 6.14 Secondary electron SEM micrograph of LPSSiC-1 after full potentiodynamic scan in distilled water. 76

Figure 6.15 Potentiodynamic polarisation scans of LPSSiC-2 in distilled water. Corrosion potential shifts to more active values with subsequent scans on the same sample re-polished. However, the corrosion current densities are nearly the same. The average corrosion current density is ~0.07 $\mu A/cm^2$ 76

Figure 6.16 Secondary electron SEM micrograph of LPSSiC-2 after full potentiodynamic scan in distilled water. 77

Figure 6.17 Comparison of average corrosion current densities of LPSSiC-1 and LPSSiC-2 samples in different corrosive media. The shifts in the E_{corr} were not accounted for in the calculation of the average i_{corr}. 78

Figure 6.18 Secondary electron SEM micrograph of LPSSiC-1 after holding at +300 mV (vs. SCE) in 1 M HCl for 10 minutes. 81

Figure 6.19 Secondary electron SEM micrograph of LPSSiC-1 after immersion in 1 M HCl for 10 minutes showing about the same corrosion damage at the secondary phase as with 10 minutes hold at +300 mV (vs. SCE). 81
Figure 6.20 Secondary electron SEM micrograph of LPSSiC-1 after holding at +300 mV (vs. SCE) in 1 M HCl for 30 minutes. 82
Figure 6.21 Secondary electron SEM micrograph of LPSSiC-1 after immersion in 1 M HCl for 30 minutes showing about the same corrosion damage at the secondary phase as with 30 minutes hold at +300 mV (vs. SCE). 82
Figure 6.22 Potentiodynamic polarisation scans of LPSSiC-1 in 1 M HCl and 1 M HCl/YCl_3. Corrosion current densities are about the same. 84
Figure 6.23 Secondary electron SEM micrograph of LPSSiC-1 after full potentiodynamic scan in 1 M HCl/YCl_3. The secondary phase is attacked to a lesser extent than after exposure to 1 M HCl. 85
Figure 6.24 Potentiodynamic polarisation scans of LPSSiC-2 in 1 M HCl and 1 M HCl/YCl_3 mixture. Corrosion current densities are about the same. 85
Figure 6.29 Comparison of dissolved ion concentration of Si, Al, and Y after full potentiodynamic scan on LPSSiC-1 and LPSSiC-2 in 1 M HCl. 87
Figure 6.30 Comparison of dissolved ion concentration of Si, Al, and Y after full potentiodynamic scan on LPSSiC-1 and LPSSIC-2 in 1 M NaOH. 87
Figure 6.31 XRD pattern comparison of the LPSSiC-1 before and after corrosion in 1 M HCl. 1–SiC; 2–yttrium aluminate (YAG); 3–aluminium yttrium oxide ($Al_2Y_4O_9$) 89

LIST OF TABLES

Table 2.1 Physical properties of sintered silicon carbide (SSiC) and liquid phase sintered silicon carbide (LPSSiC) ceramics (after Schwetz, 2000) 15

Table 3.1 X-ray diffractometer parameters used for the analyses of the samples 25

Table 4.1 Material compositions of both SSiC and LPSSiC. The porosity and volume percent of binder were measured in this investigation using Image Tool© (version 3) 29

Table 5.1 Summary of polarisation results of SSiC and Si materials 64

Table 6.1 Ratio (R) at different peaks before and after corrosion of LPSSiC-1 in 1 M HCl 90

Table 6.2 Summary of the polarisation results of LPSSiC-1 and LPSSiC-2, compared to SSiC 91

LIST OF SYMBOLS AND ABBREVIATIONS

(g) ……in the gaseous state

(*l*) ……in the liquid state

(s) …… in the solid state

ASTM ……American Society of Testing and Materials

CE ……...counter electrode

DW ……distilled water

e^- ……an electron

E_{corr} ……open circuit potential, mV

i_{corr} ……corrosion current density, $\mu A / cm^2$

LPSSiC ……...liquid phase sintered silicon carbide

M ……molar, a non-SI unit of concentration (= 10^3 mol m^{-3})

SCE ……....saturated calomel electrode

SEM ……...scanning electron microscopy

SSiC ……...sintered silicon carbide

RBSiC ……....Reaction bonded silicon carbide

XRD ……..X-ray diffractometry

SXPS……...scanning X-ray photoelectron spectroscopy

CHAPTER 1

INTRODUCTION

Ceramic materials have many attractive properties which make them appropriate for structural applications. Structural ceramics are widely used in areas where their high hardness and wear resistance are necessary (e.g. bearings, seals, valves, and linings in chemical equipment). One other outstanding advantage which ceramic materials have over the other materials is their high degree of corrosion resistance (Cook *et al*., 1994; Fett, 1999; Herrmann *et al*., 2003; Liu, 1997; Magnani *et al*., 2000; Morrell, 1985; Nickel, 1997; Pelissier *et al*., 1998; Schwetz, 2000; Steen and Ranzani, 2000). However, even though corrosion is slow, it does occur. The corrosion behaviour of ceramics is very sensitive to composition and microstructure: even impurities of less than 0.1 % can increase the corrosion rate by more than an order of magnitude (Cook *et al*., 1994; Herrmann *et al*., 2003; Liu, 1997; Nickel, 1997).

The standard procedure for corrosion testing of ceramic materials is by immersion method. The corrosion behaviour is explained by immersing the samples in a media and measuring the weight loss, the corrosion layer depth, residual strength, and sometimes the concentration of the corroded ions in the media (Cook *et al*., 1994; Bellosi *et al*., 2001; Herrmann *et al*., 2003; Nickel and Seipel, 2003; Sharkawy and El-Aslabi, 1998). This method is limited due to the low corrosion rates of most of these materials (Cook *et al*., 1994; Herrmann *et al*., 2003; Schwetz, 2000). Another limitation of this method is that it does not elucidate the mechanism of corrosion; it only gives the rate and degree of dissolution (Cook *et al*., 1994; Herrmann *et al*., 2003). On the other hand, the technique is simple and straightforward and does not require any knowledge of the corrosion reactions that are occurring to determine whether the material is suitable for application or not.

Electrochemical methods are often used to determine corrosion behaviour of metals and hardmetals, but are hardly ever used for the analysis of ceramic materials. However, these techniques can also be used to measure the corrosion behaviour of ceramics as long as the ceramics remain electrically conducting (Cook *et al*., 1994). These methods offer the possibility to further elucidate corrosion mechanisms and stability of conducting or partially-conducting ceramic materials, thus enhancing the understanding of ceramic material behaviour.

Electrochemical corrosion of solid state sintered silicon carbide (SSiC) and reaction bonded silicon carbide (RBSiC) have been studied at room temperature by Cook *et al*. (1994) and Divakar *et al*. (1989) in various dilute acids (HCl, HNO_3, HF, H_2SO_4 and H_3PO_4). The investigations by Cook *et al*. (1994) showed that SSiC and RBSiC are passive in acidic environments because of the formation of a surface silica film. HF is an exception though, because the silica is dissolved. For RBSiC, the residual silicon was preferentially corroded. It is believed that the Si atoms present in RBSiC are responsible for the corrosion behaviour. The principal corrosion reaction of SSiC was assumed to be the dissolution of Si atoms; 1 mol of silicon removal meant removal of 1 mol of SiC. However, there is the possibility of the residual carbon in SSiC dissolving out, accompanied by the liberation of electrons and therefore contributing to the corrosion behaviour measured. The corrosion mechanisms were not investigated in alkaline environments (that is, the effect of OH^- ions). If silicon is responsible for the corrosion behaviour of SSiC obtained by Cook *et al*., and Divakar *et al*., then in alkaline environments, silicate ions would be formed (Antelman, 1982; Bard *et al*., 1985; Pourbaix *et al*., 1958); and no passivity feature should be observed in alkaline environments. Because some aspects regarding the corrosion mechanisms of SiC ceramic materials are still unclear, the following questions were posed:

1. Is the corrosion behaviour of SSiC due to the electrochemical dissolution of Si atoms or is it due to both Si atoms and the C present?

2. Can electrochemical techniques be used to establish the corrosion mechanisms for liquid phase sintered silicon carbides (LPSSiC) materials?

The following objectives were identified to answer these questions:

1. Establishment of the possibility of using electrochemical techniques.
2. Determination of the corrosion mechanisms of SSiC and LPSSiC ceramic materials by electrochemical techniques.
3. Determination of the possible effect of the secondary phases on the electrochemical corrosion of LPSSiC in different environments.
4. Prediction of the stability of SiC materials consisting of conducting and non-conducting phases in corrosive environments.

To achieve these objectives, a brief literature survey was conducted (see Chapter 2) where the different types of SiC ceramics as well as their properties and applications were outlined; and previous work on the corrosion of SSiC and LPSSiC pointed out. The experimental procedures that were designed to address the objectives are given in Chapter 3. These included potentiodynamic polarisation scans, scanning electron microscopy (SEM), and X-ray diffractometry analyses (XRD). The materials, before corrosion experiments, were characterised based on material composition and microstructures, and a detailed report is given in Chapter 4. The results of the investigations on the corrosion of SSiC and LPSSiC, as well as the conclusions are given in Chapters 5, 6 and 7, respectively.

CHAPTER 2

LITERATURE SURVEY

2.1 Introduction

Ceramics are conventionally defined as inorganic non-metallic, man-made materials, generally of high melting point. The field covers oxide and non-oxide refractories, glasses, hydraulic cements, "traditional" clay-based systems, and fined-grain, polycrystalline materials usually used for their strength, hardness, wear resistance, or a wide spectrum of electromagnetic and optical properties (McCauley, 1995). From the engineering point of view, brittleness is the reason why designers and engineers act very cautiously when the possibility of using a ceramic arises. On the bases of application, ceramic materials can be grouped into clay products, refractories, abrasives and advance ceramics (Fett, 1999). SiC-based ceramics are classified under advanced ceramics.

2.2 Silicon Carbide Materials

Silicon carbide materials can be produced by sintering and the products are classified as follows:

- **Pressureless Sintered Silicon Carbide (SSiC)**
  Pressureless sintered silicon carbide is produced by high-temperature firing of silicon carbide powder with a suitable dopant such as boron and carbon to enhance the slow sintering mechanism (German, 1996; Morrell, 1985; Rahaman, 2003). Solid state sintered silicon carbide and liquid phase sintered silicon carbide ceramics are classified under this group of materials. The dopant added enhances the sintering process at the grain boundaries. Both the high-temperature stable phase (alpha-SiC) and the low-temperature stable

phase (beta-SiC) could be used for sintering. The beta-SiC transforms to alpha-SiC at sintering temperatures higher than 2000^{o}C (Lee *et al*., 1998; Magnani *et al*., 2000). The transformation, which is accompanied by grain growth of the alpha phase, depends on the firing temperature as well as the dopant level. This group of materials is further discussed in Section 2.3

- **Reaction Bonded Silicon Carbide (RBSiC)**

  Reaction-bonded silicon carbide is produced at relatively low temperatures – up to 2000^{o}C (German, 1996; Morrell, 1985; Rahaman, 2003; Schwetz, 2000). They are made by pressing a powder compact of silicon carbide powder, carbon and a temporary binder. The elemental carbon in the preform is then reacted with gaseous liquid silicon. Thus, the binder in the pressed shape is carbonised and the porous body subjected to liquid silicon, silicon vapour or silicon monoxide vapour. The silicon reacts with the carbon to produce SiC which is deposited on the pre-existing grains (German, 1996; Rahaman, 2003; Schwetz, 2000).

- **Hot Pressed Silicon Carbide (HPSiC)**

  Hot pressed silicon carbide is manufactured by pressing and firing at the same time. Hot pressed silicon carbide is produced by addition of a small amount of secondary material, usually an oxide, to the starting material (German, 1996; Morrell, 1985; Rahaman, 2003). In axial hot-pressing with graphite tools it is necessary to use small amounts of sintering aids. The pressure that is used is limited by the strength of the graphite, the maximum being 50 MPa (Schwetz, 2000). The secondary material is deformable at the hot-pressing temperature (1900 - 2000^{o}C) and a suitable refractory for subsequent use of the product. HPSiC is fine-grained, has essentially zero porosity, and is hard and strong (German, 1996; Schwetz, 2000).

- **Hot Isostatically Pressed Silicon Carbide (HIPSiC)**

  Powder is put in a flexible rubber mould and then hydrostatically compressed in a fluid (normally oil) to give uniform compaction through the body (German, 1996). Higher relative densities can be obtained if pressure is applied at the same time as heating. This is useful for materials which are difficult to sinter because of intrinsically low diffusion coefficients. SiC is an example of such materials. In hot isostatic pressing the pressure is provided by a high-pressure gas. The primary control parameters are pressure, temperature and time (German, 1996).

  The post-densification of SSiC or LPSSiC by hot isostatic pressing is less complicated because no gas-tight encapsulation is necessary. It is also possible to achieve 99% theoretical density; the variation of density and strength can also be reduced by this method (Schwetz, 2000).

2.3 Sintered Silicon Carbide Ceramics

One of the concerns in the application of ceramic materials is the fabrication process (German, 1996). Unlike ceramics, many of the metal fabrication processes rely on casting and/or other techniques that involve plastic deformation. Ceramic materials have high melting temperatures; hence casting them becomes mostly impracticable. In addition to the problems associated with casting, the brittleness of ceramic materials prevents plastic deformation. SiC ceramic materials are therefore produced from powders. The sintering process improves the microstructure and properties of the fabricated material (Fett, 1999; German, 1996; Morrell, 1985; Rahaman, 2003).

Sintering involves mechanisms of mass transport between particles which lead to porosity elimination, together with shrinkage of the overall body (Schwetz, 2000). Densification is the change in volume divided by the initial volume of the material. Three mechanisms of transport have been identified in densification: surface transport, bulk transport and gas phase transport (German, 1996). Surface transport processes produce neck growth without densification due to mass flow originating and terminating at the particle surface. The factors that contribute to the surface transport mechanism are surface diffusion and evaporation-condensation reactions.

The bulk transport mechanisms include volume diffusion, grain boundary diffusion, plastic flow and viscous flow. For most materials the gas phase transport contributions are small and are often ignored (German, 1996). Generally, one of these mechanisms is predominant at any given stage in the sintering process.

The composition of a ceramic and the microstructure produced by the fabrication method are important in determining the properties and performance, just as with metallic materials (German, 1996; Morrell, 1985). However, unlike the case with metals, the microstructure cannot be changed by plastic working either at room temperature or at elevated temperatures.

During fabrication of SiC ceramics, many of the powder particles touch one another and initially necks form along the contact regions between adjacent particles. In addition, a grain boundary forms within each neck and every interstice between particles become a pore. These pores become smaller and spherical in shape during sintering (German, 1996; Rahaman, 2003). The mechanism of sintering is shown in figure 2.1.

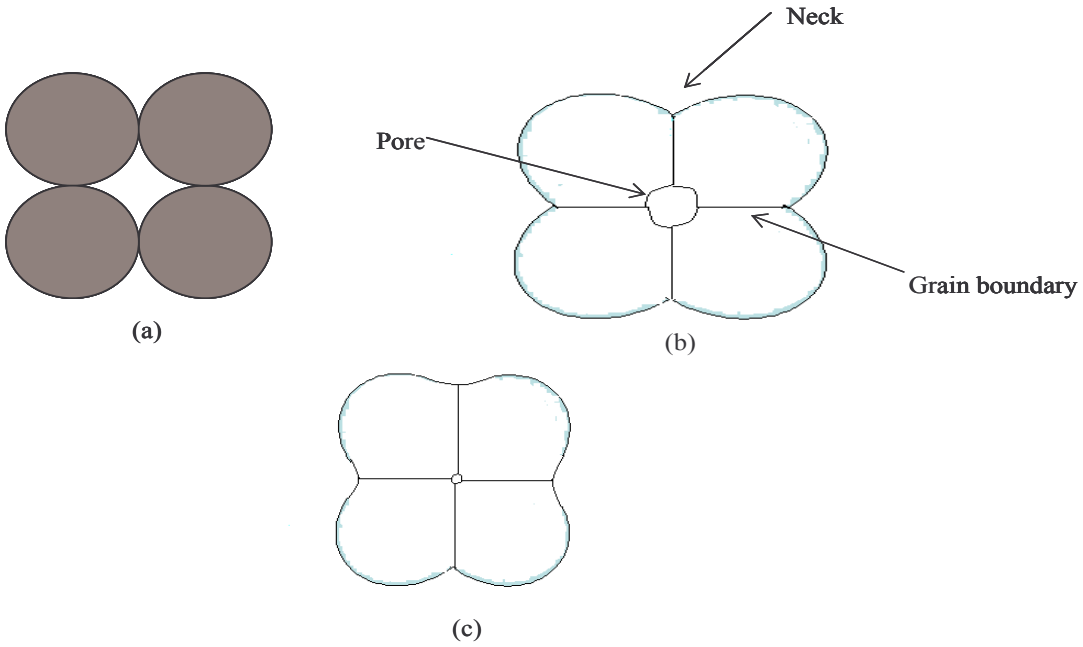


Figure 2.1 Microstructurual changes that occur during firing of a powder compact. (a) Powder particles after pressing, (b) Particle coalescence and pore formation sintering begins, (c) As sintering proceeds, the pores change size and shape (adapted from German, 1996).

Silicon carbide, after fabrication, exhibits a large number of different structures. The high temperature stable phase of silicon carbide, alpha-SiC, is crystallographically hexagonal and it is produced by reduction of silica sand by carbon in an arc furnace. It exists in a number of forms with various stacking arrangements of atomic planes. These can be classified into hexagonal and rhombohedral crystal systems (i.e. 6H, 15R and 4H). Beta-SiC is crystallographically cubic, and is produced by low-temperature vapour phase reactions. Fabrication processes with temperature exceeding 2000^{o}C transforms beta-SiC to alpha-SiC. Silicon carbide is very refractory, only tending to dissociate at temperatures above 2500^{o}C (Morrell, 1985).

Since certain mechanisms of mass transport can dominate in some systems, two categories of sintering can be identified:

1. Solid state sintering, where all densification is achieved through changes in particle shape, without particle rearrangement or the presence of liquid.
2. Liquid phase sintering, where liquid present at sintering temperatures aids compaction. In this case, grain rearrangement occurs.

2.3.1 Solid state sintering

The special properties of SiC-based ceramic materials are due to their highly covalent bonding. The covalent bonding makes it difficult to achieve densification in SiC-based ceramics and other non-oxide covalent compounds (Si_3N_4 and AlN) during sintering. However, unlike Si_3N_4 and AlN which tend to decompose severely at elevated temperatures, SiC has the advantage of being densified at elevated temperatures, without decomposing, through the solid state sintering process.

Sintering is carried out in an inert atmosphere or in a vacuum at elevated temperatures between 1900^{o}C and 2100^{o}C with the aid of boron (B) and carbon (C). Aluminium and aluminium compounds or beryllium and its compounds are sometimes used instead of boron, the net results being the same (German, 1996; Morrell, 1985; Rahaman, 2002; Schwetz, 2000; Stobierski and Gubernat, 2003a). As the sintering temperature increases to about 1400^{o}C, the excess addition of carbon ensure complete de-oxidation, that is the removal of the SiO_2 film from the silicon carbide grain (Schwetz, 2000; Stobierski and Gubernat, 2003a; Stobierski and Gubernat, 2003b). The addition of excess carbon also inhibits grain growth and produces a more equiaxed grain structure.

In the carbon-free samples, the presence of SiO_2 reacts with SiC during sintering at about 1500 to 1700^{o}C as follows:

$$2SiO_2(s) + SiC(s) = 3SiO(g) + CO(g) \quad [2.1]$$

Thus, silicon monoxide and carbon monoxide evaporate from the system. This could cause some damage on the quality of sintered bodies because of the gas-producing reaction between SiC and SiO_2 at high temperatures. It could also cause an increase in weight loss and can reduce density. This implies that the quantity of SiO_2 in the SiC should be kept as low as possible (Magnani *et al.*, 2000). The presence of carbon removes SiO_2 from the surface of SiC according to:

$$SiO_2 + 3C = SiC + 2CO \quad [2.2]$$

In this case only carbon monoxide is transferred to the gaseous phase. This reduces the defects present at the surface, as a result of the violent reaction between SiC and SiO_2, and diffusion along the surface decreases resulting in densification of SiC.

The other dopant added during sintering of SiC is boron or aluminium and its compounds. The effect of this additive is believed to take place in two stages: transient liquid phase sintering which enables the involvement of the capillary forces in densification process, followed by solid state sintering during the final stage (Schwetz, 2000).

During the sintering process, beta–SiC (low-temperature modification) transforms to alpha–SiC (high-temperature modification) with associated grain growth. This transformation depends on the type and the amount of sintering additives, as well as sintering temperature. The driving force for the sintering process is the decrease in surface free energy of the powdered compacts. However, solid state sintering of SiC ceramics have poor, or at the best, moderate mechanical properties: flexural strength of 300-450 MPa and fracture toughness of 2.5-4 $MPa.m^{-1/2}$ (Magnani *et al.*, 2000; Schwetz, 2000).

Applications of SSiC

SSiC has the following uses (Fett, 1999; Schwetz, 2000):

- Modern mechanical seals in the form of slide rings due to its corrosion, wear, and thermal shock resistance
- Sliding bearings due to its erosion and chemical resistance
- Radiant tubes in indirect gas-fired heat treating operations
- Heat exchanger systems because of its high-thermal conductivity and corrosion resistance
- Heating elements due to its low electrical resistivity at high temperatures ≤ 1600^{o}C and low porosity.

2.3.2 Liquid phase sintering

One problem usually encountered in solid state sintering is that coarsening may dominate the densification process, with the result that high densities are mostly difficult to achieve (German, 1996; Rahaman, 2003). This can be remedied in the liquid state sintering by adding additives that form small amounts of liquid phase between the grains at sintering temperatures. Y_2O_3-Al_2O_3 or Y_2O_3-AlN based compounds have been found to be the most effective densifying aids (Schwetz, 2000).

The liquid phase provides high diffusivity paths for transport of matter into the pores to produce densification. Compared with SSiC, liquid phase sintering produces an increase in fracture toughness to 6.0 MPa.m$^{-1/2}$ and an increase in flexural strength to more than 700 MPa (Schwetz, 2000). The major part of the secondary phase is YAG (yttrium aluminium garnet, $Y_3Al_5O_{12}$) which crystallises together with re-precipitated SiC on solidification from the liquid (Schwetz, 2000). Liquid phase sintering of SiC can be achieved at much lower temperatures (1800 – 1900^{o}C) than solid state sintering (Schwetz, 2000). Large pores can occur in liquid phase sintered SiC and are attributed to the loss of additives (e.g. alumina) according to the reaction:

$$SiC(s) + Al_2O_3(s) \Leftrightarrow Al_2O(g) + SiO(g) + CO(g) \quad [2.3]$$

This reaction can lead to some weight loss of SiC material. The reaction increases with high alumina content and temperature of sintering (Izhevskyi, 2000; Magnani *et al*., 2000).

Applications of LPSSiC

LPSSiC has the following uses (Schwetz, 2000):

- Dewatering elements in the paper industry and as rings for highly stressed gas seals
- Neutral matrix in ceramic matrix composites containing plutonium to burn the world's stockpiles of military plutonium in thermal or fast reactors.

2.4 Properties of SSiC and LPSSiC Materials

Ceramic materials have many attractive properties which make them appropriate for structural applications. This section aims at giving a general overview of the physical and chemical properties of solid state sintered silicon carbide and liquid phase sintered silicon carbide ceramic materials.

2.4.1 Physical Properties

Electrical Properties

Ceramics exhibit the largest possible range in electrical conductivity in terms of type and magnitude of conductivity (Schwetz, 2000). Electrical conduction in ceramic materials can result from a number of different mechanisms, depending on the type of material (Morrell, 1985). It can occur by the conduction of electrons, as in semiconducting ceramics such as SiC, or by a passage of doped ions such as boron and aluminium when incorporated into the SiC crystal lattice. The most important

electronic properties of SiC are its wide energy band gap of 3.26 eV for 4H-SiC and 3.03 eV for 6H-SiC, high breakdown electric field of 2.2×10^6 $V.cm^{-1}$ for 100 V operations, and high saturated electron drift velocity of 2×10^7 $cm.s^{-1}$ (Schwetz, 2000).

Homogeneous SiC obeys Ohm's Law, while aggregates of SiC grains show nonlinear current-voltage behaviour. At low applied voltages, SiC behave as insulators; increasing the applied voltage above a certain value, increases the current exponentially. Thus, the points of contact between the grains cause the electrical resistance to be voltage dependent (Schwetz, 2000). It is reported (Pelissier *et al.*, 1998) that the electrical resistivity of SiC ceramics depends on the amount and on the nature of the second phase located at the grain boundaries. It also depends on the free carrier concentration in SiC grains. The electrical resistivity is usually discussed in terms of mean scatter time, which is the average interval between collisions of the conduction electrons (phonons). It is believed that an important quantity of additives increases phonons scattering and therefore results in variations in electrical resistivity of the material. The electrical resistivity is a function of temperature as shown in figure 2.2.

SiC is used as electrical heating elements because of its low electrical resistivity (Fett, 1999; Morrell, 1985; Pelissier *et al.*, 1998). The reciprocal of electrical resistivity (ρ) is the electrical conductivity.

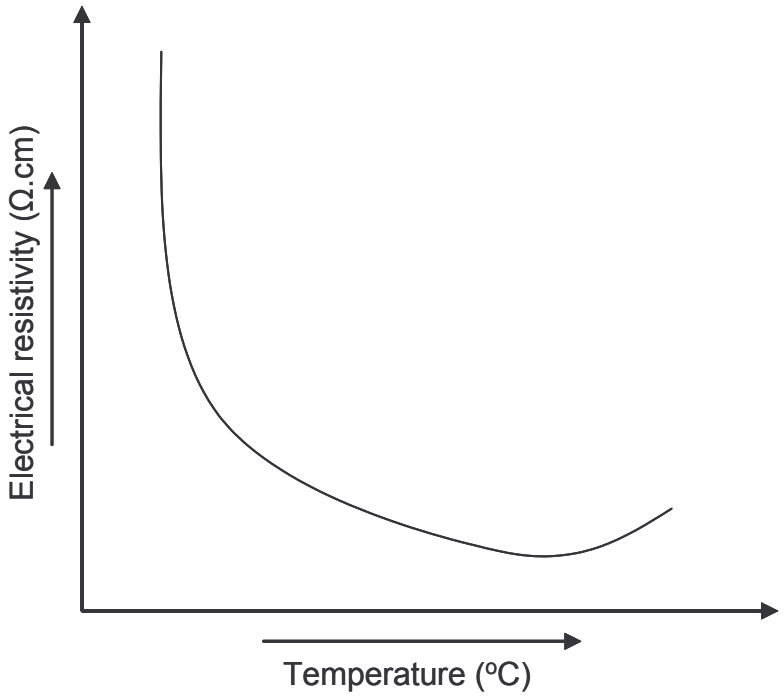


Figure 2.2 Schematic diagram of electrical resistivity of SiC material as a function of temperature (after Pelissier *et al*., 1998)

Thermal and Calorific Properties

Sintered silicon carbide has high thermal conductivity at 600^{o}C (50 W.mK^{-1} for SSiC and LPSSiC). Both solid state and liquid phase sintered silicon carbide have good resistance to thermal shock due to high thermal conductivity (50 W.mK^{-1} for both materials at 600^{o}C) and low thermal expansion - 4.9 x 10^{-6} K^{-1} for SSiC and 4.5 x 10^{-6} K^{-1} for LPSSiC from 30^{o}C to 1500^{o}C - (Schwetz, 2000).

Mechanical Properties

Sintered silicon carbide has a high modulus of elasticity (410 GPa for SSiC and 420 GPa for LPSSiC). Solid state sintered silicon carbide offers considerable advantages over all other ceramic materials in plastic deformation, because of the low content of sintering aids. On the other hand, liquid phase sintered silicon carbide features improved edge toughness close to the edge flaking resistance of silicon nitride

(Schwetz, 2000). Table 2.1 summarises some of the typical properties of solid state and liquid phase sintered silicon carbide ceramics.

Table 2.1 Physical properties of sintered silicon carbide (SSiC) and liquid phase sintered silicon carbide (LPSSiC) ceramics (after Schwetz, 2000)

SiC material type		Sintered SiC (solid state) SSiC	Sintered SiC (liquid phase) LPSSiC
SiC content (weight-%)		98	95
Density (gcm^{-3})		3.15	3.21
Porosity (%)		<2	<1
Young modulus (GPa)		410	420
Thermal expansion 30-1500°C (10^{-6} K^{-1})		4.9	4.5
Thermal conductivity at 600°C (W mK^{-1})		50	50
Flexural strength	20°C (MPa)	430	730
	1400°C (Mpa)	450	400

2.4.2 Chemical Properties

One of the outstanding advantages which ceramic materials have over the other materials is their high degree of chemical inertness. This has enabled silicon carbide ceramic components (valves, bearings, linings and seals) to be used in highly corrosive environments such as gas turbines and heat exchangers (Cook *et al*., 1994; Herrmann *et al.*, 2003; Liu, 1997; Morrell, 1985; Schwetz, 2000; Steen and Ranzani, 2000).

Corrosion properties

The corrosion resistance of a ceramic does not depend solely on the chemical nature of the major component, but can greatly be influenced by the presence of even small

amount of secondary phases. There is therefore an intimate relationship between the corrosion resistance and microstructure (Lay, 1983).

It is reported (Cook *et al.*, 1994; Herrmann *et al.*, 2003; Nickel, 1997) that corrosion of SiC ceramics causes degradation of its properties. The degradation of the properties is not a material property but a system property (Herrmann *et al.*, 2003; Nickel, 1997). The system property comprises, among other factors, the material and the corrosive medium at a given temperature, flow rate and pressure. The chemical stability of polycrystalline ceramics in aggressive environments is strongly affected by the grain boundary phase. The composition, amount, distribution and crystallinity of the grain boundary phase are important. The matrix material is often more resistant to corrosion than the grain boundary phase (Gogotsy and Yoshimura, 1994). The reductions in strength of SiC as a result of corrosion have been studied (Herrmann *et al.*, 2003) and in all cases attributed to the formation of pits. The pit formation in the silicon carbide materials is thought to be caused by the clusters of pores brought about by sintering.

SiC ceramics have very good resistance to acid environments but are not so resistant to alkaline environments (Lay, 1998). Silicon containing products are attacked by HF/HNO_3 mixtures, which dissolve the silicon phase and leave a porous, weaker material (Morrell, 1985; Schwetz, 2000).

2.5 Aqueous Corrosion of SSiC and LPSSiC Ceramics

There are several parameters used to classify corrosion in SSiC and LPSSiC ceramic materials: the attack mode, the medium and the locus. The appropriate names associated with these parameters are shown in figure 2.3. However, the basis for the classification should be the appearance of the corroded material (Jones, 1996; Nickel, 1997).

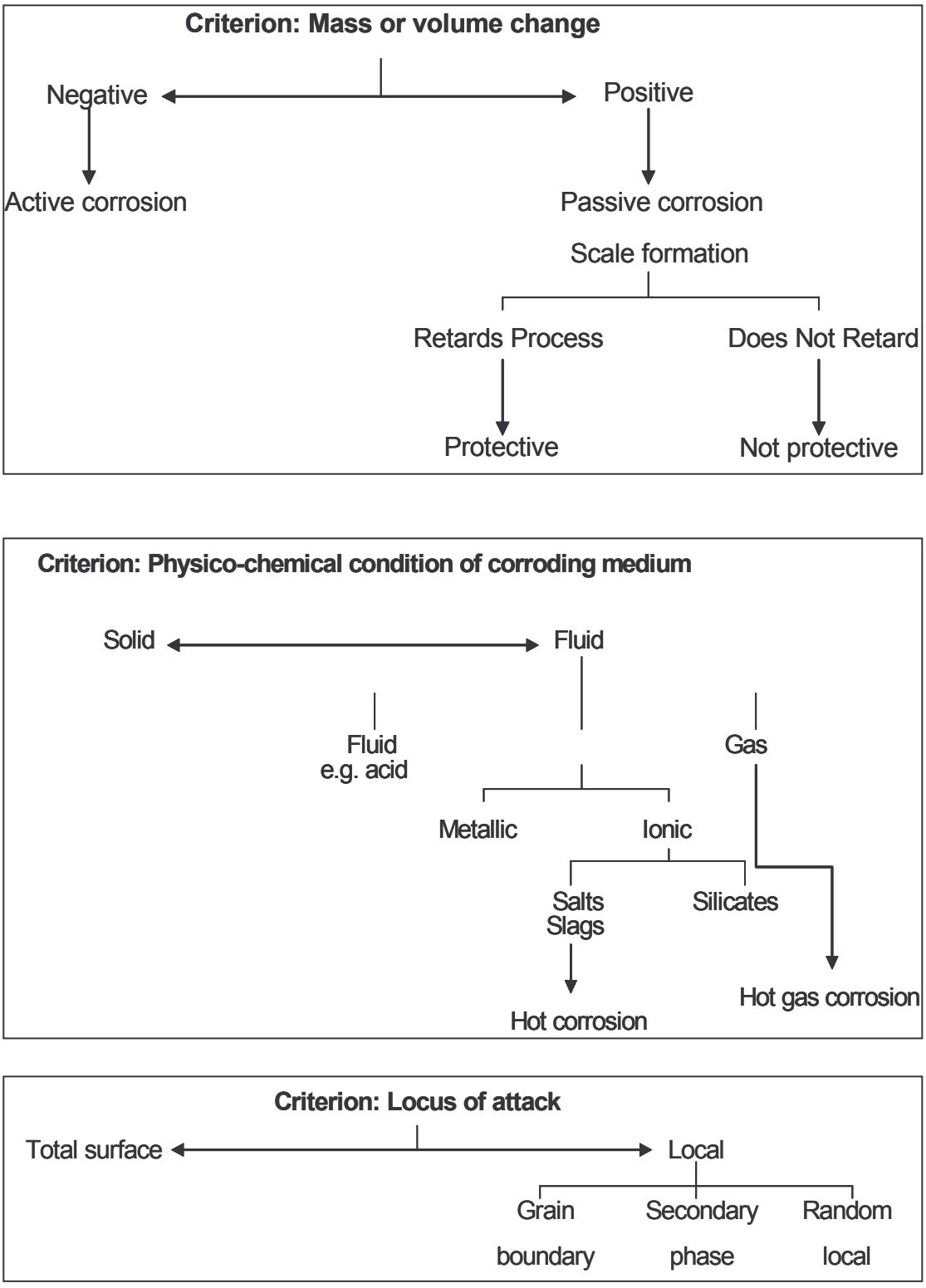


Figure 2.3 Three major classification schemes of corrosion of materials (Nickel, 1997)

2.5.1 Forms of Corrosion in Ceramic Materials

Even though the corrosion resistant properties of SSiC and LPSSiC ceramics make it difficult to detect the various forms of corrosion, the following forms have been identified.

Pitting

Pitting is considered as the intermediate stage between general overall corrosion and complete corrosion resistance (Jones, 1996). Pitting in solid state sintered silicon carbide ceramics comes about as a result of pores present after sintering processes as mentioned in Section 2.3. The voids introduced after sintering serve as an initiation point for the pit to penetrate at an increasing rate. It is difficult to measure pits because of their small size. It is therefore difficult to measure quantitatively and compare the extent of damage because of the varying depth and number of pits that may occur under identical conditions (Jones, 1996). Even though it has been found that there is pitting in ceramic materials (Cook *et al*., 1994; Herrmann *et al*., 2003), it becomes complicated to predict by laboratory tests since pitting takes several years to show up in actual service (Jones, 1996).

Intergranular Corrosion

Grain boundaries in some technical ceramic materials, under certain conditions, could be slightly more resistant to corrosion than the matrix (Herrmann *et al.*, 2003; Nickel, 1997) because of the formation of SiO_2 rich boundaries; HF environments are an exception. However, grain boundary corrosion can occur and is usually caused by the impurities introduced at the grain boundaries during sintering. Intergranular corrosion is the localized attack at and adjacent to grain boundaries, with relatively little corrosion of the grains. SSiC and LPSSiC ceramic materials are polycrystalline and the grain boundary may be viewed as an area of high defect and/or impurity concentration, which makes it more susceptible to corrosion than the bulk material. Small amounts of impurities segregate to the grain boundaries, causing the grain boundary to be less resistant to corrosion and intergranular attack results. Intergranular corrosion causes the material to disintegrate (grains fall out), resulting

in loses in strength of the material. The dependence of the residual strength on the content of the grain boundary phase of LPSSiC ceramics after corrosion in 1 N H_2SO_4 at 101^oC showed a maximum strength at 4 mass-% additives (Herrmann *et al.*, 2003).

Preferential Secondary Phase Corrosion

This type of corrosion usually occurs in infiltrated structured composites such as infiltrated silicon carbide (SiSiC) and LPSSiC. Preferential corrosion is the removal of one element from a solid alloy. The SiSiC contains free silicon which is preferentially corroded by acids and bases (Cook *et al*., 1994; Nickel, 197). Likewise, the oxide phase in LPSSiC materials is preferentially corroded (Herrmann *et al*., 2003).

2.5.2 Corrosion of SSiC and LPSSiC Materials by Immersion Technique

The standard method for measuring the rate of corrosion in ceramic materials has been by immersion (Bellosi *et al*., 2001; Cook *et al*., 1994; Herrmann *et al*., 2003; Nickel and Speipel, 2003; Sharkawy and El-Aslabi, 1998). The corrosion measurement is achieved by immersing the sample in a corrosive medium and measuring the weight loss, the corrosion layer depth, the residual strength, and sometimes the concentration of the corroded ions in the media.

Investigation by Herrmann *et al*. (2003) in a number of acidic and alkaline environments at boiling temperature (101^oC) showed that SSiC has a very good corrosion resistance in both acidic and alkaline environments; their relatively moderate strength level is barely changed by corrosive attack. The LPSSiC materials also showed very low mass losses; however there is decrease in residual strength as a result of pit formation. Investigation by Cook *et al*. (1994) at room temperature showed that SSiC is resistant to acids (HCl, HNO_3 and H_2SO_4) with no mass losses and no significant changes in surface appearance, even after 5000 hours of exposure.

2.5.3 Corrosion of SiC-based Ceramics by Electrochemical Technique

Electrochemical corrosion of solid state sintered SiC (SSiC) and reaction bonded SiC (RBSiC) have been studied at room temperature by Divakar *et al*. (1989) and Cook *et al*. (1994) in various dilute acids (HCl, HNO_3, HF, H_2SO_4 and H_3PO_4) by means of polarization measurements. The investigations by Cook *et al*. (1994) showed that both SSiC and RBSiC are passive in acid environments because of the formation of a surface silica film. HF is an exception since the silica is dissolved. Divakar *et al*. (1989) proposed the principal corrosion mechanism for RBSiC as follows:

$$Si(solid, residual) = Si^{4+}(aq) + 4e^{-} \qquad [2.4]$$

where the residual silicon was preferentially attacked. The equivalent weight of RBSiC was assumed to correspond to that of Si atom alone. On the other hand, it was assumed that 1 mol of Si removal meant removal of 1 mol of SiC.

For SiSiC material, the following anodic reaction was proposed (Divakar *et al*., 1989):

$$\text{Si (solid, in SiC)} = Si^{4+}(aq) + 4e^{-} \qquad [2.5]$$

Thus, it seems the silicon atoms present in RBSiC and SiSiC are responsible for the corrosion behaviour obtained.

Divakar *et al*. (1989) made no mention of the anodic reactions occurring in the cell other than the silicon dissolving to form Si^{4+} ions in solution. However, Cook *et al*. (1994) proposed a number of anodic reactions occurring as:

$$H_3SiO_4^{-}(aq) + 5H^{+}(aq) + 4e^{-} = Si(s) + 4H_2O(l) \qquad E^o = -0.712\,\text{V} \qquad [2.6]$$

$$H_4SiO_4(aq) + 4H^{+}(aq) + 4e^{-} = Si(s) + 4H_2O(l) \qquad E^o = -0.848\,\text{V} \qquad [2.7]$$

$$SiO_2(s) + 4H^{+}(l) + 4e^{-} = Si(s) + 2H_2O(l) \qquad E^o = -0.888\,\text{V} \qquad [2.8]$$

$$SiF_6^{2-}(aq) + 4e^{-} = Si(s) + 6F^{-}(aq) \qquad E^o = -1.37\,\text{V} \qquad [2.9]$$

$$SiO_3^{2-}(aq) + 6H^+(aq) + 4e^- = Si(s) + 3H_2O(l) \qquad E^o = -1.69\,\text{V} \qquad [2.10]$$

These reactions do not take the electrochemical dissolution of the carbon present into consideration.

Very little work, if any, has been done on the electrochemical corrosion of LPSSiC. However, since SiC is electrically conductive, it might be possible to investigate the corrosion mechanisms of LPSSiC materials by electrochemical methods.

2.6 Electrochemical Testing Techniques

Aqueous corrosion reactions are generally electrochemical in nature and therefore can be studied by electrochemical techniques. Electrochemical techniques include potentiodynamic polarisation curves, linear polarisation resistance, open circuit potential decay, AC impedance measurement, and electrochemical noise measurement. For the purposes of this dissertation, only potentiodynamic polarisation measurements are discussed.

Theoretical Background

The potential difference across an open circuit cell (ΔE_n), is determined by thermodynamics. When a device which generates current (I) of any amperage is applied, the voltmeter reads a value, ΔE which is different from ΔE_n. If I is positive, then ΔE will be larger (more positive) than ΔE_n and so E will be more positive than E_n. Conversely, negative current flow through the cell (resulting in a reductive electrode reaction at the working electrode), would cause a negative shift in the electrode potential. This shift in the potential difference across a cell caused by the passage of current is called polarisation (Jones, 1996; Oldham and Myland, 1994). Polarisation has ohmic polarisation, activation polarisation and concentration polarisation effects, respectively. These three polarisation effect arise at different locations in the cell. Activation polarisation has its origin at the electrode interface;

concentration polarisation originates in the depletion zone adjacent to the electrode; ohmic polarisation reflects the resistance of the entire cell. The third polarisation may be reduced by introducing a reference electrode. Detail of these effects can be found in literature (Jones, 1996; Oldham and Myland, 1994).

Instrumentation and Experimental Procedure

The test cell consist of the working electrode, auxiliary/counter electrode, a Luggin capillary with salt bridge connection to the reference electrode, gas inlet and outlet tubes, and a thermometer. Figure 2.4 shows a schematic potentiodynamic polarisation setup.

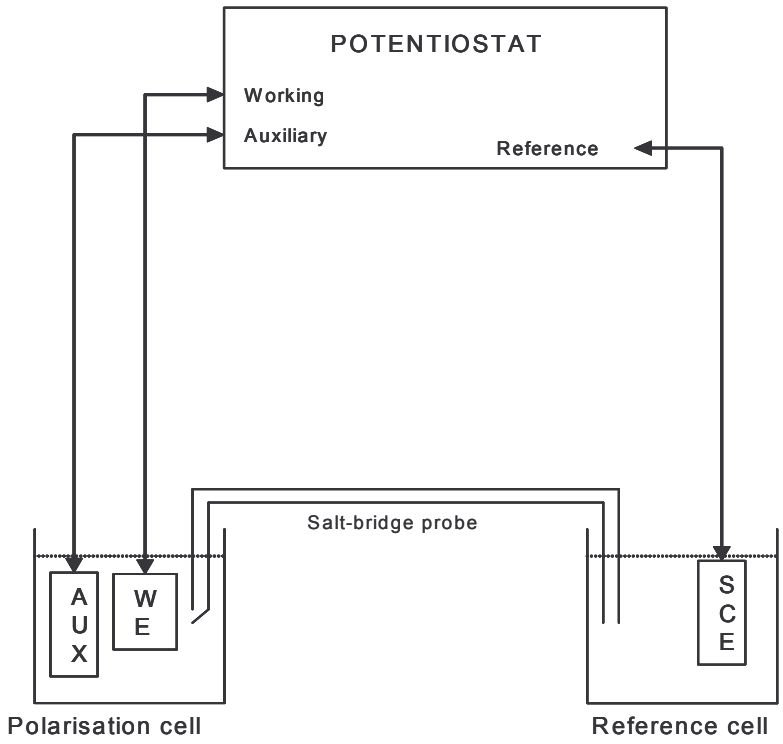


Figure 2.4 Schematic potentiodynamic polarisation measurement setup diagram (after Jones, 1996)

An electronic device called a scanning potentiostat is employed for potentiodynamic measurements. This is connected to all three electrodes as shown in figure 2.4. The potentiostat automatically vary the potential at a constant rate between two preset potentials which generates current through the cell. The current supplied goes to the working electrode, through an auxiliary electrode, AUX. The potential of the working electrode is measured with respect to the reference electrode, REF. As mentioned, the salt bridge and the Luggin probe are usually included to minimise ohmic resistance interference in the electrolyte. Data logging of the potential and current, as well as control of the potentiostat functions, are usually done by a computer with relevant software. A typical polarisation measurement curve obtained from such experiment is shown in figure 2.5. Information that could be obtained from such graphs include open circuit potential (E_{corr}), corrosion current density (i_{corr}) and Tafel slopes. i_{corr}, which is directly proportional to the corrosion rate, is determined by Tafel extrapolation method: linear regions of Tafel slopes extended until they meet as indicated below.

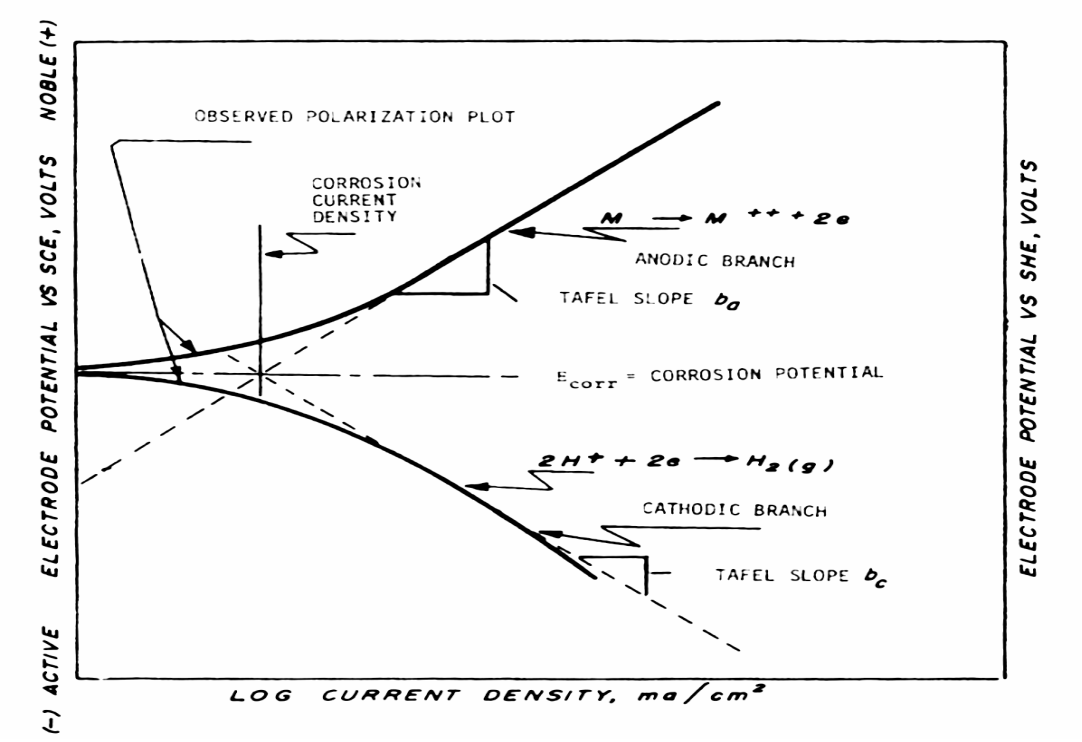


Figure 2.5 Typical Tafel plot from polarisation experiment (ASTM G3 - 89)

CHAPTER 3

EXPERIMENTAL PROCEDURE

3.1 Introduction

Various techniques have been used to determine the corrosion mechanisms of the SSiC and LPSSiC ceramic materials. The experimental techniques are described in detail in this chapter.

3.2 Materials

Two SiC – based ceramic materials were investigated: solid state sintered silicon carbide (SSiC) and liquid phase sintered silicon carbide (LPSSiC). The SSiC ceramic material was gas pressure sintered in Ar at a temperature of 2100^{o}C with carbon (C) and boron (B) as sintering additives. Two LPSSiC materials of different additive ratios were investigated: both materials were sintered at a temperature of about 1950^{o}C with Al_2O_3 and Y_2O_3 as sintering additives. The materials characterisation is discussed in Chapter 4.

3.3 Image Analyses

The microstructures and compositions of the materials before and after corrosion were analysed by means of scanning electron microscopy (SEM) and X-ray diffraction (XRD). Samples were prepared for image analysis by grinding on Struers MD-Piano 1200 to achieve a flat surface and polishing on a Pan cloth to 1 μm finish using diamond spray and diamond extender (lubricant). The samples were rinsed afterwards with ethanol, and dried.

A LEO 1525 scanning electron microscope was used to examine the microstructures of the samples. X-ray diffraction experiments were performed with a Phillips

PW1710-based powder diffractometer. The diffractometer parameters are given in table 3.1. Raman Spectrometry (JOBIN-YVON T64000) and Scanning X-ray photoelectron spectroscopy (PHI Quantum 2000) were used to examine the surface of the materials after corrosion.

Table 3.1 X-ray diffractometer parameters used for the analyses of the samples

Anode material	Copper
Generator settings	40kV, 20mA
Step size, ^{o}2Th	0.02
Step size time, s	1.0
Scan type	Step
Monochromator	None

To determine the volume fractions of the binder, at least eight micrographs were taken at different magnifications, analysed using Image Tool© (version 3) and the mean area fraction calculated. The mean area fraction represents the volume fractions of the different grains identified (see Table 4.1).

3.4 Electrochemical Corrosion Measurements

The electrochemical corrosion behaviour of SSiC and LPSSiC ceramic materials were investigated by using potentiodynamic polarisation measurements according to ASTM G 5-94 and ASTM G 3-89.

Samples were prepared by attaching insulated copper wire to one face of the sample with aluminium conductive tape and cold mounting in resin with addition of a catalyst. Samples were polished on a Pan cloth to 1 μm surface finish and were coated at the sample-resin interface with Bostik quickset to eliminate the possibility of crevice corrosion. After coating the samples with Bostik quickset, they were cleaned in an ultrasonic bath with ethanol before immersion in the electrolyte.

A Schlumberger (SI 1286) electrochemical interface was connected to a personal computer (PC) with electrochemical application software for control and data-logging. All tests were done at room temperature (~25^{o}C). Solutions were replaced after each test run. Samples were re-polished and used in the subsequent scans. A platinum counter electrode (CE) was used. A saturated calomel reference electrode (SCE) was connected to the cell via a Luggin capillary. The probe tip was suspended approximately 1 cm above the sample surface. All potentials reported are versus the SCE potential (standard hydrogen potential, SHE = SCE + 241 mV). A schematic diagram of the experimental setup is shown in figure 3.1.

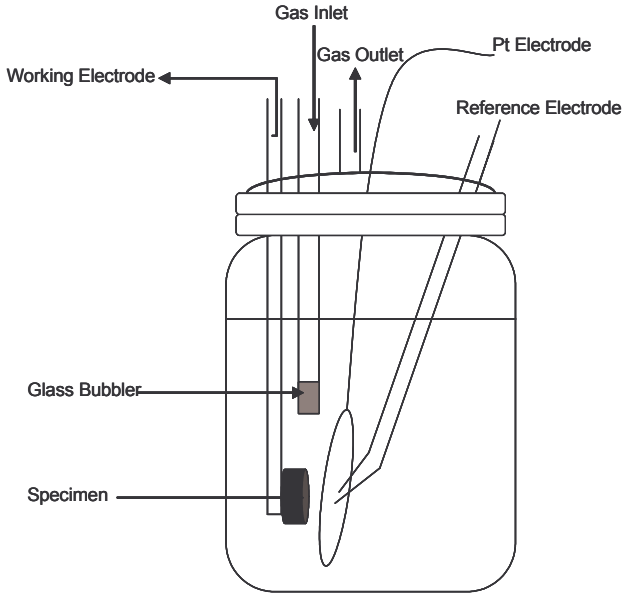


Figure 3.1 Schematic diagram of the setup used for the potentiodyanmic polarisation tests

The electrolytes were prepared from reagent grade chemicals and distilled water. Electrolytes used included 1 M solutions of HCl, HNO_3 and NaOH. In addition to this, distilled water was used in two tests. These electrolytes were chosen to assist in general understanding of the corrosion behaviour of the SSiC and LPSSiC ceramic materials in both acidic and alkaline environments. 40.0g of sodium carbonate (Na_2CO_3) and 10.0g of yttrium chloride (YCl_3) were dissolved in 0.4 litres of 1 M NaOH and 0.3 litres 1 M HCl, respectively, and also used as electrolytes; the details

are explained in Section 5.3.1 and Section 6.3.1, respectively. Before immersion of the samples, the corrosive solutions were purged with ultra-high purity (99.999%) nitrogen gas (except where CO_2 was used, as explained in Section 5.3.1) for approximately 45 minutes to reduce the dissolved-oxygen content. Purging was continued throughout the tests.

The open-circuit potential (E_{corr}) was measured 5 minutes after immersion of samples. A potential scan was then initiated using a scan rate of 1 mV/s. The width of the scan was from -200 mV to about +1000 mV relative to E_{corr}. At least three full scans were conducted per sample-electrolyte combination. The corrosion current density (i_{corr}), which is directly proportional to the corrosion rate, was determined by Tafel extrapolation method: linear regions of Tafel slopes extended until they meet (Jones, 1996).

3.5 Inductively Coupled Plasma Optical Emission Spectrometer

An inductively coupled plasma optical emission spectrometer (SPECTRO CIRUS CCD) was used to determine the concentrations of Al, Si, and Y cations in the electrolyte before and after corrosion for the LPSSiC materials. The following analytical wavelengths were chosen (nm): 396.156 Al, 251.611 Si, and 371.030 Y. These wavelengths showed a good linear response between concentration and intensity and were free from interferences in the range of concentrations used in the present study.

CHAPTER 4

MATERIAL CHARACTERISATION

4.1 Introduction

The solid state sintered silicon carbide and liquid phase sintered silicon carbide ceramic materials were characterised based on their compositions and microstructures. Details of the results are shown in this chapter.

4.2 Material Compositions

The compositions of the materials along with the densities and volume percent of the binder are shown in table 4.1. The volume fraction of the residual carbon was also determined by image analysis and found to be 2.4 %. The measured density was 97.8 % of the theoretical density.

Different mole ratios of Y_2O_2/Al_2O_3 (1:1 and 1:4, respectively) were used for the LPSSiC materials as sintering additives. The porosity of LPSSiC-2 is higher than that of LPSSiC-1, due to some loss of alumina according to the equation:

$$SiC(s) + Al_2O_3(s) \Leftrightarrow Al_2O(g) + SiO(g) + CO(g) \qquad [4.1]$$

This reaction increases with high alumina content and high sintering temperature [Izhevskyi, 2000; Magnani *et al*., 2000]. The measured densities for LPSSiC-1 and LPSSiC-2 materials were 98.9 % and 97.6 % of the theoretical density, respectively.

Table 4.1 Material compositions of both SSiC and LPSSiC. The porosity and volume percent of binder were measured in this investigation using Image Tool© (version 3)

Material	Additives	Mol ratio additives Y_2O_3/Al_2O_3	Density (g/cm^3)	Theoretical Density (g/cm^3)	Porosity (%)	Vol. % of binder
SSiC	B,C	-	3.11	3.18	2.4	-
LPSSiC-1	Y_2O_3/Al_2O_3 10 wt %	1:1	3.32	3.36	1.2	9.0
LPSSiC-2	Y_2O_3/Al_2O_3 10 wt %	1:4	3.26	3.34	2.4	9.78

4.3 Microstructural Analysis of SSiC Material (as-sintered)

The microstructure of SSiC, shown in figure 4.1, consists of two phases: SiC (light gray phase) and residual carbon as a result of sintering (gray phase). There is also porosity – the dark areas with white rings around them.

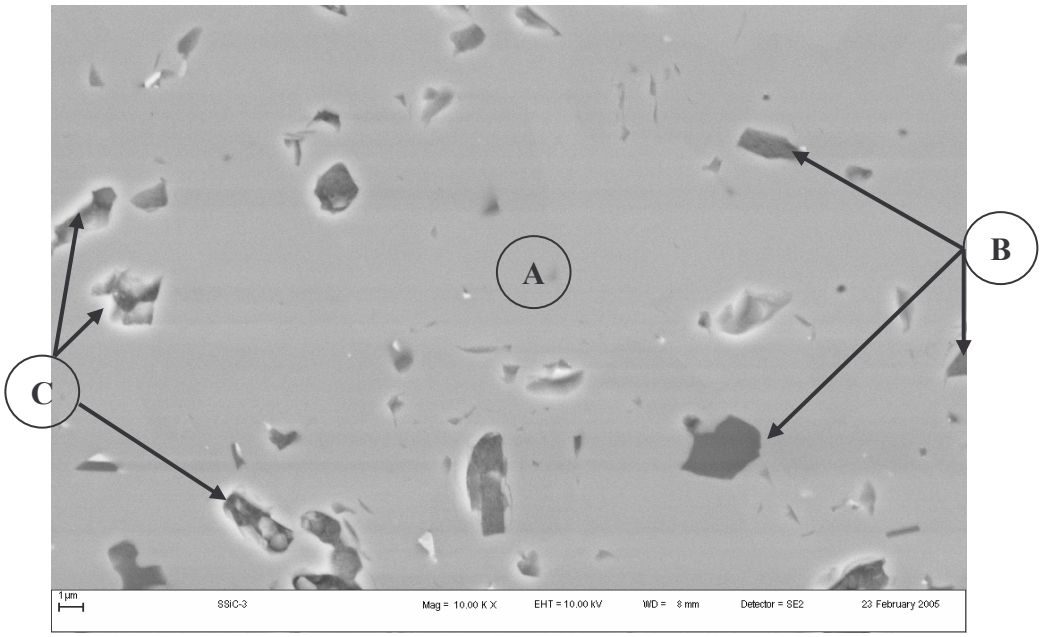


Figure 4.1 Secondary electron SEM micrograph of a polished section of SSiC (as-sintered). The following features are marked: (A) silicon carbide (light gray phase), (B) carbon inclusions (gray phase), and (C) porosity (dark areas)

The XRD pattern of the material (Figure 4.2) shows carbon and SiC as the main grains present. The SiC exists in a number of forms with various stacking arrangements of atomic planes; these are classified into hexagonal and rhombohedral crystal systems (i.e. 6H, 15R and 4H). The different modifications are not distinguishable in the SEM micrograph. The residual carbon is graphitic with rhombohedral modifications; these modifications are also not distinguishable in the SEM micrograph.

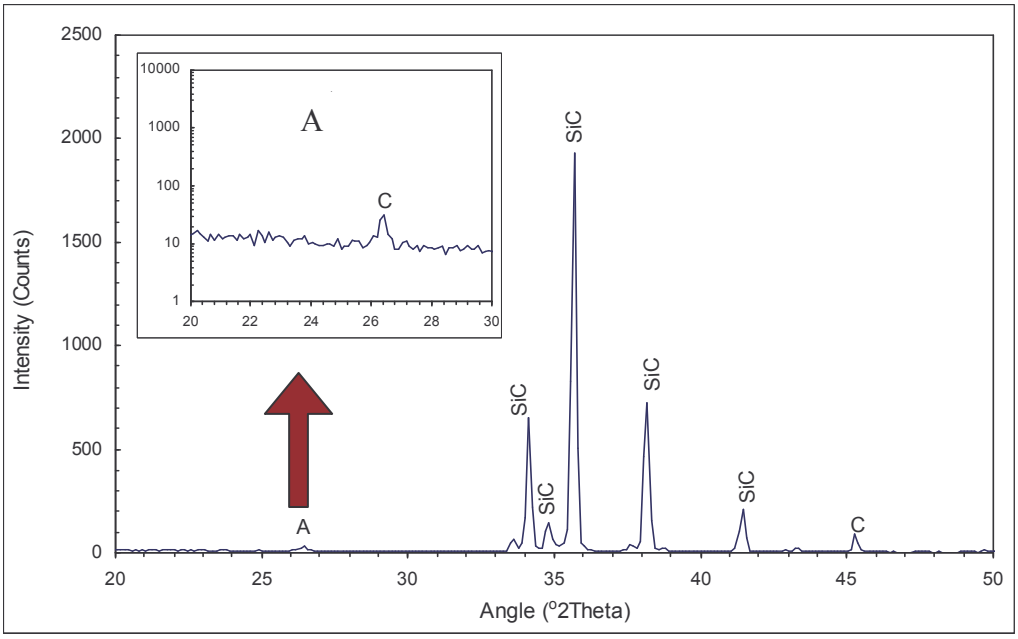


Figure 4.2 XRD pattern of SSiC (as-sintered) showing residual carbon in the sample. The enlargement of peak "A" is shown in the insert.

4.4 Microstructural Analysis of LPSSiC Materials (as-sintered)

The microstructures of LPSSiC-1 and LPSSiC-2, shown in figures 4.3 and 4.4, reveal white regions corresponding to the secondary phases in the form of aluminium yttrium oxides. These secondary phases are formed from the liquid phase during sintering as a result of the reaction between the added Al_2O_3 and Y_2O_3. The gray phase corresponds to SiC grains, also in different stacking arrangements (6H, 15R and 4H). The dark portions in figure 4.4 are porosity introduced during sintering due to some loss of alumina (Table 4.1).

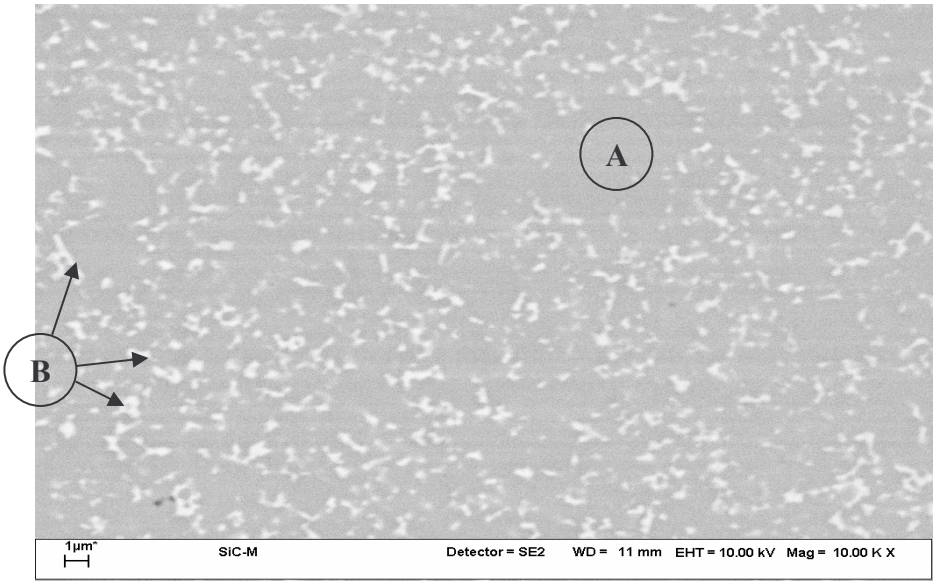


Figure 4.3 Secondary electron SEM micrograph of a polished section of LPSSiC-1 (as-sintered). The following features are marked: (A) silicon carbide (light gray phase) and (B) secondary phases (white).

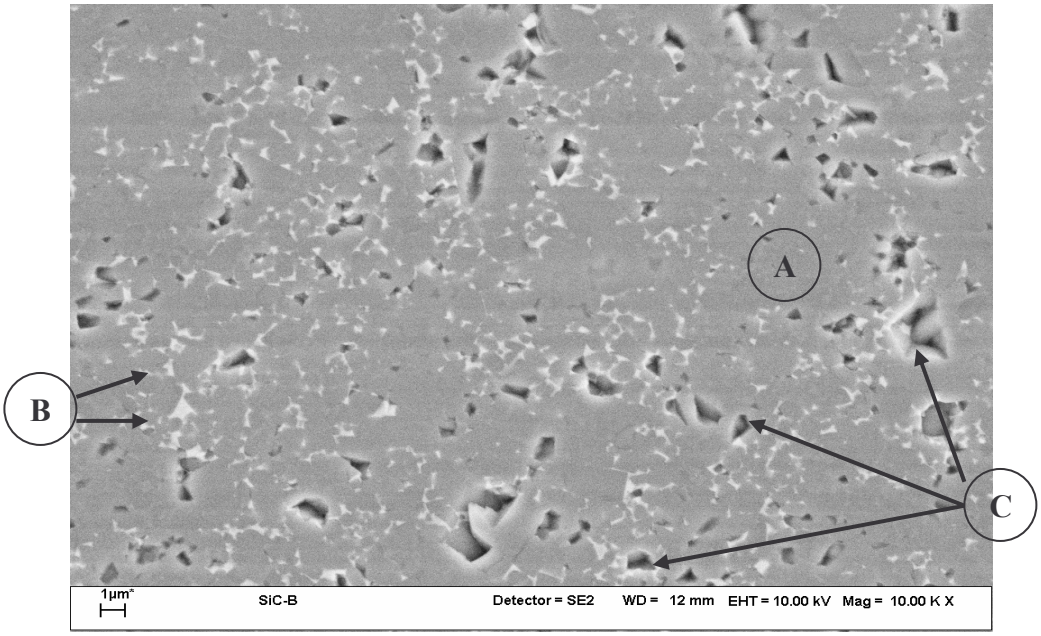


Figure 4.4 Secondary electron SEM micrograph of a polished section of LPSSiC-2 (as-sintered). The following features are marked: (A) silicon carbide (light gray phase), (B) secondary phase (white), and (C) porosity (dark areas).

The XRD patterns of the materials (Figures 4.5 and 4.6) show YAG ($Y_3Al_5O_{12}$) as the major secondary phase. The LPSSiC-1 contains aluminium yttrium oxide ($Al_2Y_4O_9$) whereas the LPSSiC-2 material contains excess alumina. These oxides are not distinguishable in the SEM micrographs. The $Al_2Y_4O_9$ has a monoclinic crystal system while the YAG phase has a cubic crystal system; the excess alumina in LPSSiC-2 is rhombohedral.

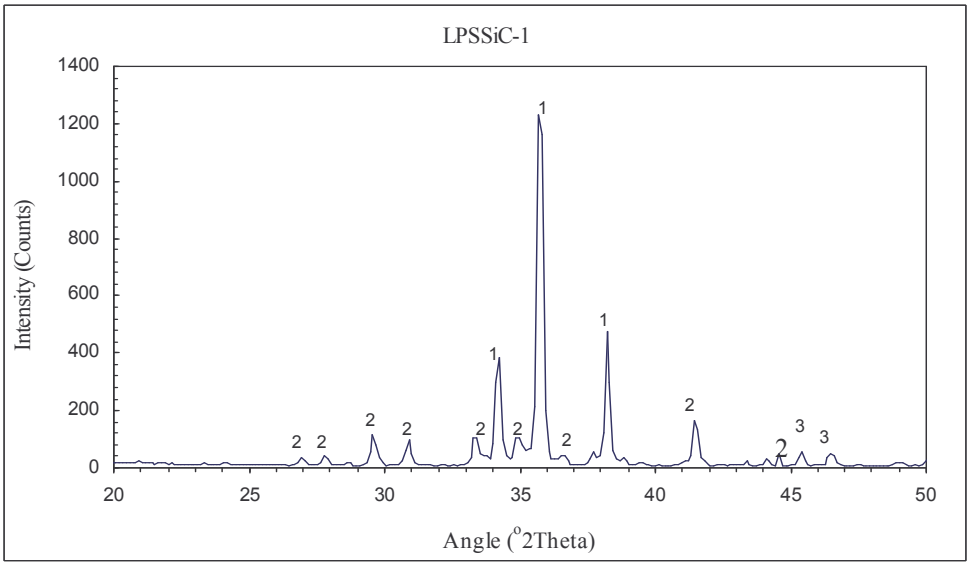


Figure 4.5 XRD pattern of LPSSiC-1 (as-sintered) showing the different phases in the sample: 1- SiC modification; 2 - yttrium aluminate (YAG); 3 - alminium yttrium oxide ($Al_2Y_4O_9$).

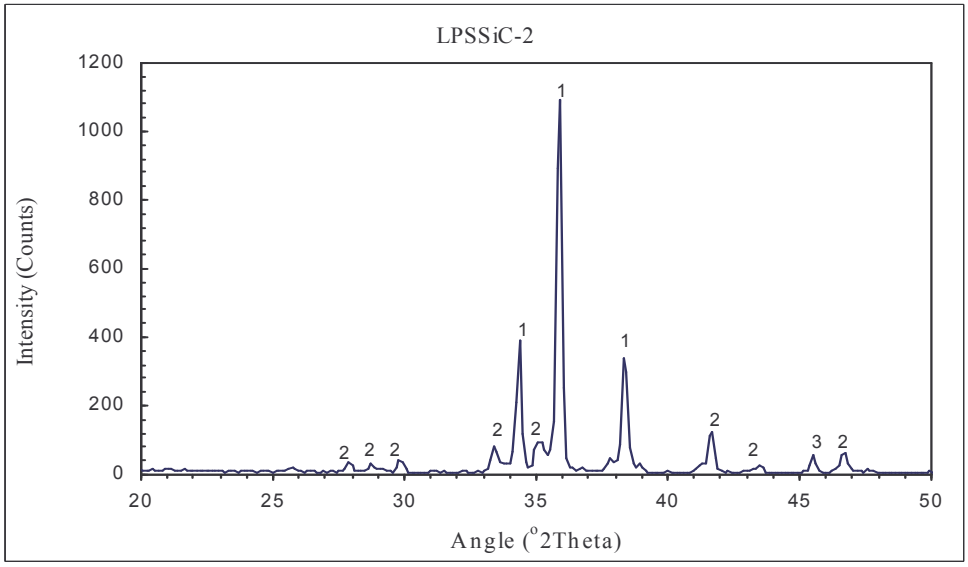


Figure 4.6 XRD pattern of LPSSiC-2 (as-sintered) showing the different phases in the sample: 1 – SiC modification; 2 - yttrium aluminate (YAG); 3 - alumina (Al_2O_3).

CHAPTER 5

CORROSION OF SOLID STATE SINTERED SILICON CARBIDE (SSiC)

5.1 Introduction

After characterising the SSiC materials, corrosion tests were performed on them in acidic and alkaline environments. The test results are presented first, followed by five hypotheses that were proposed to explain the corrosion mechanisms of SSiC materials.

5.2 Electrochemical Behaviour

Results of the corrosion behaviour of SSiC in the different electrolytes are presented on semi-logarithmic plots along with their microstructural changes after the polarisation scans. The electrolytes were chosen to assist in the general understanding of the corrosion mechanisms of SSiC ceramics in acidic and alkaline environments.

5.2.1 Corrosion behaviour in HCl

The potentiodynamic polarisation results and the surface after corrosion are shown in figures 5.1 and 5.2, respectively. The reproducibility of the potentiodynamic polarisation scans in HCl was very good. The anodic current density initially increased as the potential was increased above E_{corr}. Beyond +160 mV the current density dropped slightly (about 75 $\mu A/cm^2$) and a plateau, or pseudo-passive region was formed. The average corrosion current density was about 46 $\mu A/cm^2$.

The corroded surface (see Figure 5.2) did not show any damage even though there was a measurable corrosion current density. The residual carbon seems not to have been affected.

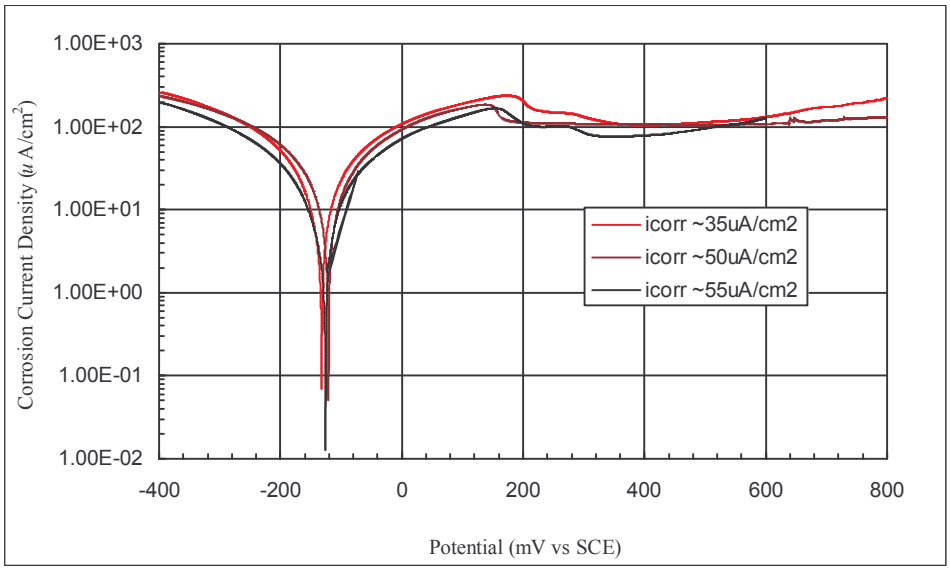


Figure 5.1 Potentiodynamic polarisation scans of SSiC in 1 M HCl showing good reproducibility. Pseudo-passivity was observed at approximately +160 mV. The average corrosion current density is ~46 $\mu A / cm^2$.

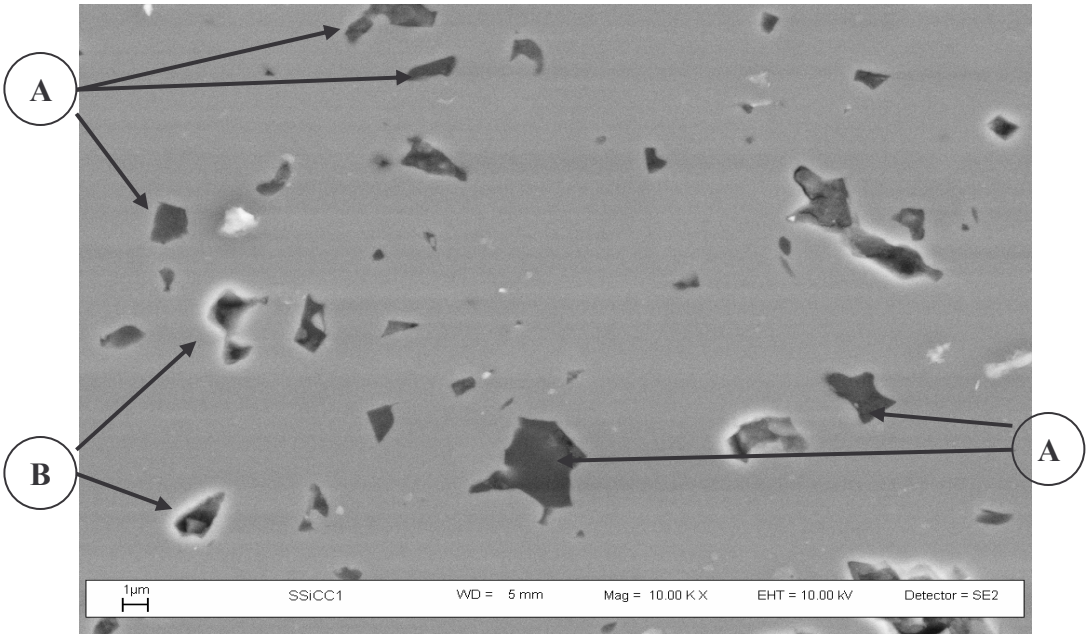


Figure 5.2 Secondary electron SEM micrograph of SSiC after full potentiodynamic scan in 1 M HCl showing no significant surface damage. The following features are marked: (A) residual carbon and (B) porosity.

5.2.2 Corrosion behaviour in HNO_3

The polarisation results and the SEM micrograph after scanning in 1 M HNO_3 are shown in figures 5.3 and 5.4, respectively. The corrosion behaviour was similar to that in HCl with a difference in E_{corr} of about +50 mV. Thus, SiC seems to be slightly more noble in HNO_3 than in HCl. Potentiodynamic polarisation curves showed very good reproducibility. Pseudo-passivity features were observed at approximately +700 mV, at which the current density decreased slightly (about 25 $\mu A/cm^2$). The average corrosion current density was approximately 58 $\mu A/cm^2$.

There were no obvious surface damage after scanning (see Figure 5.4) and the residual carbon seems not to have been affected.

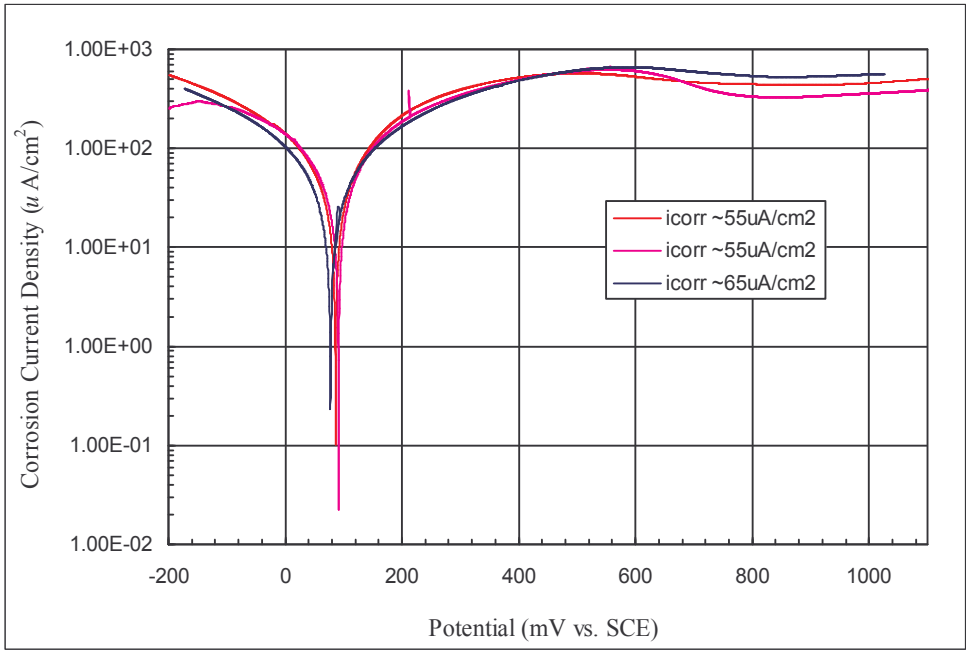


Figure 5.3 Potentiodynamic polarisation scans of SSiC in 1 M HNO_3 showing very good reproducibility. The average corrosion current density is ~58 $\mu A / cm^2$.

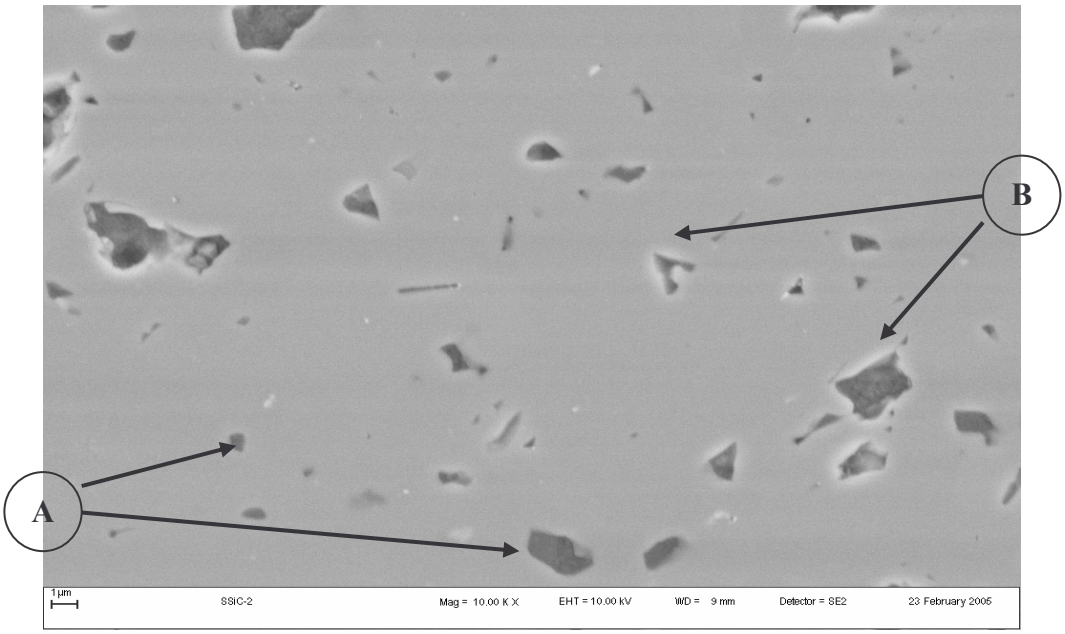


Figure 5.4 Secondary electron SEM micrograph of SSiC after full potentiodynamic scan in 1 M HNO_3 showing no significant surface damage. The following features are marked: (A) residual carbon and (B) porosity.

5.2.3 Corrosion behaviour in NaOH

The potentiodynamic polarisation curves of SSiC along with the SEM micrograph are shown in figures 5.5 and 5.6, respectively. The results were reproducible and no pseudo-passivity feature (as was seen in HCl and HNO_3) could be observed. The average corrosion current density was approximately 33 $\mu A/cm^2$. There is also a shift in the open circuit potential of about +70 mV with respect to HCl and +25 mV with respect to HNO_3.

Again there was no observable surface damage after scanning (see Figure 5.6), and the residual carbon did not seem affected.

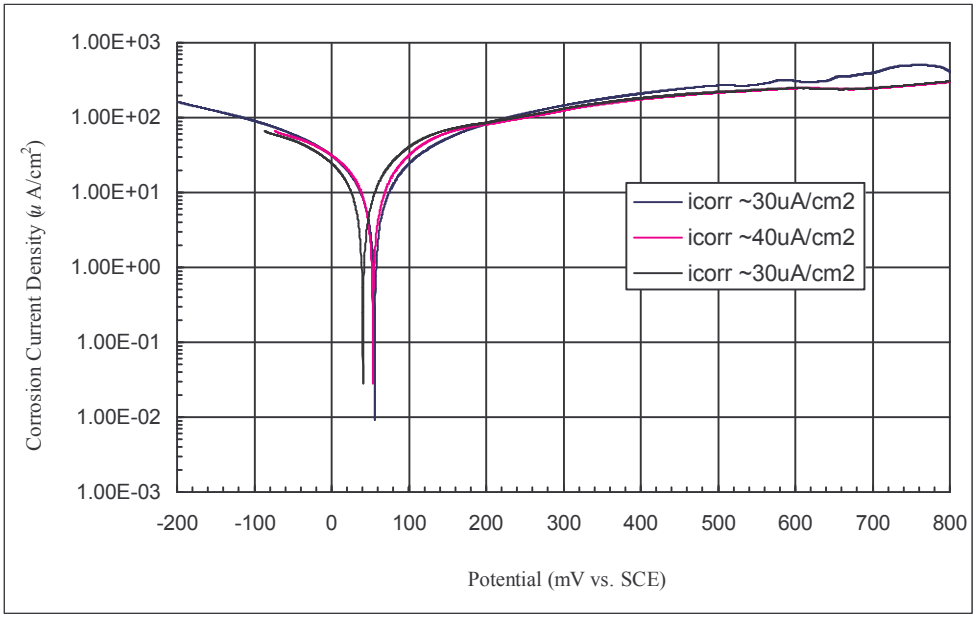


Figure 5.5 Potentiodynamic polarisation scans of SSiC in 1 M NaOH showing good reproducibility. The average corrosion current density is ~33 $\mu A/cm^2$.

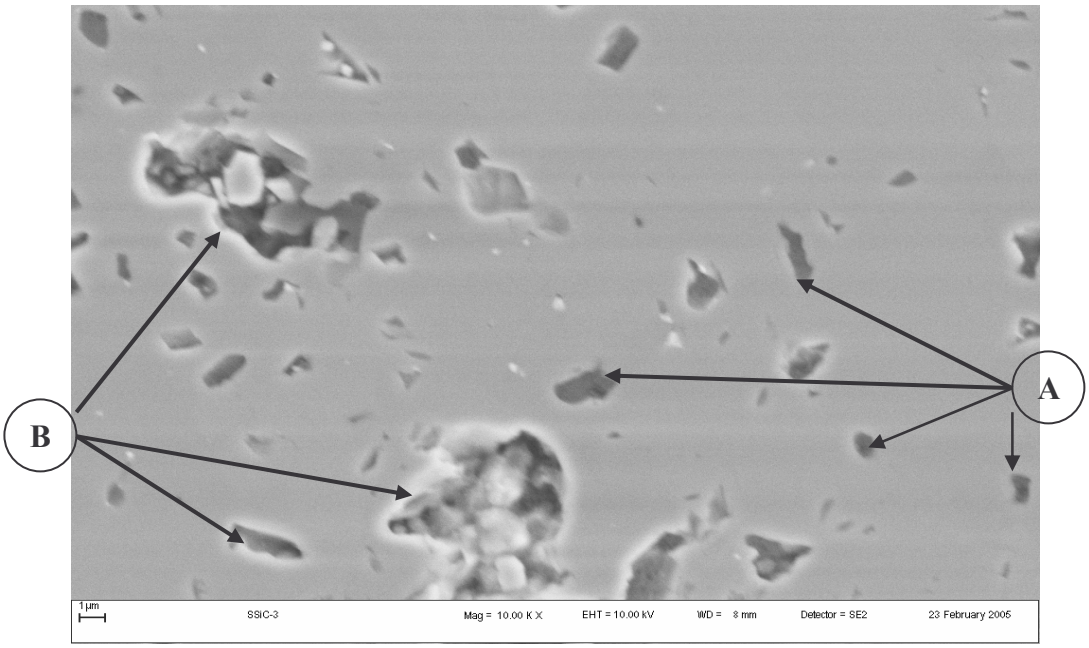


Figure 5.6 Secondary electron SEM micrograph of SSiC after full potentiodynamic scan in 1 M NaOH showing some surface damage around the porosities. The following features are marked: (A) residual carbon and (B) porosity

5.2.4 Corrosion behaviour in distilled water

The potentiodynamic polarisation curves and the microstructural appearance after scanning in distilled water are shown in figures 5.7 and 5.8, respectively. The polarisation curves had very good reproducibility. No passivation features were observed; this is probably due to the high pH, which behaves like NaOH. The average corrosion current density was ~3 $\mu A / cm^2$.

The SEM micrograph after scanning (see Figure 5.8) did not show any surface damage. The residual carbon was also not affected.

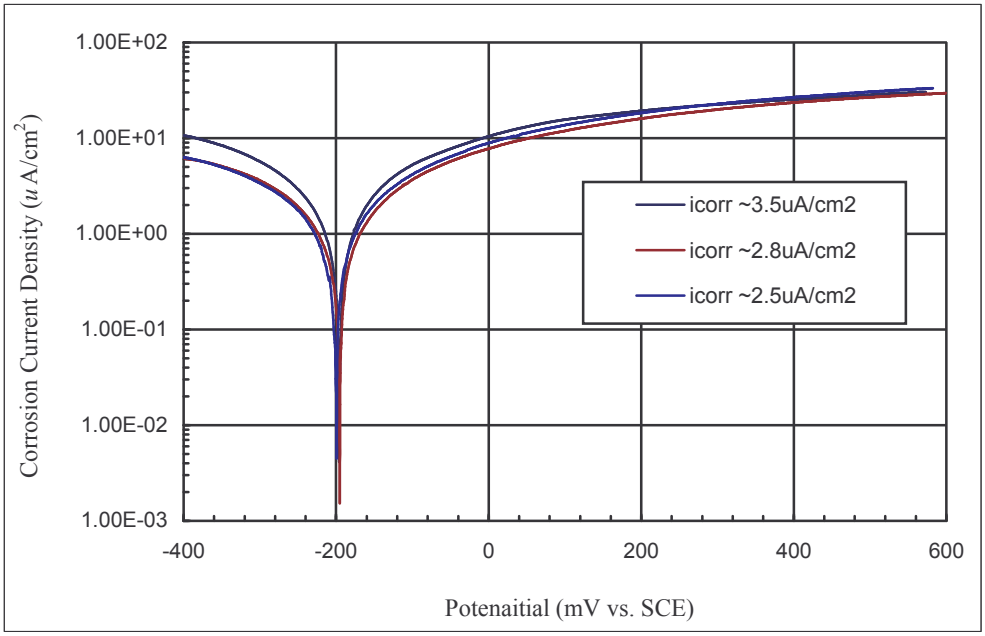


Figure 5.7 Potentiodynamic polarisation scans of SSiC in distilled water showing very good reproducibility. The average corrosion current density is ~3 $\mu A / cm^2$.

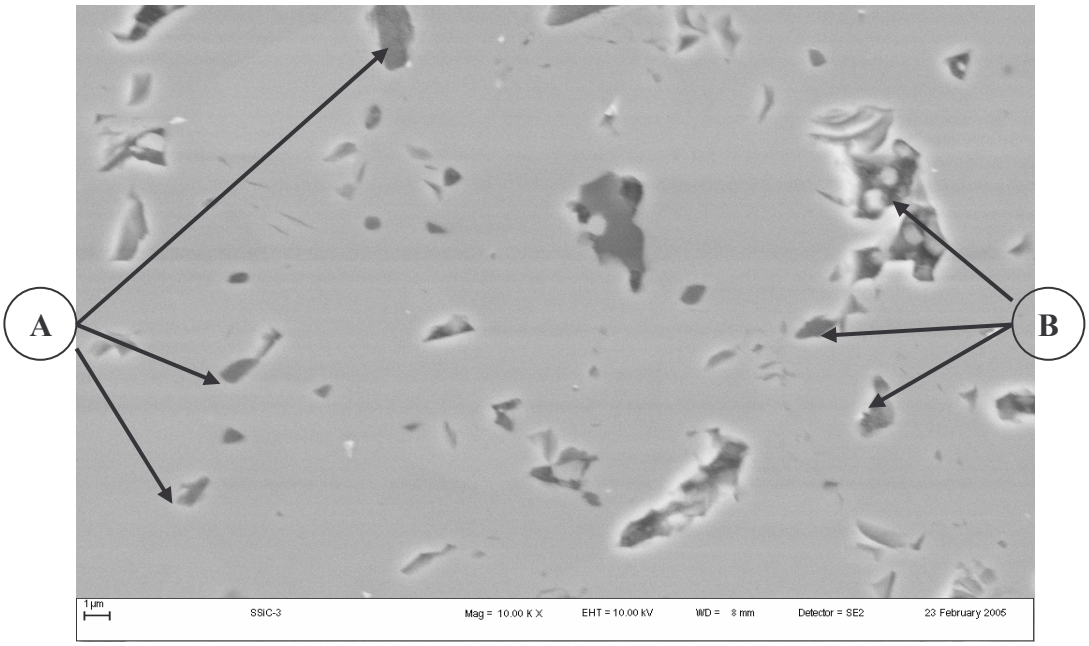


Figure 5.8 Secondary electron SEM micrograph of SSiC after full potentiodynamic scan in distilled water showing no surface damage. The following features are marked: (A) residual carbon and (B) porosity.

In general, the average corrosion current density of SSiC in HCl, HNO_3 and NaOH were approximately the same. The average corrosion current density in distilled water was much lower than in HCl, HNO_3 and NaOH. The graph comparing the corrosion current densities of SSiC in the different media are shown in figure 5.9.

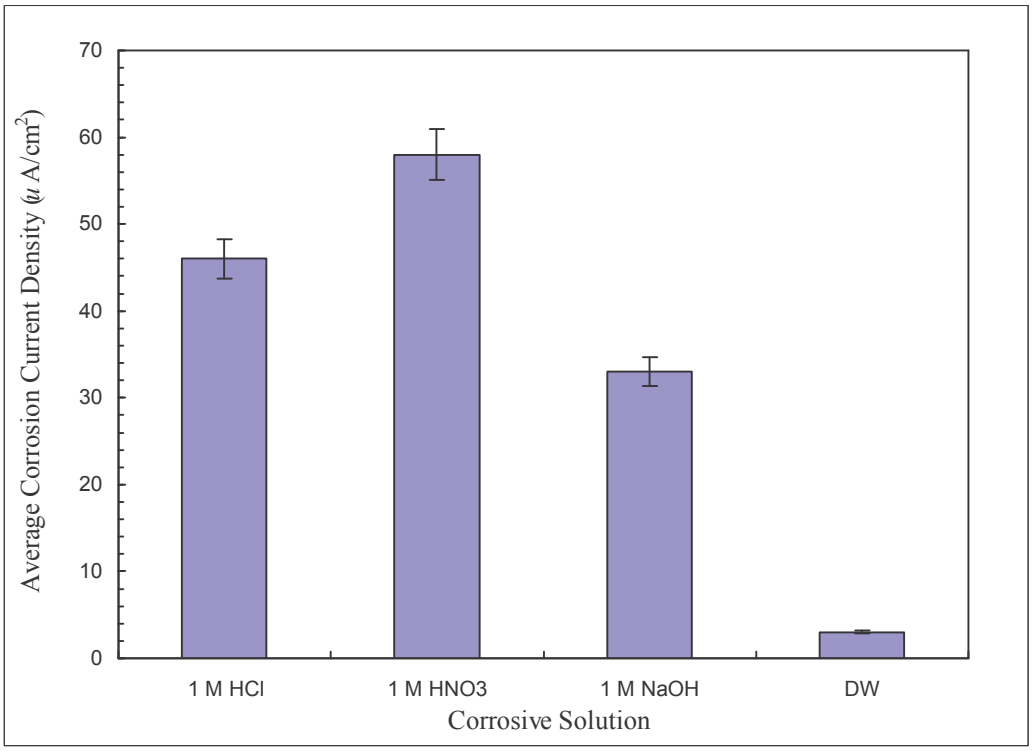


Figure 5.9 Average corrosion current densities of SSiC sample in different corrosive media. The slight shift in E_{corr} has not been accounted for in the graph above.

5.3 Corrosion Mechanisms of SSiC

A number of anodic reactions that could be responsible for the electrochemical corrosion of SSiC are found in literature, together with their corresponding standard potentials (E^o) (Antelman, 1982; Bard *et al*., 1985; Pourbaix *et al*., 1958; SGTE, 2001). These potentials are measured against the Standard Hydrogen Electrode (SHE).

In acidic environments, silicon and carbon would react as

$$C(s) + 2H_2O(l) \rightarrow CO_2(g) + 4H^+(aq) + 4e^- \qquad E^o = +0.206 \text{ V} \qquad [5.1]$$

$$C(s) + H_2O(l) \rightarrow CO(g) + 2H^+(aq) + 2e^- \qquad E^o = +0.517 \text{ V} \qquad [5.2]$$

$$Si(s) + 2H_2O(l) \rightarrow SiO_2(s) + 4H^+(aq) + 4e^- \qquad E^o = -0.888 \text{ V} \qquad [5.3]$$

$$Si(s) + 4H_2O(l) \rightarrow H_4SiO_4(aq) + 4H^+(aq) + 4e^- \qquad E^o = -0.848 \text{ V} \qquad [5.4]$$

$$Si(s) + 4H_2O(l) \rightarrow H_3SiO_4^-(aq) + 5H^+(aq) + 4e^- \qquad E^o = -0.712 \text{ V} \qquad [5.5]$$

In alkaline environments, silicon and carbon would react as

$$C(s) + 6OH^-(aq) \rightarrow CO_3^{2-}(aq) + 3H_2O(l) + 4e^- \qquad E^o{}_B = +1.72 \text{ V} \qquad [5.6]$$

$$Si(s) + 6OH^-(aq) \rightarrow SiO_3^{2-}(aq) + 3H_2O + 4e^- \qquad E^o{}_B = -1.69 \text{ V} \qquad [5.7]$$

Based on the above reactions, eight electrochemical reactions for SSiC were proposed as the possible corrosion reactions in acidic and alkaline environments. The standard (SHE) potentials were calculated based on thermodynamics. The detailed calculations are shown in Appendix A.

In acidic environments, the residual carbon and SiC can undergo dissolution according to the following reactions:

$$C(s) + 2H_2O(l) \rightarrow CO_2(g) + 4H^+(aq) + 4e^- \qquad E^o = +0.206 \text{ V} \qquad [5.8]$$

$$SiC(s) + 2H_2O(l) \rightarrow SiO_2(s) + C + 4H^+(aq) + 4e^- \qquad E^o = -1.07 \text{ V} \qquad [5.9]$$

$$SiC(s) + 4H_2O(l) \rightarrow SiO_2(s) + 8H^+(aq) + CO_2(g) + 8e^- \qquad E^o = -0.433 \text{ V} \quad [5.10]$$

$$SiC(s) + 3H_2O(l) \rightarrow SiO_2(s) + 6H^+(aq) + CO(g) + 6e^- \qquad E^o = -0.542 \text{ V} \quad [5.11]$$

While in alkaline environments, the residual carbon and SiC can undergo dissolution according to the following reactions:

$$C(s) + 6OH^-(aq) \rightarrow CO_3^{2-}(aq) + 3H_2O(l) + 4e^- \qquad E^o{}_B = +1.72\,\text{V} \quad [5.12]$$

$$SiC(s) + 6OH^-(aq) \rightarrow SiO_3^{2-}(aq) + C + 3H_2O(l) + 4e^- \qquad E^o{}_B = -1.874 \text{ V} \quad [5.13]$$

$$SiC(s) + 12OH^-(aq) \rightarrow SiO_3^{2-}(aq) + 5H_2O(l) + CO_3^{2-}(aq) + 8e^-$$

$$E^o{}_B = -0.076\,\text{V} \quad [5.14]$$

$$SiC(s) + 8OH^-(aq) \rightarrow SiO_3^{2-}(aq) + 4H_2O(l) + CO(g) + 6e^- \qquad E^o{}_B = -0.8\,\text{V} \quad [5.15]$$

In the remaining sections of this chapter, five hypotheses were proposed with the aim of determining which of these reactions govern the corrosion behaviour of the materials in the various corrosive media (Section 5.2).

5.3.1 Effect of Carbon

Hypothesis I

If residual carbon is responsible for the measured corrosion behaviour, holding the sample at a more positive potential for a while would remove the residual carbon, thereby eliminating its effect on the measured corrosion current densities and subsequently leading to lower corrosion current densities during potentiodynamic testing.

Samples were held at +500 mV (vs. SCE) in 1 M HNO_3 for 5, 10, 20, 30 and 60 minutes, respectively, before performing potentiodynamic tests. All scans were measured under identical conditions. The results of the investigation are shown in figures 5.10 to 5.13.

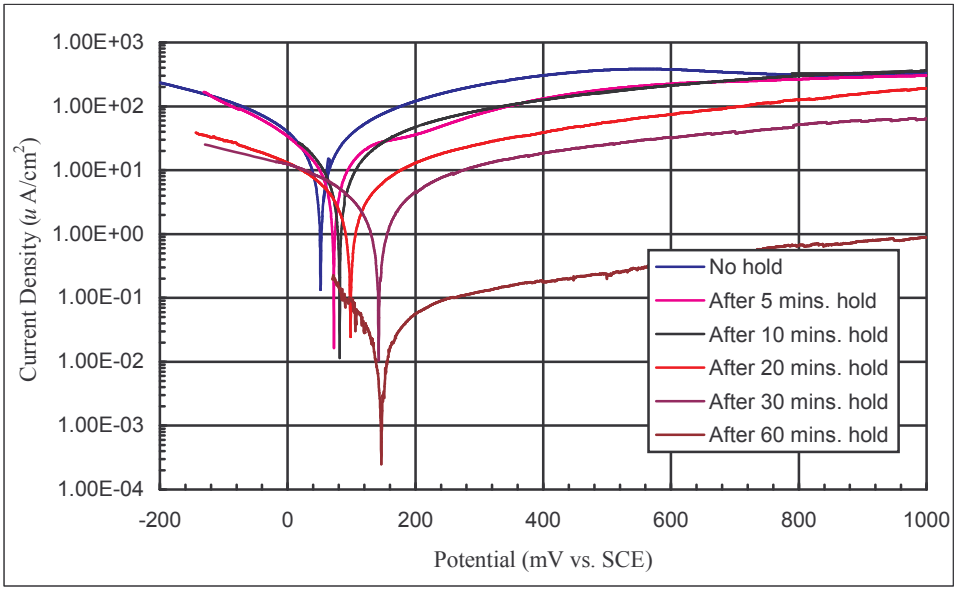


Figure 5.10 Potentiodynamic polarisation scans of SSiC in 1 M HNO_3. Samples were held at +500 mV for 5, 10, 20, 30, and 60 minutes respectively and compared to a normal scan in HNO_3 (without holding) showing decreasing corrosion current density as the holding time is increased.

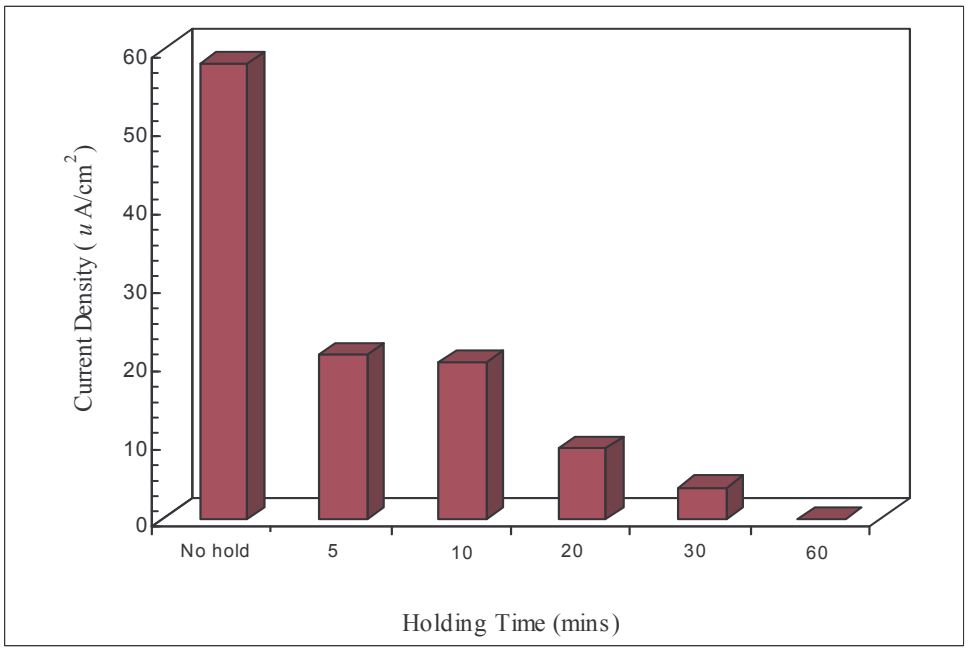


Figure 5.11 Comparison of the corrosion current densities of SSiC in 1 M HNO_3 at different holding times. The corrosion current density decreased as holding time increased.

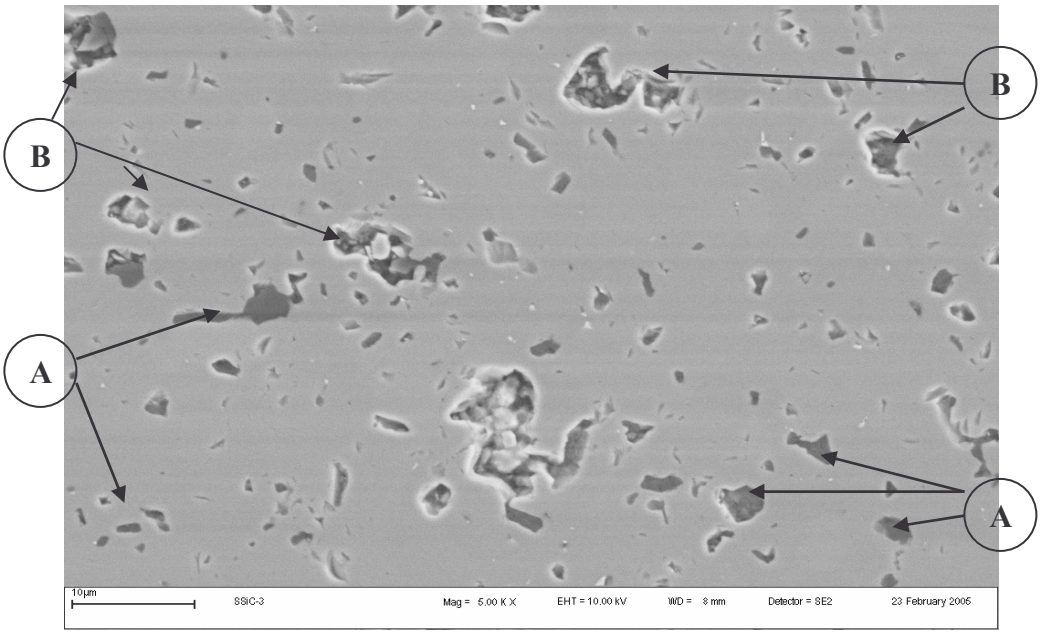


Figure 5.12 Secondary electron SEM micrograph of SSiC after full potentiodynamic scan in 1 M HNO_3. Before scan, the working electrode was held at +500 mV for 20 minutes. The following features are marked: (A) residual carbon and (B) porosity

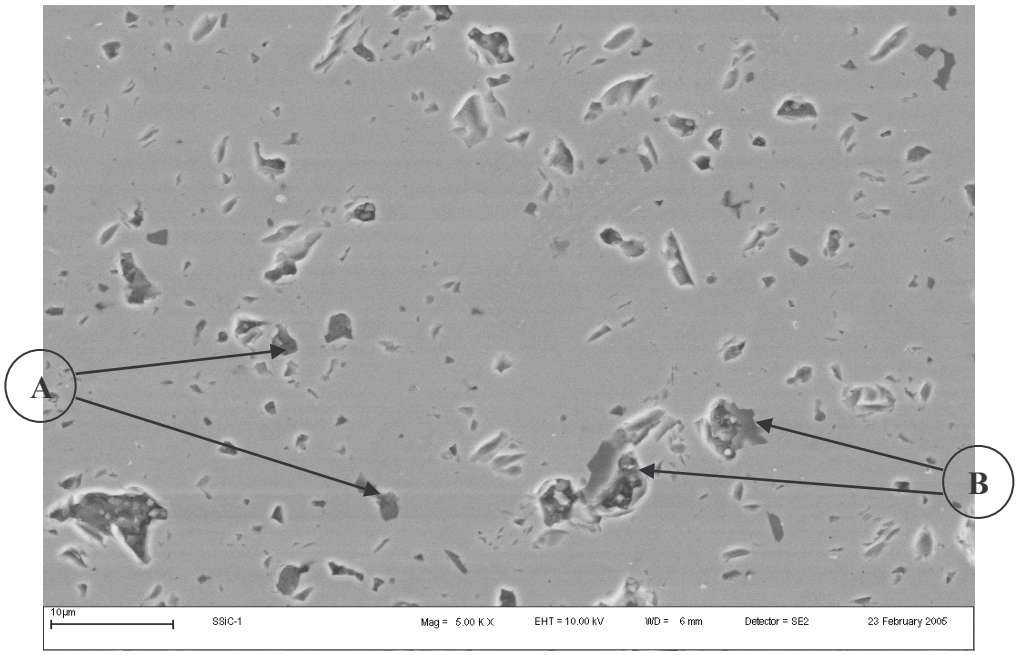


Figure 5.13 Secondary electron SEM micrograph of SSiC after full potentiodynamic scan in 1 M HNO_3. Before scan, the working electrode was held at +500 mV for 60 minutes. The following features are marked: (A) residual carbon and (B) porosity

In figure 5.10, the corrosion current density decreased as the holding time increased compared to the sample without holding (1 and 3 orders of magnitude after 30 and 60 minutes hold, respectively). There were also positive shifts in the open circuit potential as the holding time increased. The polarisation curves after holding did not show any pseudo-passivity features.

The residual carbon seems not to have been affected by corrosive attack; corrosion seems to have occurred mainly at the SiC-C (residual) and SiC-SiC grain boundaries, respectively (compare figures 5.12 and 5.13).

The corroded surface was further analysed with XRD. The intensities (height) of the residual carbon, in principle, are expected to decrease as it dissolves out. The results of the XRD scan before corrosion and after corrosion on the sample held at +500 mV for 20 minutes in 1 M HNO_3 are shown in figure 5.14. The intensities of the SiC decreased significantly after corrosion, but those of the residual carbon remained approximately the same, indicating that the residual carbon is not affected by corrosion.

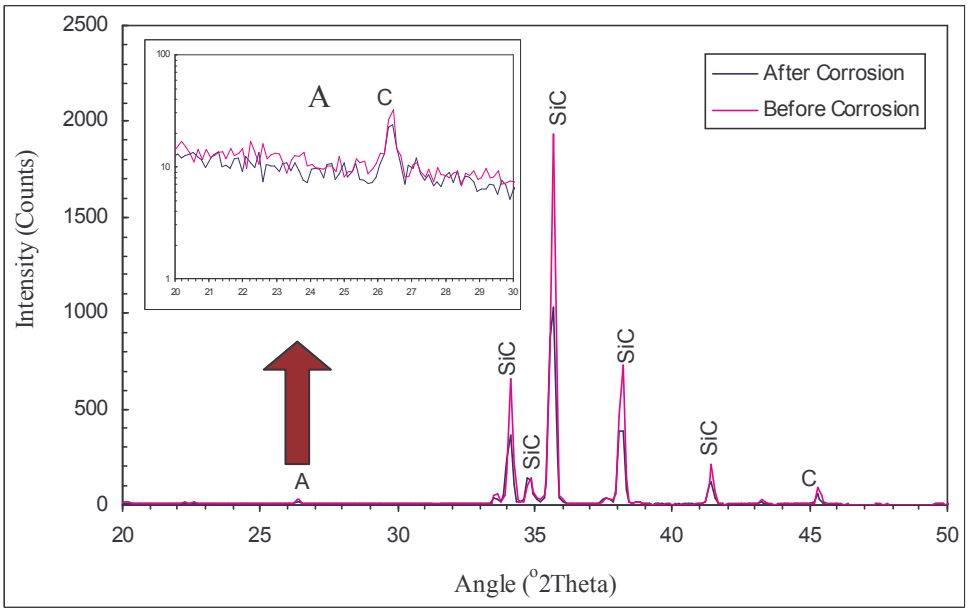


Figure 5.14 XRD pattern of SSiC before and after holding the sample in 1 M HNO_3 at +500 mV for 20 minutes before performing full potentiodynamic scan. The enlargement of peak "A" is shown in the insert. There was no change in the intensity (height) of the residual carbon.

The surface of the sample after 60 minutes hold before scan was also analysed with Raman spectrometer and scanning X-ray photoelectron spectroscopy (SXPS). A pinhole of 0.5mm was used during Raman Spectroscopy to localise the focal spot to the surface, achieving high beam intensity. The results from the investigations are shown in figures 5.15 to 5.17.

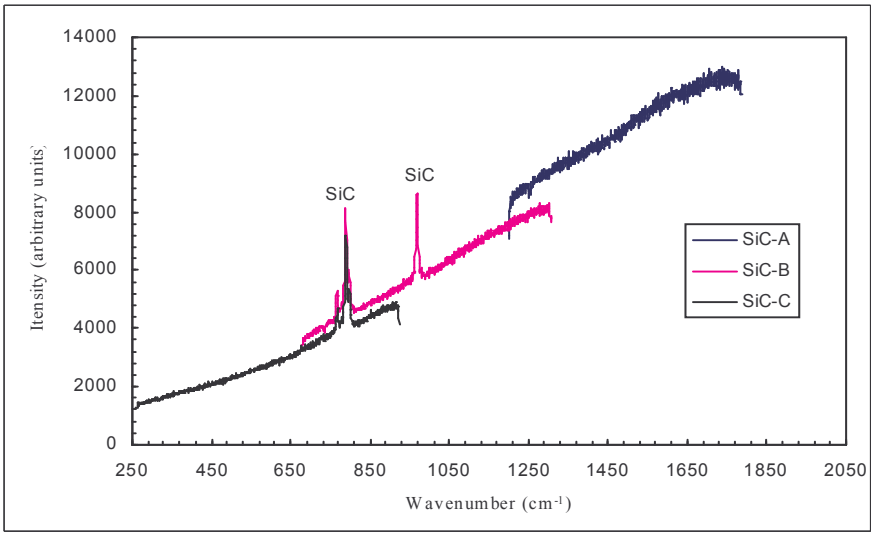


Figure 5.15 Raman spectra of SSiC (as-sintered) before corrosion. SiC-A: 50x objective, 0.5mm pinhole on "clear" area in microscope; SiC-B: same spot as SiC-A, different spectral region; SiC-C: same spot as SiC-A, different spectral region.

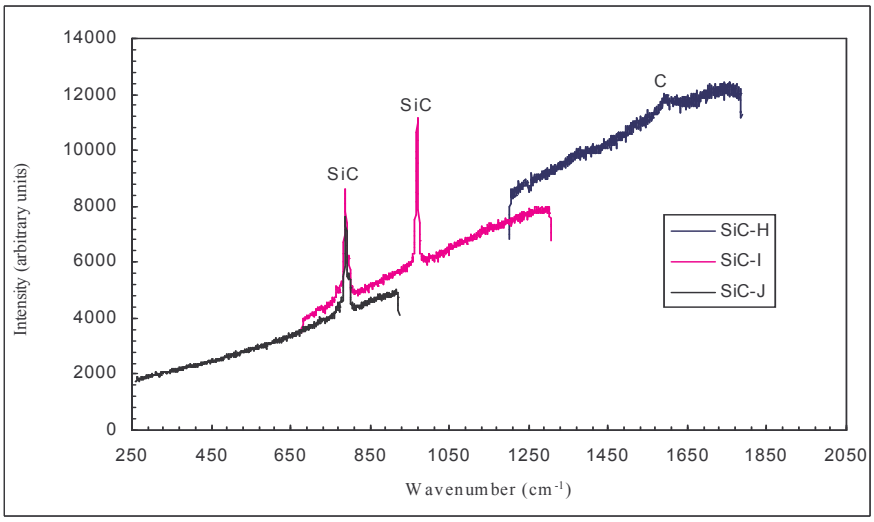


Figure 5.16 Raman spectra of SSiC after holding at +500 mV (vs. SCE) in 1 M HNO_3 for 60 minutes before polarisation scan. SiC-H: 50x objective, 0.5mm pinhole on "clear" area in microscope; SiC-I: same spot as SiC-H, different spectral region; SiC-J: same spot as SiC-H, different spectral region.

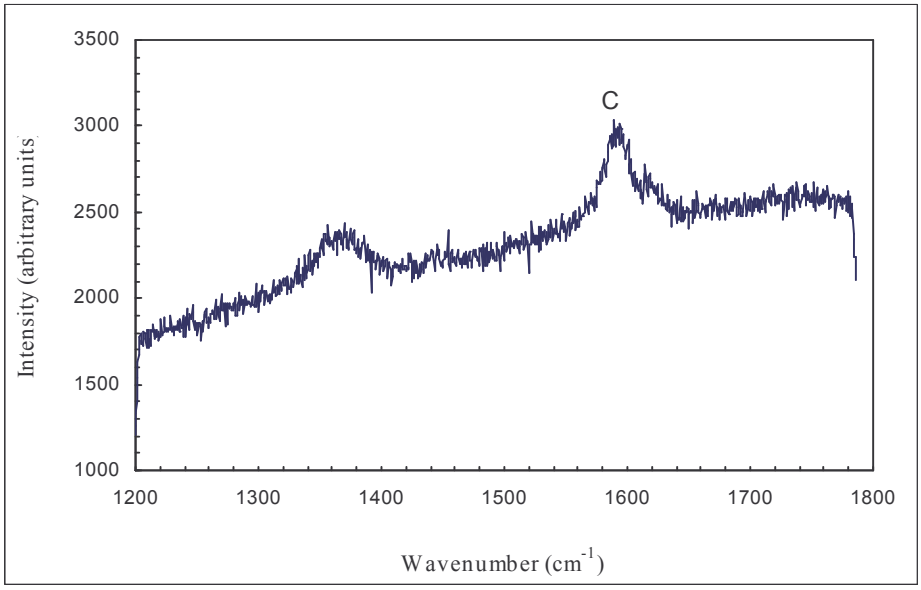


Figure 5.17 Raman spectrum at 50x objective on SSiC (black inclusion) after holding at +500 mV (vs. SCE) in 1 M HNO_3 for 60 minutes.

In figure 5.16, there is some evidence of a thin layer of carbon (amorphous) on the SiC grain, but the peaks are too weak to make any qualitative conclusions. The residual carbon was present (see Figure 5.17). This seems to indicate that the silicon atoms are dissolving out leaving the carbon on the surface.

The surface compositions, determined with scanning X-ray photoelectron spectroscopy (SXPS) show some evidence of silicon oxide layer; however, no quantitative conclusion can be made because of atmospheric contaminations on the fresh (un-corroded) sample surface. The results of the analyses are shown in Appendix B.

The above results show that the residual carbon is not responsible for the corrosion behaviour of SSiC and therefore this hypothesis seems to be not true. The decrease in corrosion current densities as the holding time increased is probably rather due to the formation of an oxide layer on the surface - investigated later, see section 5.3.3. To substantiate this conclusion however, Hypothesis II was postulated and investigated.

Hypothesis II

If reactions 5.8 and 5.10 (SiC/C forming CO_2) are responsible for the corrosion behaviour obtained in HCl and HNO_3, modifying the environment by de-aerating electrolyte with CO_2 gas would force the reactions to occur in the reverse direction, and therefore decrease the corrosion current densities and possibly result in a shift in the open circuit potential.

Samples were prepared for potentiodynamic polarisation scans as described in Chapter 3 (Section 3.4). The solution (1 M HCl) was purged with CO_2 gas (99.0 % purity) for approximately 45 minutes to reduce the dissolved oxygen content and increase the CO_2 concentration. Purging was continued throughout the test. The results of the tests are shown in figure 5.18. A comparison of the behaviour in 1 M HCl, de-aerated with N_2 gas, and 1 M HCl, de-aerated with CO_2 is shown in figure 5.19.

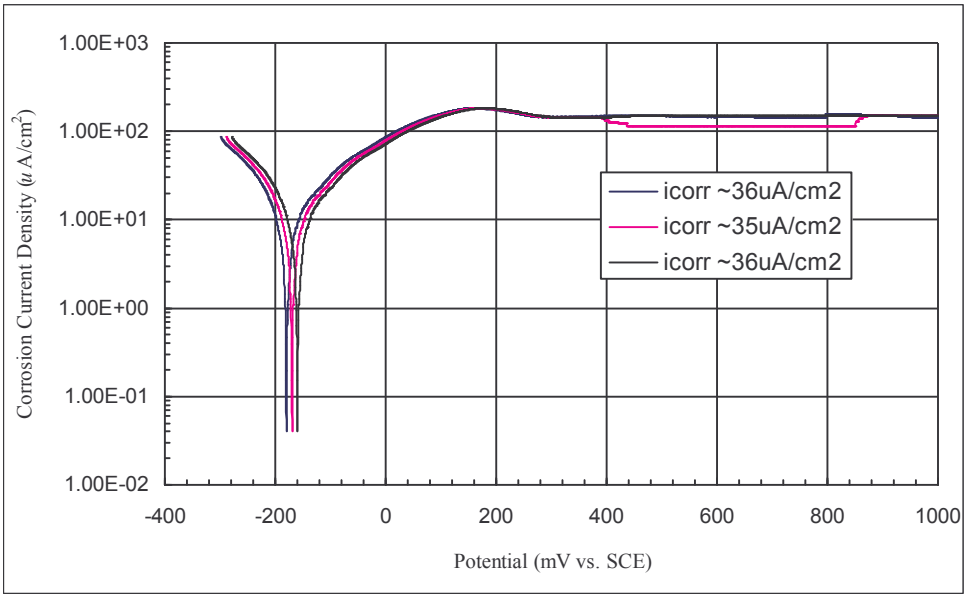


Figure 5.18 Potentiodynamic polarisation scans of SSiC in 1 M HCl showing good reproducibility. The electrolyte was de-aerated with CO_2 gas. Pseudo-passivity was observed at approximately +160 mV.

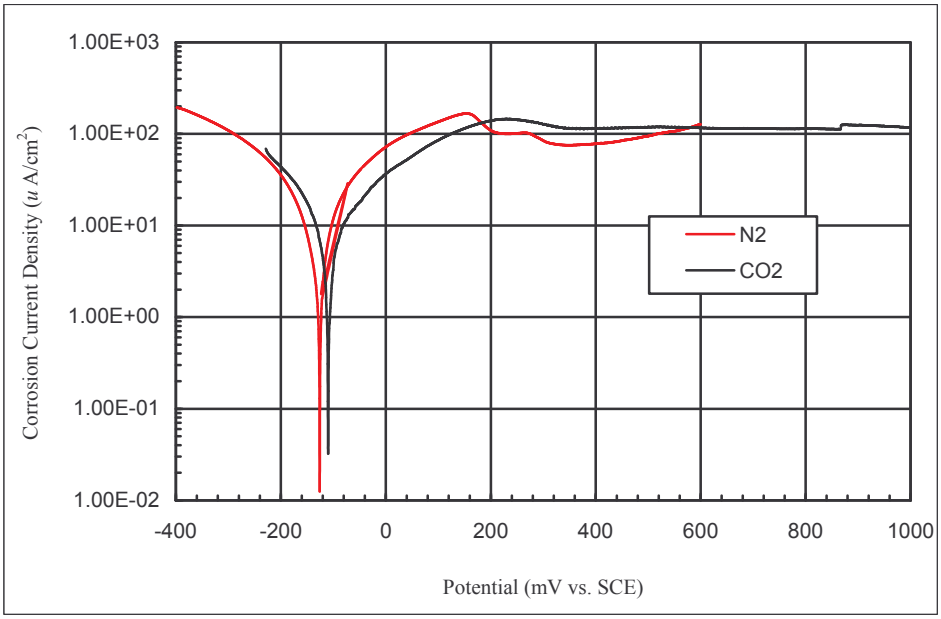


Figure 5.19 Potentiodynamic polarisation scans of SSiC in 1 M HCl indicating approximately the same corrosion current density and open circuit potential when de-aerating with N_2 or CO_2 gas.

The corrosion current densities and the corrosion potentials remained approximately the same; however, the current density drop in CO_2 environment at the passive region was lower (about 20 $\mu A/cm^2$ compared to 75 $\mu A/cm^2$ in N_2 environment).

Since there was no significant change in corrosion current densities or the open circuit potential, it suggests that the reactions do not form CO_2, under these test conditions, and therefore reactions 5.8 and 5.10 do not contribute to the current densities measured. Hypothesis II, is therefore, not probable. The effect of the carbon during corrosion in NaOH environments was investigated through Hypothesis III.

Hypothesis III

If reactions 5.12 and 5.14 (SiC/C forming CO_3^{2-}) are responsible for the corrosion behaviour obtained in NaOH, dissolving sodium carbonate (Na_2CO_3) in NaOH (used as electrolyte) would increase the concentration of CO_3^{2-} ions and thereby force the reactions to occur in the reverse direction, decreasing the current densities and possibly resulting in a shift in the open circuit potential.

Samples were prepared for potentiodynamic polarisation scans as described in Chapter 3 (Section 3.4). 40g of Na_2CO_3 was dissolved in 0.4 litres of NaOH to increase the concentration of the CO_3^{2-} ions. The results of the investigation are shown in figure 5.20. A comparison of the behaviour in 1 M NaOH/Na_2CO_3 and 1 M NaOH is shown in figure 5.21.

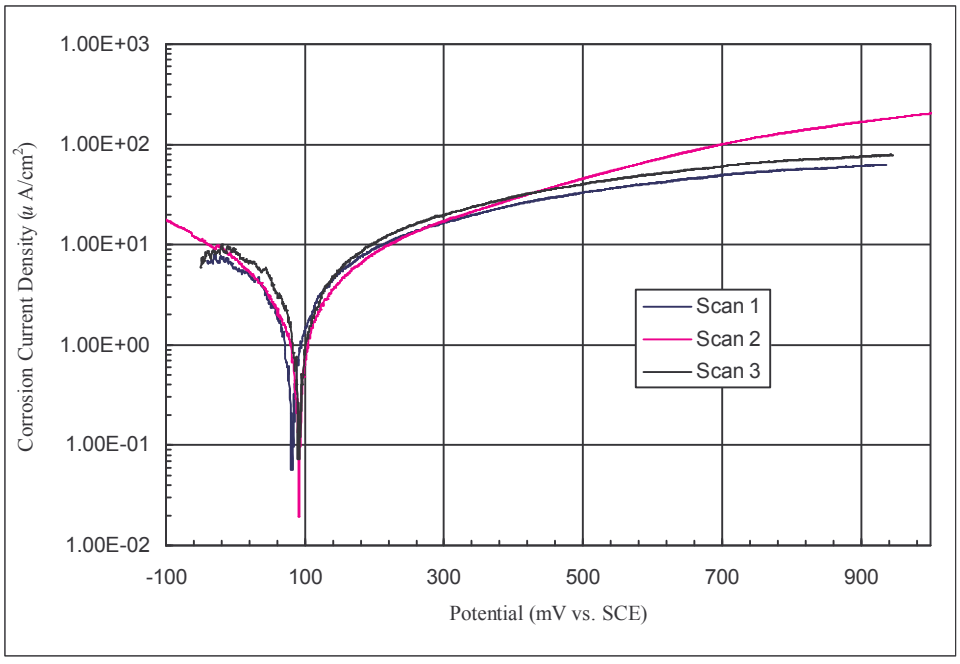


Figure 5.20 Potentiodynamic polarisation scans of SSiC in 1 M NaOH/Na_2CO_3 showing good reproducibility.

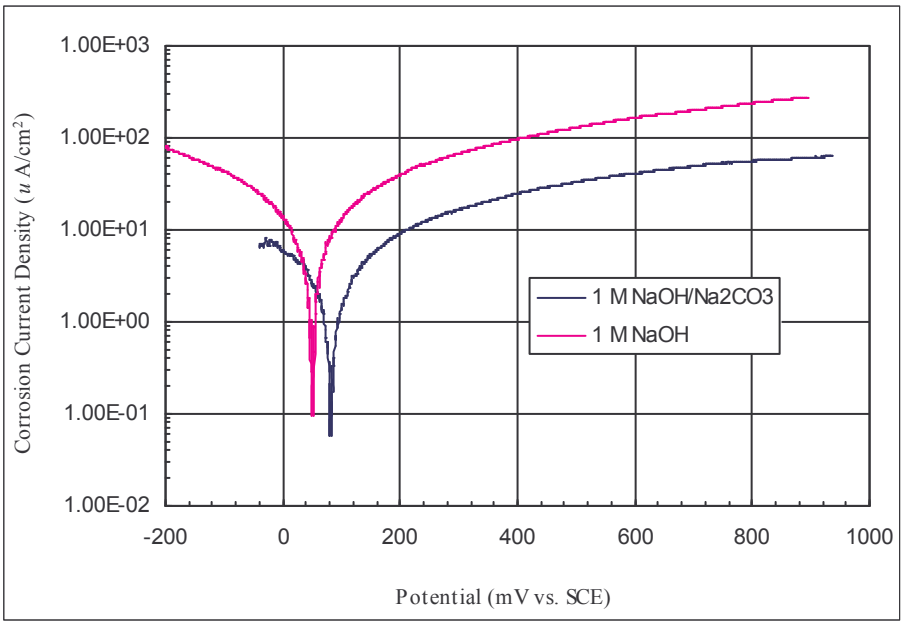


Figure 5.21 Comparison of potentiodynamic polarisation scans of SSiC in 1 M NaOH and 1 M NaOH/Na_2CO_3 indicating lower corrosion current density and a slightly positive shift in open circuit potential when Na_2CO_3 is dissolved in NaOH.

The corrosion current densities were lower in the NaOH/Na_2CO_3 mixture than in the NaOH, the corrosion potentials shifted slightly to the positive.

Since there was a marked change in corrosion current densities as well as the open circuit potential, it suggests that the reactions do form CO_3^{2-} ions in NaOH under test conditions, and therefore reaction 5.14 contributes to the currents measured. Hypothesis III is therefore, probable.

5.3.2 Effect of Silicon

Hypothesis IV

If silicon (in the SiC compound) is responsible for the corrosion behaviour (reactions 5.9, 5.11, 5.13 to 5.15), performing polarisation scans on a pure silicon electrode – measured under identical conditions in HCl, HNO_3 and NaOH solutions – would result in corrosion behaviour similar to SSiC.

Samples were prepared for polarisation scans as described in Chapter 3 (Section 3.4). The results of the investigations are shown in figures 5.22 to 5.24.

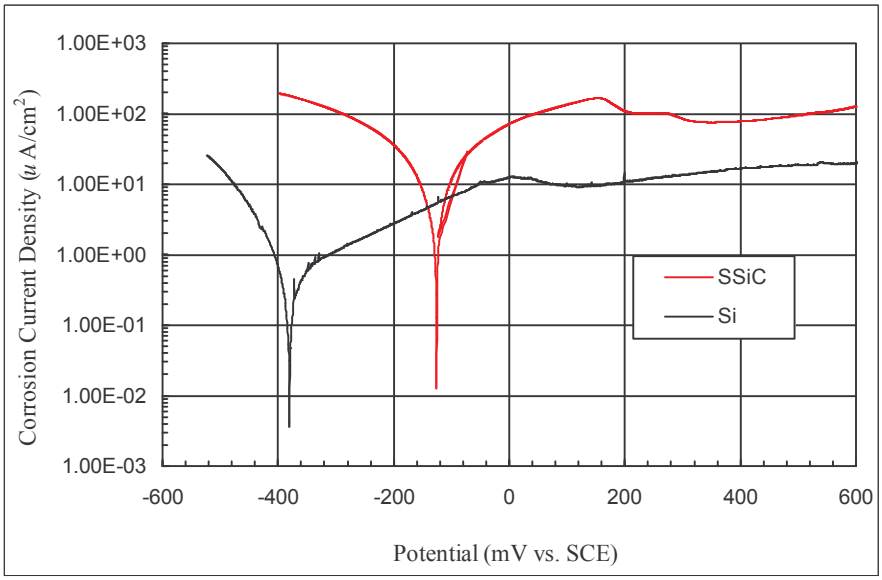


Figure 5.22 Potentiodynamic polarisation scans of SSiC and pure Si in 1 M HCl showing higher corrosion current density for SSiC material.

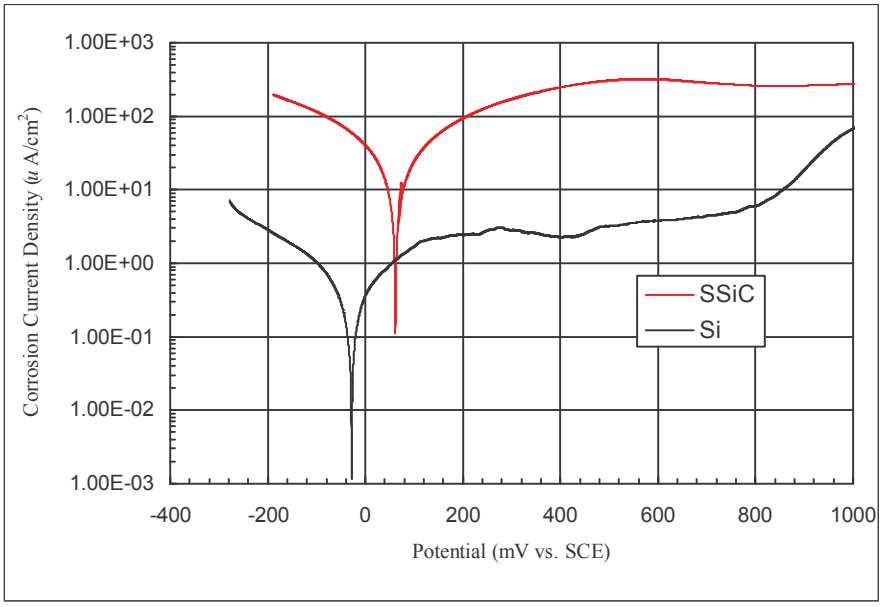


Figure 5.23 Potentiodynamic polarisation scans of SSiC and pure Si in 1 M HNO_3 showing higher corrosion current density for SSiC material.

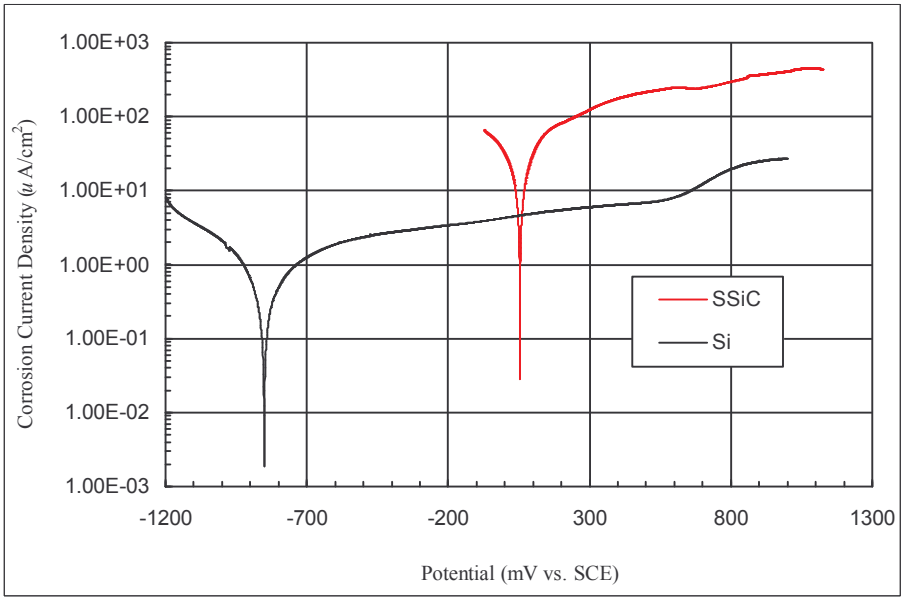


Figure 5.24 Potentiodynamic polarisation scans of SSiC and pure Si in 1 M NaOH showing higher corrosion current density for SSiC material.

In all three environments, the active dissolution of SSiC was higher than that of pure Si in the same environments. There is also a general shift in the open circuit potential in the different corrosive media; the materials were more noble in HNO_3 (see figures 5.25 and 5.26). The shift in SSiC E_{corr} is not as large as for the Si E_{corr}.

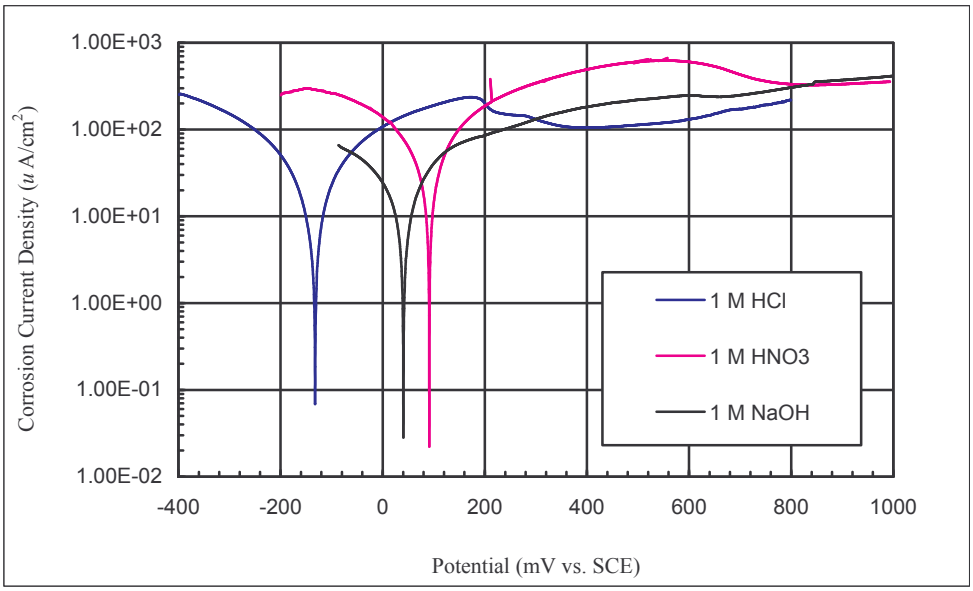


Figure 5.25 Comparison of potentiodynamic polarisation scans of SSiC in the different corrosive media.

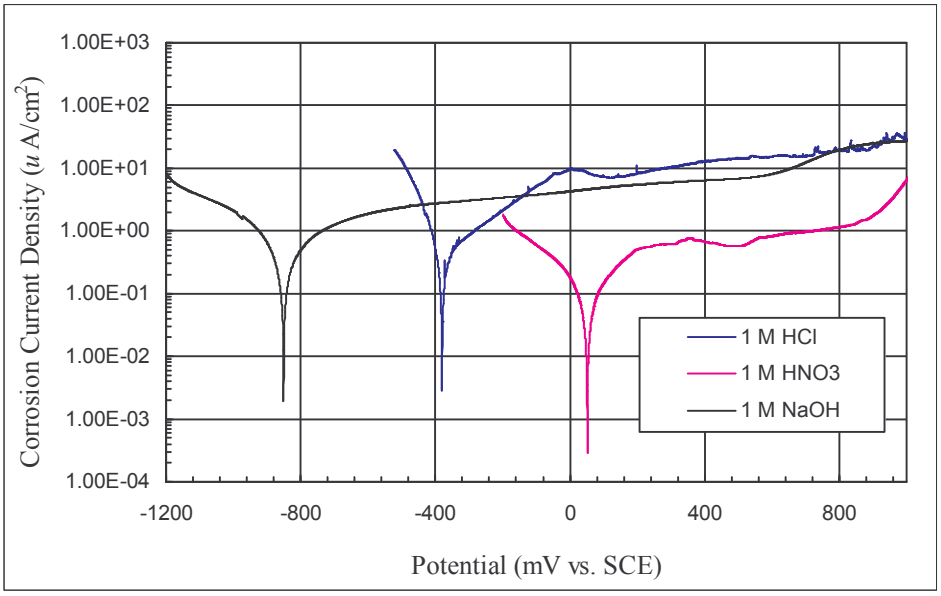


Figure 5.26 Comparison of potentiodynamic polarisation scans of Si in the different corrosive media.

In figures 5.22 to 5.24, a difference in potential of about 250 mV (in HCl), 45 mV (in HNO_3), and 800 mV (in NaOH) is observed, indicating the more noble character of SSiC compared to pure Si. The difference in current density could be due to the electrochemical dissolution of carbon to form CO. On the other hand, it could be possible that there is a preferential dissolution of Si at the SiC-$C_{residual}$ and SiC-SiC grain boundaries (see figures 5.12 and 5.13). The corrosion behaviour of Si in HCl is similar to SSiC, indicating the likelihood of Si playing a major role in the corrosion mechanism of SSiC.

The polarisation curves for Si in HCl and HNO_3 were characterised by slight pseudo-passive behaviour. The pseudo-passive behaviour could also be observed for SSiC materials in the same environments. This suggests that the pseudo-passivity observed for SSiC in acidic environments could be as a result of one of two reasons: (1) the formation of an oxide layer on the surface; (2) a thin carbon layer on the surface of

the sample as a result of the carbon not dissolving in the test conditions, as shown in the Raman spectrum in figure 5.16.

The active dissolution of Si and SSiC in NaOH followed the same trend (see figure 5.24) with the formation SiO_3^{2-} ions in solution because of the high pH values and high potentials (Pourbaix *et al*., 1958). A Pourbaix diagram for the Si-H_2O system (Figure 5.27) could be used to explain the mechanism of solid Si dissolution in acidic and alkaline environments (Antelman, 1982; Bard *et al*., 1985; Pourbaix *et al*., 1958). In figures 5.27 and 5.28, lines (1'), (2'), (4), (5) and (6) represent the influence of pH on the solubility of silica.

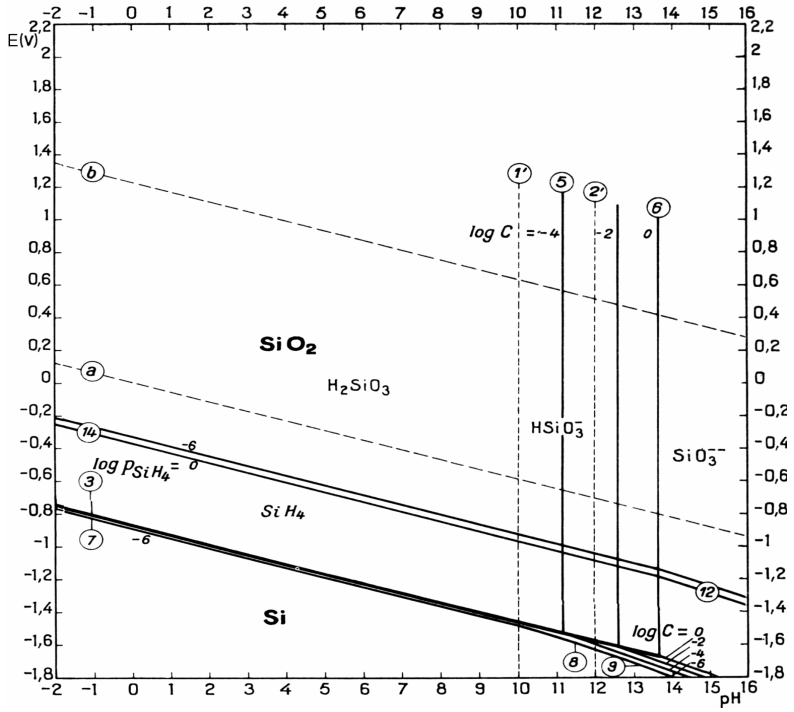


Figure 5.27 An approximate potential-pH equilibrium diagram for the system silicon-water, at 25°C, considering SiO_2 in the form of quartz (Pourbaix *et al*., 1958).

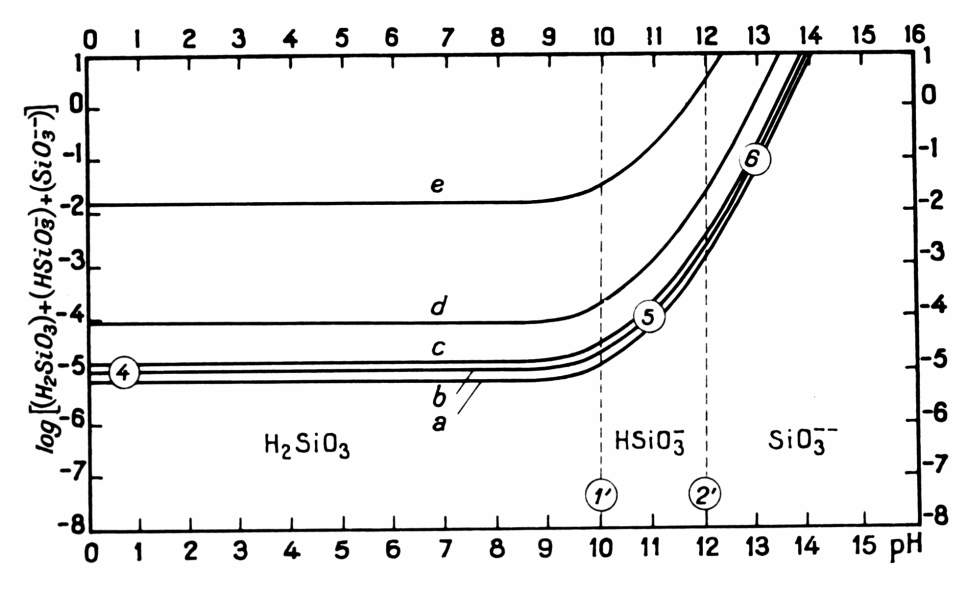


Figure 5.28 Influence of pH on the solubility of SiO_2 at 25°C. a, quartz; b, cristobalite; c, tridymite; d, vitreous silica; e, amorphous silica (Pourbaix *et al*., 1958)

In figure 5.27, at about -0.8 V (SHE) (or +1.04 V (SCE)), the stable phase in acidic environments is SiO_2. This silica will dissolve as the pH of the solution increases (Figure 5.28). The measured pH value for the HCl and HNO_3 solutions of this investigation were 0.08 and 0.07, respectively. This suggests that the anodic dissolution reaction of SiC in HCl and HNO_3 is the oxidation of SiC to SiO_2 (reactions 5.9 to 5.11). Pseudo-passivity features were observed at approximately +160 mV in HCl and at about +700 mV in HNO_3. This seems to suggest the presence of an oxide layer (SiO_2) on the SSiC surface during corrosion. The evidence of such a SiO_2 layer on SSiC and RBSiC was also observed by Cook *et al*. (1994).

At high pH's (> 10), silicates are formed (see Figures 5.27 and 5.28). This means that the Si will continuously react and form silicate product in alkaline environments. Even though there is no significant difference in corrosion current density between acidic and alkaline environments in the test results, it is expected that when exposed for longer periods, Si will corrode more in alkaline environments than in acidic

environments because of the SiO_3^{2-} ions formed in alkaline environments. Thus, if Si is the main atom contributing to the corrosion behaviour of SSiC materials, then the concentration of silicate ions in alkaline environments will play a major role in the kinetics of the process.

Since there were similarities in the corrosion behaviour of Si and SSiC in both acid and alkaline environments, it suggests that Hypothesis IV, namely that the dissolution of Si is responsible, or at least partly responsible, for the corrosion behaviour, is likely.

5.3.3 Investigation of the Formation of SiO_2 / SiO_3^{2-}

Hypothesis V

If the oxidation of SiC leads to the formation of SiO_2 in acidic environments (reactions 5.9 to 5.11), holding the sample at a more positive potential for a while in HNO_3 will increase corrosion and thereby form more SiO_2 on the surface. Performing potentiodynamic testing on the sample would lead to a decrease in corrosion current densities because of the protective oxide layer. Likewise, if the sample is held at a more positive potential for a period of time to allow SiO_2 to form, followed by immersion in hydrofluoric acid (HF), the SiO_2 would dissolve (Bard *et al*., 1986; Pourbaix *et al*., 1958), and in performing potentiodynamic testing on this sample an increase, rather than decrease in the corrosion current densities would be observed.

On the other hand, holding the sample at a more positive potential for a period of time in NaOH would increase corrosion and thereby form more SiO_3^{2-} ions in solution (reactions 5.13 to 5.15) in solution (Antelman, 1982; Bard *et al*., 1985; Pourbaix *et al*., 1958). Performing potentiodynamic testing on this sample would lead the same or increased current densities compared to a full normal scan (without holding).

Samples for the tests were prepared as described in Chapter 3 (section 3.4). SSiC was held at +500 mV (vs. SCE) in 1 M HNO_3 for 20 and 30 minutes, respectively before performing potentiodynamic tests. The scan results were compared to the normal scan (without holding). Another sample was held at +500 mV (vs. SCE) in 1 M HNO_3 for 30 minutes after which it was removed and immersed in hydrofluoric acid (1 M HF) for 10 minutes (personal conversation with Dr. M. Herrmann) without applying potential. The sample, after 10 minutes immersion in HF, was immersed in 1 M HNO_3 and a full potentiodynamic scan performed. The results of the investigation are shown in figure 5.29.

The current densities, after 10 minutes immersion in HF, were higher than the 20 and 30 minutes hold scan. This strongly suggests that an oxide layer (SiO_2) forms on the surface in acidic environments and is responsible for the reduction in corrosion rate.

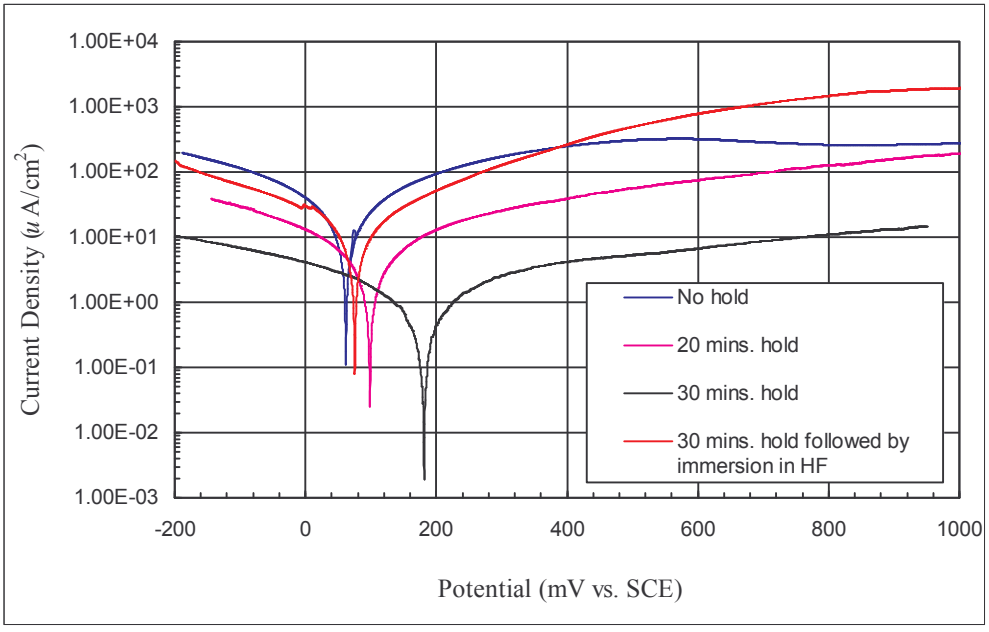


Figure 5.29 Potentiodynamic polarisation scans of SSiC in 1 M HNO_3. Samples were held at +500 mV for 20 and 30 minutes, respectively and compared to a normal scan in 1 M HNO_3 (without holding). A sample was also held at +500 mV for 30 minutes in 1 M HNO_3, followed by 10 minutes immersion in HF, before performing a full scan.

Similarly, another sample was exposed to 1 M NaOH at +500 mV (vs. SCE) for 30 minutes before performing potentiodynamic test and compared to the normal scan (without holding). The result of the investigation is shown in figure 5.30.

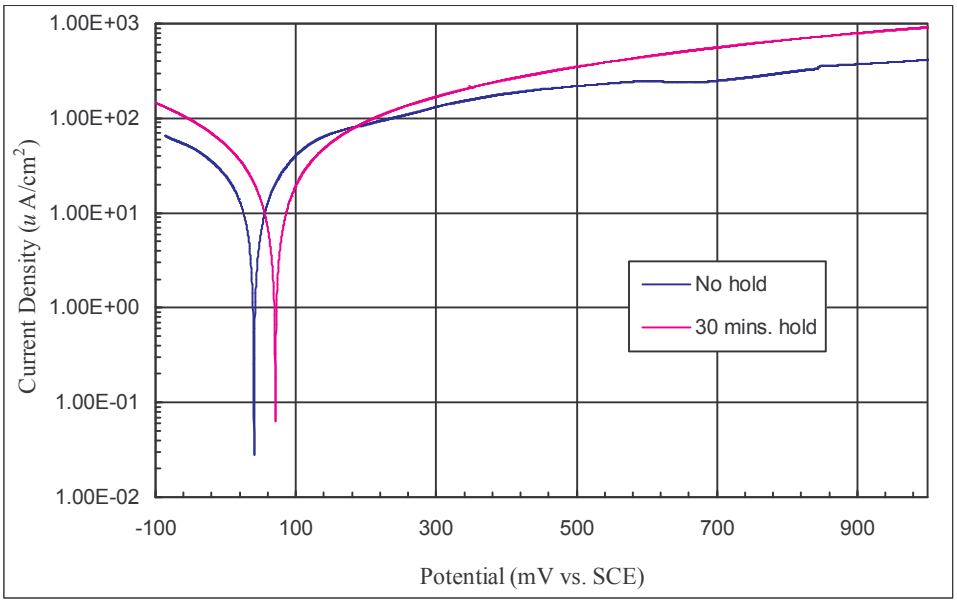


Figure 5.30 Potentiodynamic polarisation scans of SSiC in 1 M NaOH. Samples were held at +500 mV for 30 minutes and compared to a normal scan in HNO_3 (without holding)

In the alkaline environment, the current densities after 30 minutes hold in NaOH before scanning were approximately the same as without holding. This suggests that no protective layer forms during holding and rather, with longer times in the corrosive environment (that is, during holding and scanning) SiC progressively corrodes to form SiO_3^{2-} ions. Hypothesis V, that Si (in the SiC compound) forms SiO_2 and SiO_3^{2-} in acidic and alkaline environments, respectively, is therefore likely.

This means that the results obtained in Hypothesis I (that is the decrease in current densities with increasing holding times – Figure 5.10) is not a result of depletion of

the residual carbon after holding at +500 mV before scans (as already alluded to be the results of section 5.3.1), but rather due to a build-up of oxide (SiO_2) during holding. The lowering of anodic currents could possibly be due to the oxide layer thickness increasing with longer holding times. If an existing oxide layer is on the sample surface, the corrosion rate will be less than that of a sample with a thin or no oxide layer. The build-up of the oxide layer would also make the exposed surface passive and performing potentiodynamic scans on this surface would result in a positive shift in the E_{corr}. It is probable that no pseudo-passivity was observed because there was already an oxide layer on the surface. The lowering of anodic current due to the oxide layer thickness was also found by Cook *et al*. (1994).

5.4 Conclusion

The residual carbon seems not to have dissolved in either acidic or alkaline environments under these test conditions. One reason could be that the corrosion reaction potential measured in acidic environments using polarisation methods was lower than the potential calculated thermodynamically, which means that the reaction cannot take place (Jones, 1996). In addition to the lower positive potential measured, the SEM micrographs and XRD results showed no attack on the residual carbon. Secondly, the formation of CO_2 in acidic environments seems not feasible under these test conditions, since increasing the CO_2 concentration in the electrolyte did not decrease the corrosion current densities measured (see figure 5.19). The formation of CO_3^{2-} ions in alkaline environments seems to be more feasible (Figure 5.21).

The corrosion current densities of SSiC were higher than those of the pure Si, due to the lower activity of Si in SiC in comparison to pure Si. Table 5.1 summarises the polarisation results obtained.

Table 5.1 Summary of polarisation results of SSiC and Si materials

Material	Condition (s)	Corrosion Potential (mV vs. SCE)	Corrosion Potential (mV vs. SHE)	Current Density, i_{corr} ($\mu A/cm^2$)
SSiC	1 M HCl	-125	+116	46
	1 M HNO_3	+77	+318	58
	1 M NaOH	+53	+294	33
	1 M HNO_3 (30 mins hold)	+183	+424	2
	1 M HNO_3 + 1 M HF	+78	+319	40
	1 M NaOH (30 mins hold)	+73	+314	35
Si	1 M HCl	-380	-139	1
	1 M HNO_3	-26	+215	0.7
	1 M NaOH	-846	-605	0.9

It therefore seems likely that reactions 5.8, 5.10 and 5.12 are not feasible, and that the following reactions are responsible for the electrochemical corrosion response measured:

Acidic environments

$$SiC(s) + 2H_2O(l) \rightarrow SiO_2(s) + C + 4H^+(aq) + 4e^- \qquad E^o = -1.07 \text{ V} \qquad [5.9]$$

$$SiC(s) + 3H_2O(l) \rightarrow SiO_2(s) + 6H^+(aq) + CO(g) + 6e^- \qquad E^o = -0.542 \text{ V} \qquad [5.11]$$

Alkaline environments

$$SiC(s) + 6OH^-(aq) \rightarrow SiO_3^{2-}(aq) + C + 3H_2O(l) + 4e^- \qquad E^o{}_B = -1.874 \text{ V} \qquad [5.13]$$

$$SiC(s) + 12OH^-(aq) \rightarrow SiO_3^{2-}(aq) + 5H_2O(l) + CO_3^{2-}(aq) + 8e^-$$

$$E^o{}_B = -0.076\,\text{V} \qquad [5.14]$$

$$SiC(s) + 8OH^-(aq) \rightarrow SiO_3^{2-}(aq) + 4H_2O(l) + CO(g) + 6e^-$$

$$E^o{}_B = -0.8\,\text{V} \qquad [5.15]$$

Even though there is no significant difference in corrosion current densities in acidic and alkaline environments in these test results, it is expected that when exposed for longer periods, SSiC will corrode more in alkaline environments than in acidic environments because a protective SiO_2 layer forms in acidic environments, but not in alkaline environments. This agrees with other investigators that showed the rate of dissolution of SiC to be high in alkaline environments but not so high in acidic environments with immersion testing (Lay, 1983).

CHAPTER 6

CORROSION OF LIQUID PHASE SINTERED SILICON CARBIDE (LPSSiC)

6.1 Introduction

After characterising the LPSSiC materials, corrosion tests were performed on them in acidic and alkaline environments. The test results are presented first, followed by two hypotheses that were proposed to explain the corrosion behaviour of LPSSiC materials and the possible effect of the secondary phase on the corrosion mechanisms.

6.2 Electrochemical Behaviour

Results of the corrosion behaviour of the LPSSiC materials in the different electrolytes are presented on semi-logarithmic plots along with their microstructural changes after the polarisation scans. The electrolytes were chosen to assist in the general understanding of the corrosion mechanisms of LPSSiC ceramics in acidic and alkaline environments.

6.2.1 Corrosion behaviour in HCl

The potentiodynamic polarisation scans on LPSSiC-1and LPSSiC-2 specimens in 1 M HCl are shown in figures 6.1 and 6.3, respectively. SEM micrographs after polarisation scans are shown in figures 6.2 and 6.4.

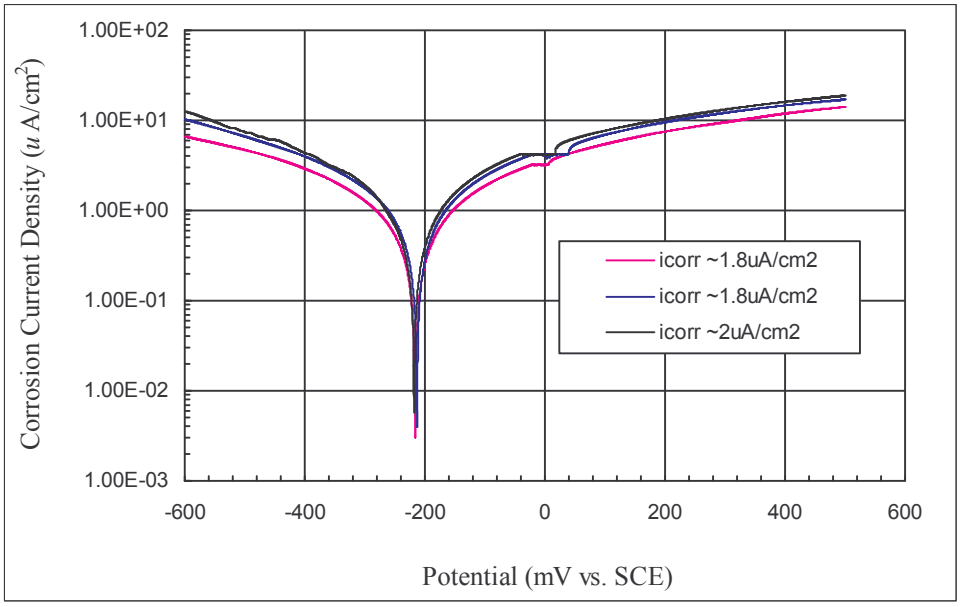


Figure 6.1 Potentiodynamic polarisation scans of LPSSiC-1 in 1 M HCl showing good reproducibility. The average corrosion current density is ~2 $\mu A / cm^2$.

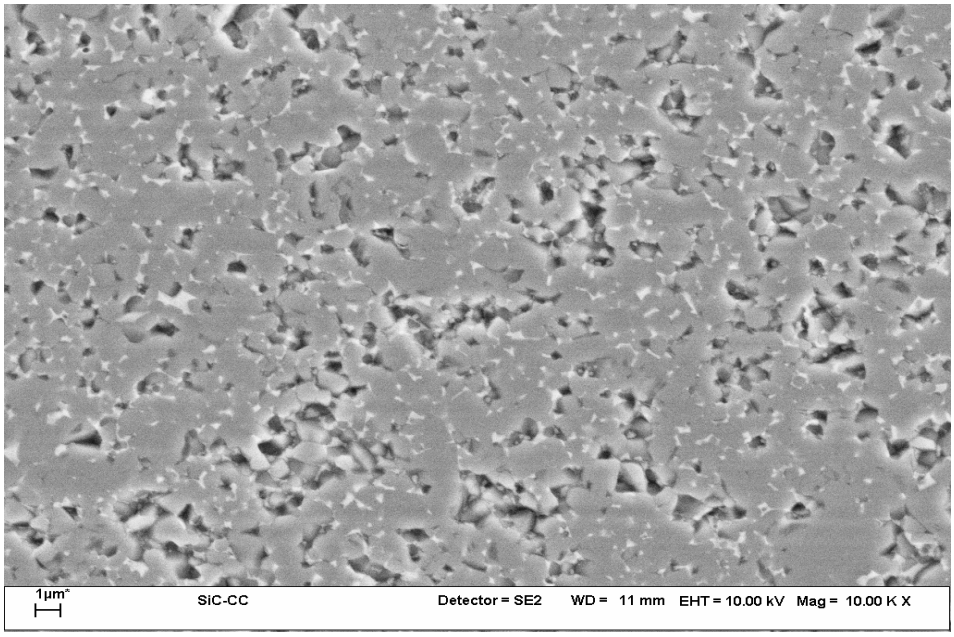


Figure 6.2 Secondary electron SEM micrograph of LPSSiC-1 after full potentiodynamic scan in 1 M HCl. Corrosion is visible at the secondary phase.

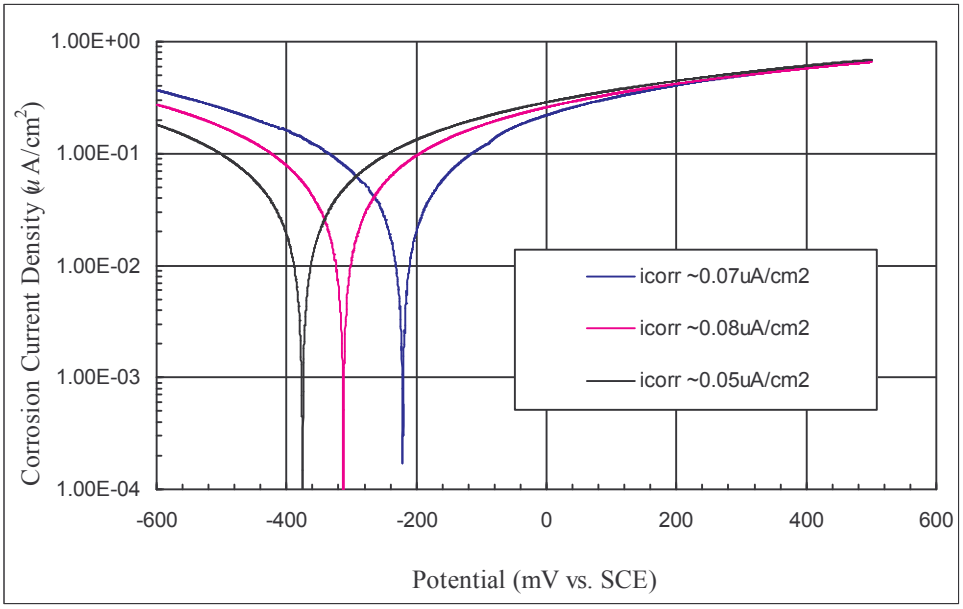


Figure 6.3 Potentiodynamic polarisation scans of LPSSiC-2 in 1 M HCl. Corrosion potential is not reproducible; however, the corrosion current densities are approximately the same. The average corrosion current density is ~0.07 $\mu A / cm^2$.

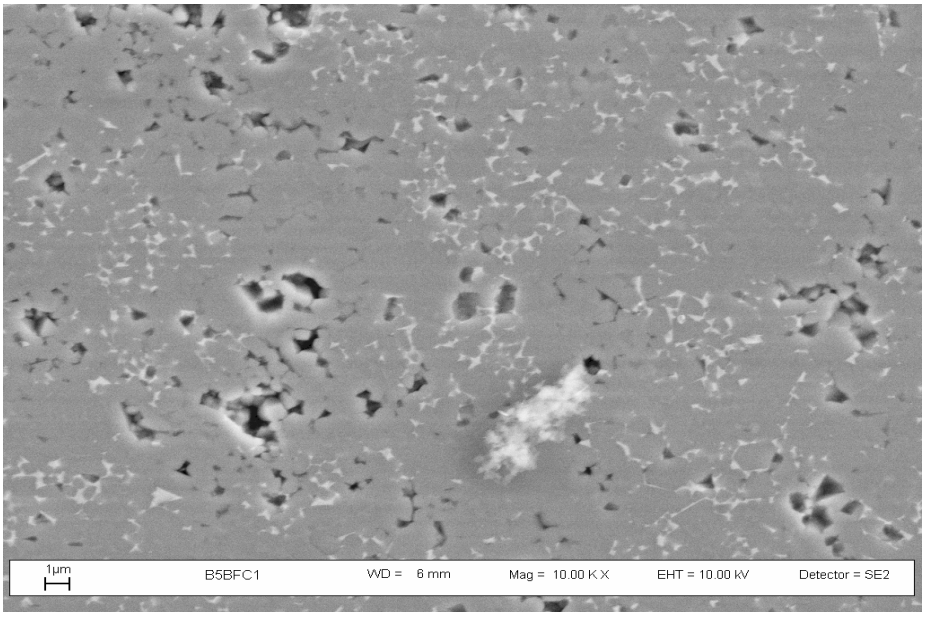


Figure 6.4 Secondary electron SEM micrograph of LPSSiC-2 after full potentiodynamic scan in 1 M HCl. Corrosion is visible at the secondary phase.

The reproducibility of results of the LPSSiC-1 in HCl was good, but with LPSSiC-2, scatter was obtained. Even though it was intended to use a scan width of about -200 mV to about +1000 mV relative to the open circuit potential, it was not possible due to unpredictable shifts in the open circuit potential. Samples were re-polished and used in the subsequent scans. The non-reproducibility of the corrosion potential could be due to the electrical resistivity of the LPSSiC ceramics, which depends on the amount and the nature of the secondary phase located at the grain boundaries (Pelissier *et al*., 1998). As could be seen from the results (Figures 6.1 and 6.3), there was more scatter with LPSSiC-2 (having excess alumina) than with LPSSiC-1.

The average corrosion current densities for LPSSiC-1 and LPSSiC-2 were $\sim 2\,\mu A/cm^2$ and $\sim 0.07\,\mu A/cm^2$, respectively. The low corrosion current density for LPSSiC-2 seems to be connected to the excess alumina content; however the exact reaction mechanism is unclear.

The SEM micrographs (Figures 6.2 and 6.4) of the materials show significant surface damage after scanning in 1 M HCl. The secondary phase was preferentially attacked. The dissolution of the secondary phase is not homogenous; whereas alumina undergoes intensive dissolution in acidic environments, yttria is fairly stable in these environments, leaving yttria only slightly affected by corrosion.

6.2.2 Corrosion behaviour in HNO_3

The polarisation results of LPSSiC materials and the SEM micrographs after scanning in 1 M HNO_3 are shown in figures 6.5 to 6.8. The corrosion behaviour in HNO_3 was similar to that in HCl, with only a slight increase in average corrosion current density; $\sim 6\,\mu A/cm^2$ for LPSSiC-1 and $\sim 0.09\,\mu A/cm^2$ for LPSSiC-2. The open circuit potentials shifted to more positive values in comparison to HCl, indicating the slightly more noble behaviour of LPSSiC materials in HNO_3 than in HCl.

After scanning in 1 M HNO_3, corrosion damage was visible at the secondary phase as shown by the SEM micrographs in figures 6.6 and 6.8. The attack on the secondary phase was more for LPSSiC-1 than for LPSSiC-2 material. Not all the secondary phases were preferentially dissolved. As mentioned, this is probably due to the relatively stable nature of yttria in acidic environments.

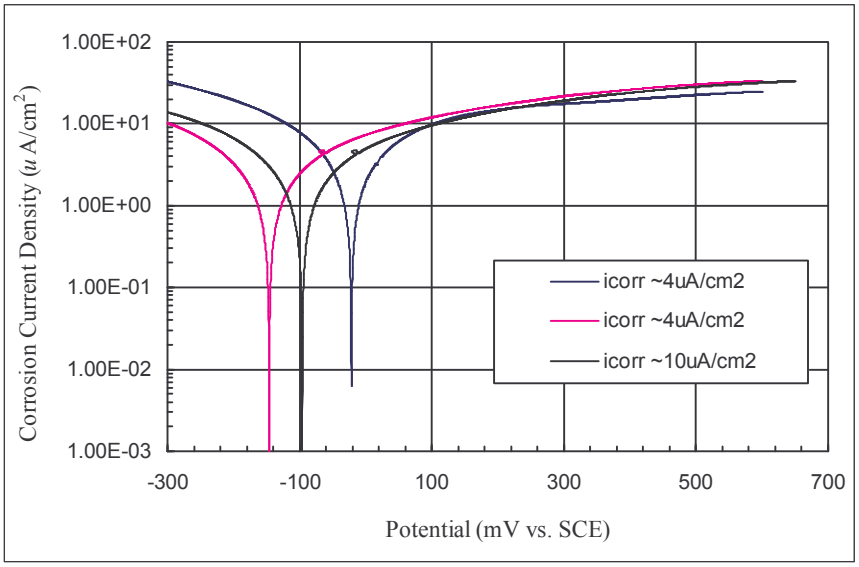


Figure 6.5 Potentiodynamic polarisation scans of LPSSiC-1 in 1 M HNO_3. Corrosion potential is not reproducible and shifts are unpredictable. However, the corrosion current densities are approximately the same. The average corrosion current density is ~6 $\mu A / cm^2$.

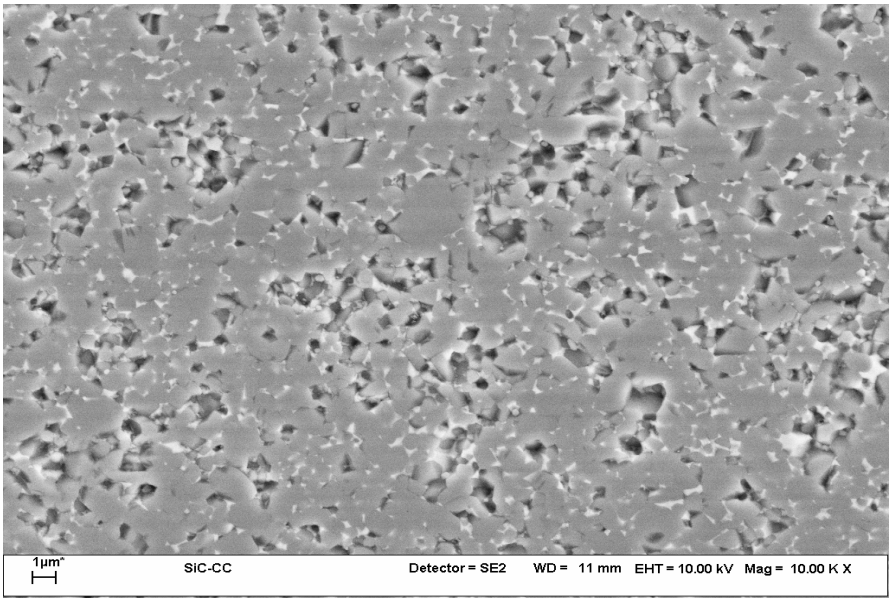


Figure 6.6 Secondary electron SEM micrograph of LPSSiC-1 after full potentiodynamic scan in 1 M HNO_3. Corrosion is visible at the secondary phase.

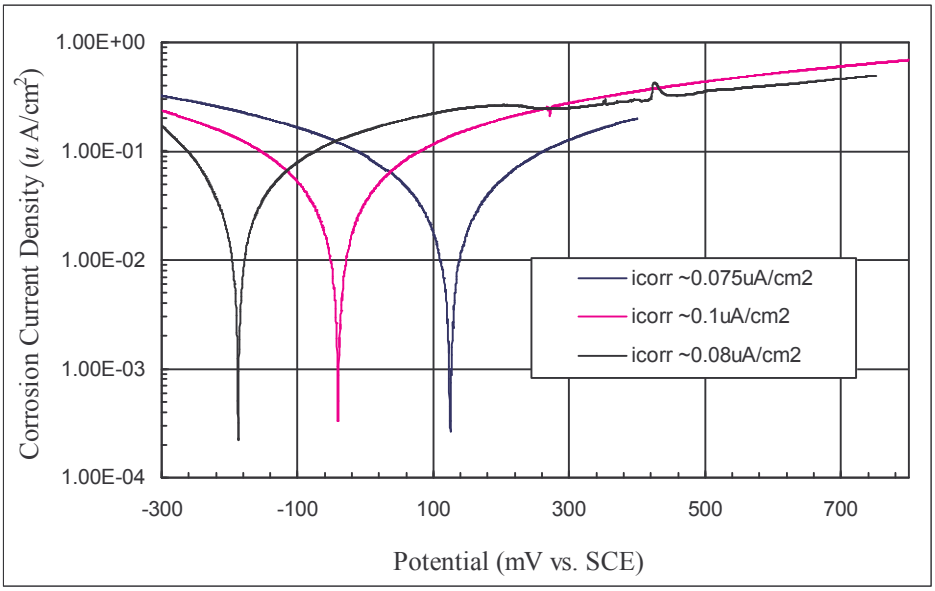


Figure 6.7 Potentiodynamic polarisation scans of LPSSiC-2 in 1 M HNO_3. Corrosion potential shifts to more active values with each scan. However, the corrosion current densities are approximately the same. The average corrosion current density is ~0.09 $\mu A / cm^2$.

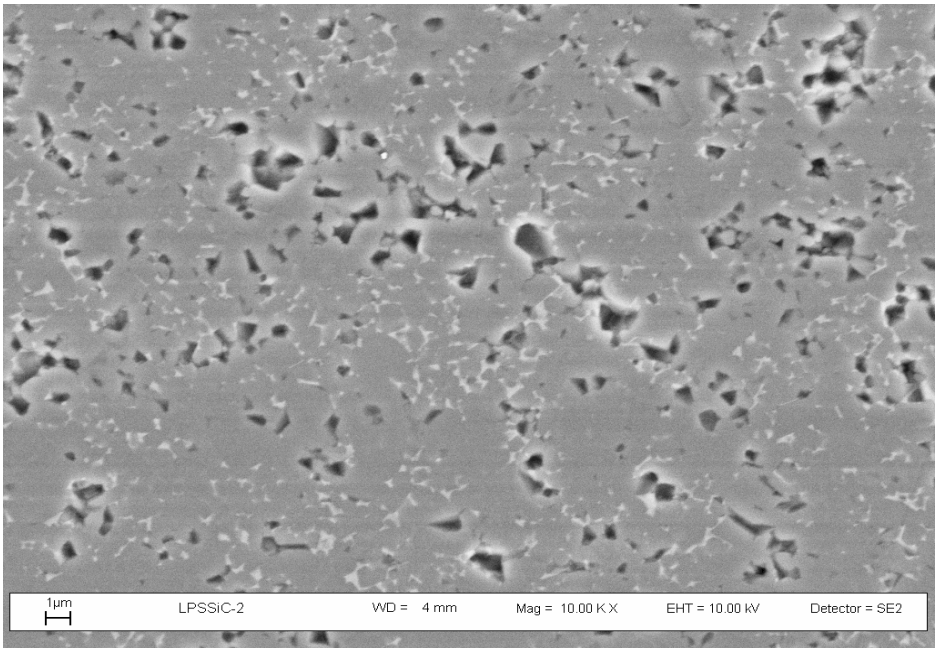


Figure 6.8 Secondary electron SEM micrograph of LPSSiC-2 after full potentiodynamic scan in 1 M HNO_3. Corrosion is visible at the secondary phase.

6.2.3 Corrosion behaviour in NaOH

The potentiodynamic polarisation scans on the materials in 1 M NaOH, along with the SEM micrographs, are shown in figures 6.9 to 6.12. Results of the corrosion potentials were not reproducible. The average corrosion current density for LPSSiC-1 and LPSSiC-2 were ~1.8 $\mu A/cm^2$ and ~0.06 $\mu A/cm^2$, respectively.

After scanning in NaOH, the surfaces were not as severely damaged as in the acidic environments. This is probably due to the formation of $Y(OH)_3$ (Bard *et al*., 1985). Unlike in HCl and HNO_3, the porosity after corrosion was about the same for both LPSSiC-1 and LPSSiC-2, probably due to the excess alumina in LPSSiC-2, which dissolves in strong alkaline environments.

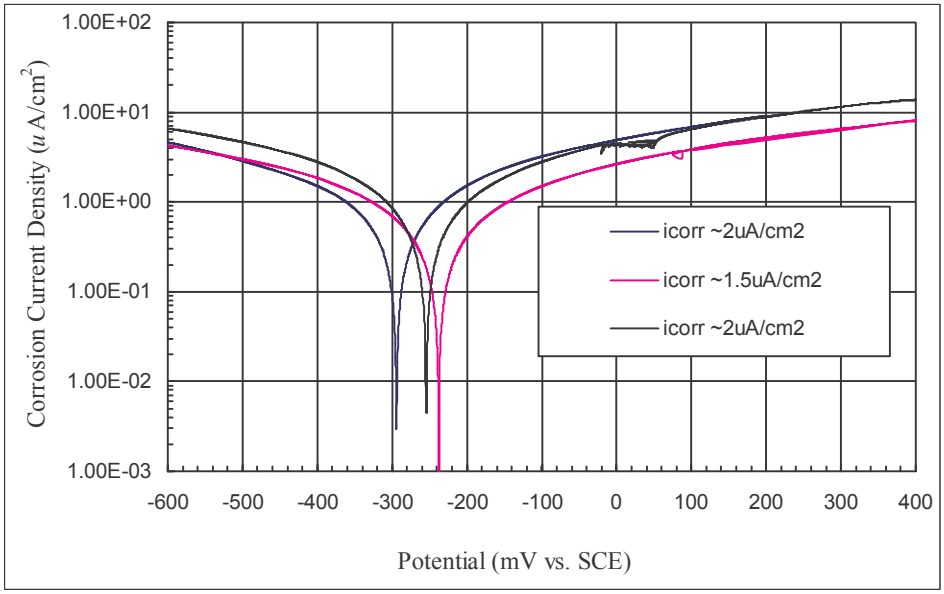


Figure 6.9 Potentiodynamic polarisation scans of LPSSiC-1 in 1 M NaOH. Corrosion potential shifts, but corrosion current densities are nearly the same. The average corrosion current density is ~1.8 $\mu A / cm^2$.

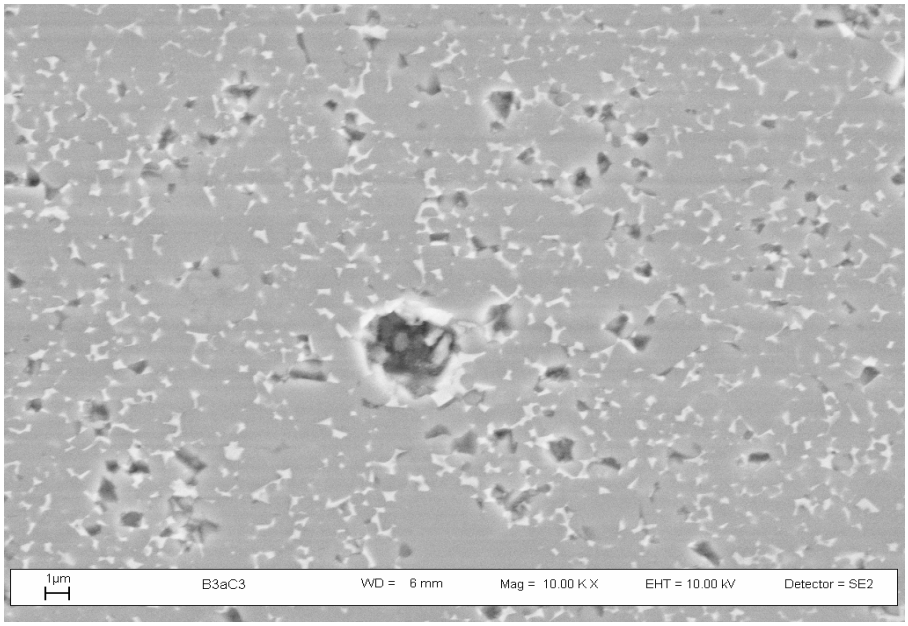


Figure 6.10 Secondary electron SEM micrograph of LPSSiC-1 after full potentiodynamic scan in 1 M NaOH. Corrosion at the secondary phase is less than in 1 M HCl.

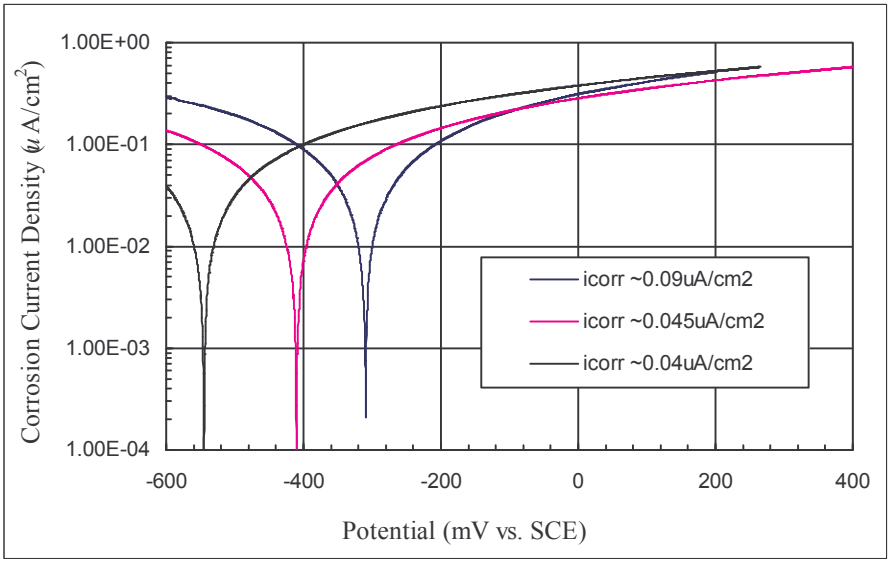


Figure 6.11 Potentiodynamic polarisation scans of LPSSiC-2 in 1 M NaOH. Corrosion potential shifts with each scan, however, corrosion current densities are similar. The average corrosion current density is ~0.06 $\mu A / cm^2$.

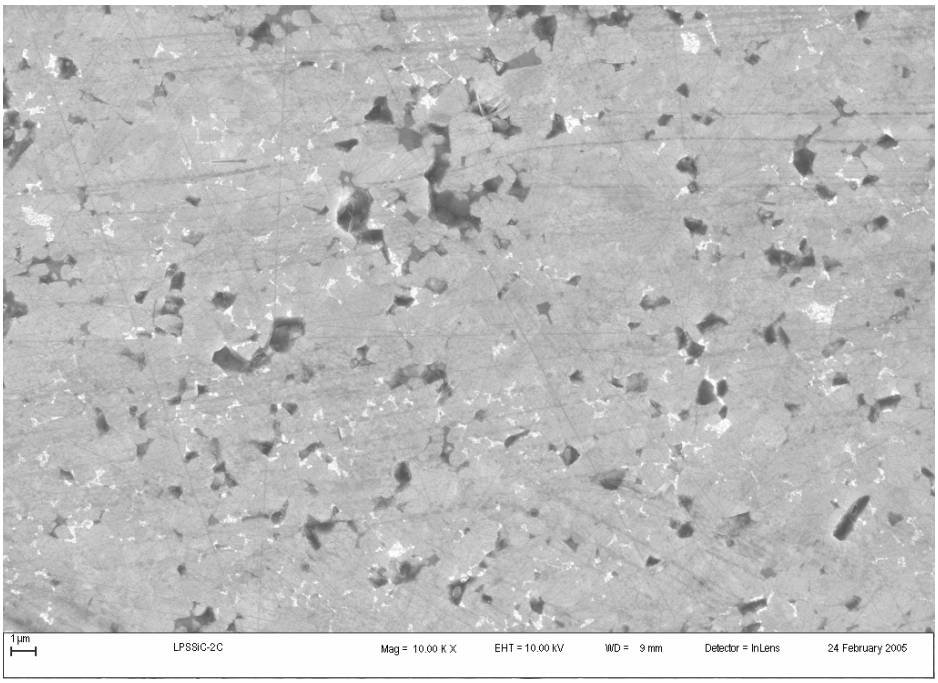


Figure 6.12 Secondary electron SEM micrograph of LPSSiC-2 after full potentiodynamic scan in 1 M NaOH. Corrosion at the secondary phase is less than for LPSSiC-1.

6.2.4 Corrosion behaviour in distilled water

The potentiodynamic polarisation scans and the microstructural appearance after scanning in distilled water are shown in figures 6.13 to 6.16. Corrosion potentials were not reproducible. The average corrosion current densities for LPSSiC-1 and LPSSiC-2 were ~0.2 $\mu A/cm^2$ and ~0.07 $\mu A/cm^2$, respectively. After scanning in distilled water, the surfaces were not severely damaged.

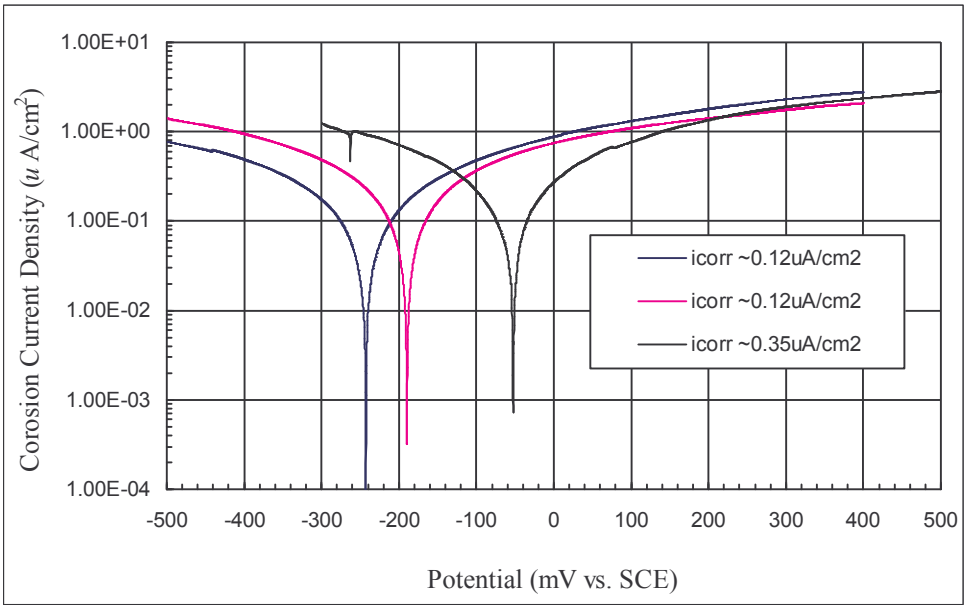


Figure 6.13 Potentiodynamic polarisation scans of LPSSiC-1 in distilled water. Corrosion potential shifts to more active values with subsequent scans on the same sample re-polished. However, the corrosion current densities are nearly the same. The average corrosion current density is ~0.2 $\mu A/cm^2$.

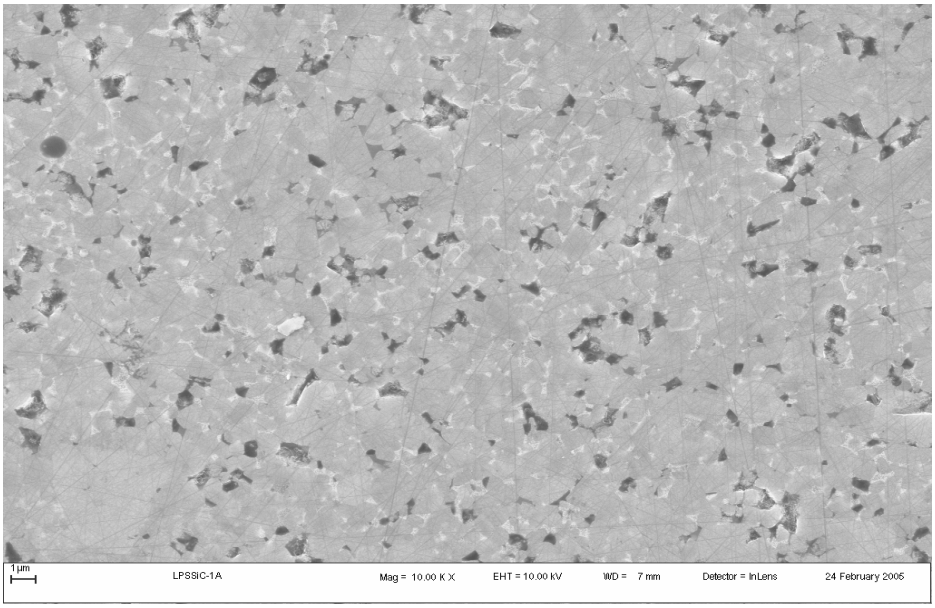


Figure 6.14 Secondary electron SEM micrograph of LPSSiC-1 after full potentiodynamic scan in distilled water.

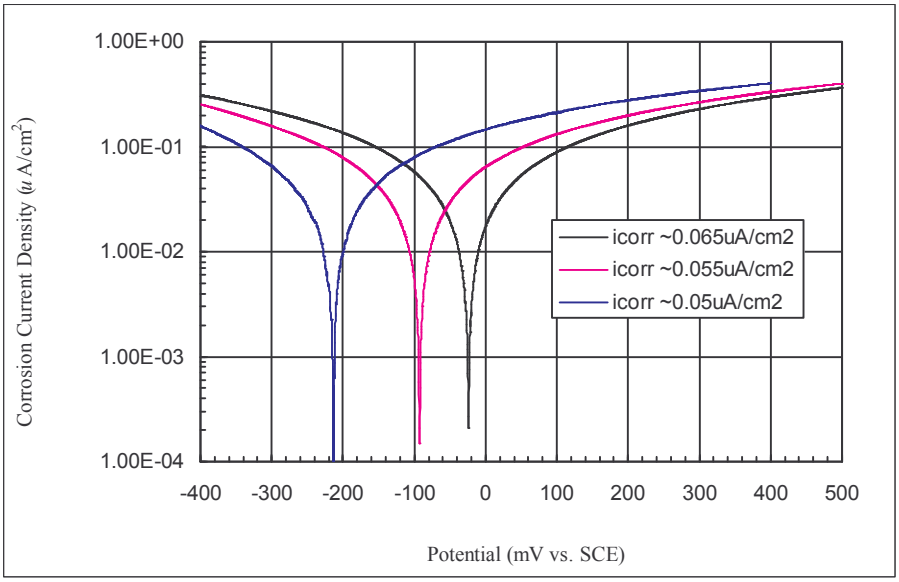


Figure 6.15 Potentiodynamic polarisation scans of LPSSiC-2 in distilled water. Corrosion potential shifts to more active values with subsequent scans on the same sample re-polished. However, the corrosion current densities are nearly the same. The average corrosion current density is ~0.07 $\mu A / cm^2$.

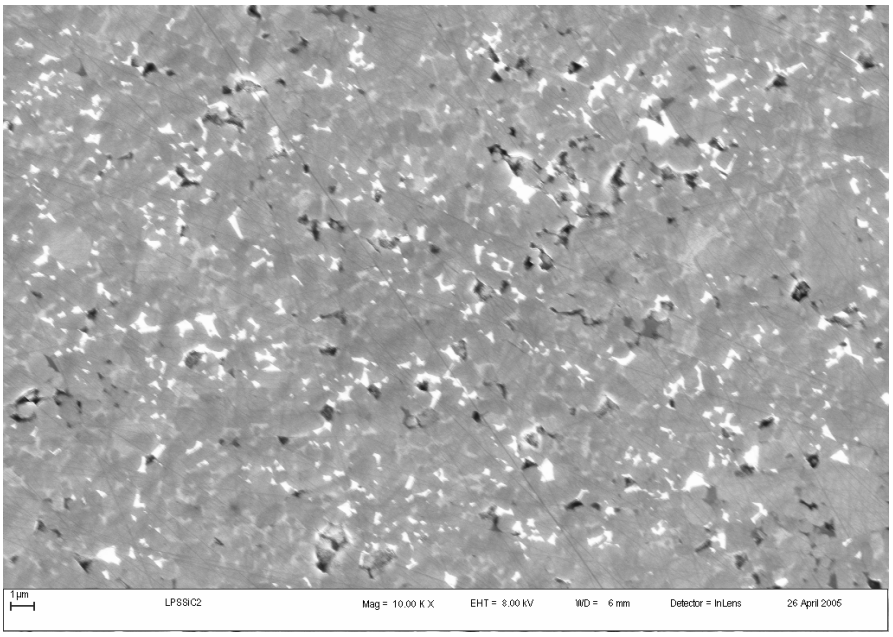


Figure 6.16 Secondary electron SEM micrograph of LPSSiC-2 after full potentiodynamic scan in distilled water.

In comparison, the average corrosion current densities for LPSSiC-1 were higher than LPSSiC-2 in all the test environments. The corrosion current densities in distilled water were much lower than in other corrosive media indicating the resistance of LPSSiC materials to corrosion in water, as was shown by Herrmann *et al*., (2003) by immersion. In figure 6.17, the graph comparing the average corrosion current densities for both materials in the different media is shown.

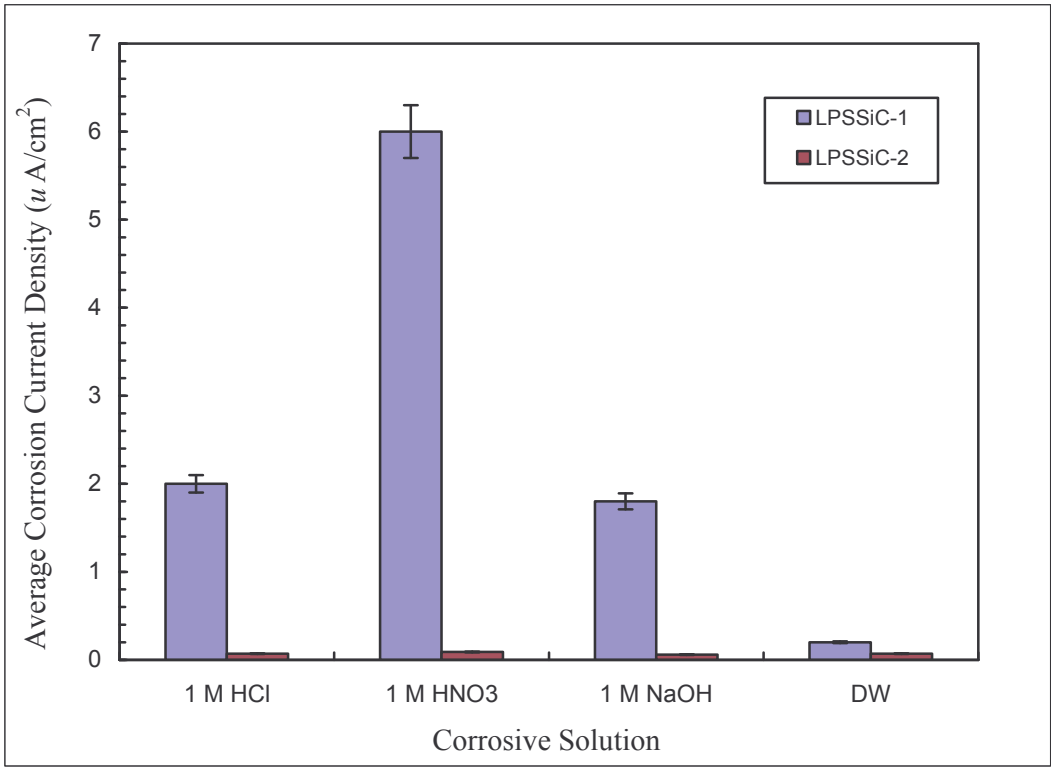


Figure 6.17 Comparison of average corrosion current densities of LPSSiC-1 and LPSSiC-2 samples in different corrosive media. The shifts in the E_{corr} were not accounted for in the calculation of the average i_{corr}.

6.3 Corrosion Mechanisms of LPSSiC Materials

The electrochemical reactions of the SiC grains in LPSSiC would be as in SSiC (discussed in the previous chapter). These reactions are:

Acidic environments

$$SiC(s) + 2H_2O(l) \rightarrow SiO_2(s) + C + 4H^+(aq) + 4e^- \qquad E^o = -1.07 \text{ V} \qquad [5.9]$$

$$SiC(s) + 3H_2O(l) \rightarrow SiO_2(s) + 6H^+(aq) + CO(g) + 6e^- \qquad E^o = -0.542 \text{ V} \qquad [5.11]$$

Alkaline environments

$$SiC(s) + 6OH^-(aq) \rightarrow SiO_3^{2-}(aq) + C + 3H_2O(l) + 4e^- \qquad E^o{}_B = -1.874 \text{ V} \qquad [5.13]$$

$$SiC(s) + 12OH^-(aq) \rightarrow SiO_3^{2-}(aq) + 5H_2O(l) + CO_3^{2-}(aq) + 8e^-$$

$$E^o{}_B = -0.076 \text{ V} \qquad [5.14]$$

$$SiC(s) + 8OH^-(aq) \rightarrow SiO_3^{2-}(aq) + 4H_2O(l) + CO(g) + 6e^- \qquad E^o{}_B = -0.8 \text{ V} \qquad [5.15]$$

In addition, with these liquid phase sintered materials, the secondary phase can undergo a severe dissolution in acid environments as:

$$Y_3Al_5O_{12} + 24H^+(aq) \leftrightarrow 3Y^{3+}(aq) + 5Al^{3+}(aq) + 12H_2O(l) \qquad [6.1]$$

In strong alkaline environments, Al and Y in solution could react to form $[Al(OH)_6]^{3-}$ or AlO_2^- ions and $Y(OH)_3$, respectively (Bard *et al*., 1985).

In the remaining sections of this chapter, two hypotheses were proposed with the aim of determining which of the reactions govern the corrosion behaviour of the materials in the various corrosive media (Section 6.2).

6.3.1 Effect of the Secondary Phase

Hypothesis I

If the secondary phase contribute to the current densities measured, immersing the sample in an electrolyte and holding at a more positive potential for a period of time and comparing the SEM micrograph after corrosion with another sample immersed in the same medium (without applying potential) would show significant changes of the two SEM micrographs with respect to the amount of secondary phase dissolved. This is because the application of current will increase the corrosion of all the phases dissolving electrochemically.

Two samples were immersed in 1 M HCl and held at +300 mV (vs. SCE) for 10 and 30 minutes, respectively. Two other LPSSiC-1 samples were immersed in 1 M HCl for 10 and 30 minutes, respectively, without applying potential. Scanning electron microscopy was used to determine the effect of these treatments. The SEM micrographs are shown in figures 6.18 to 6.21.

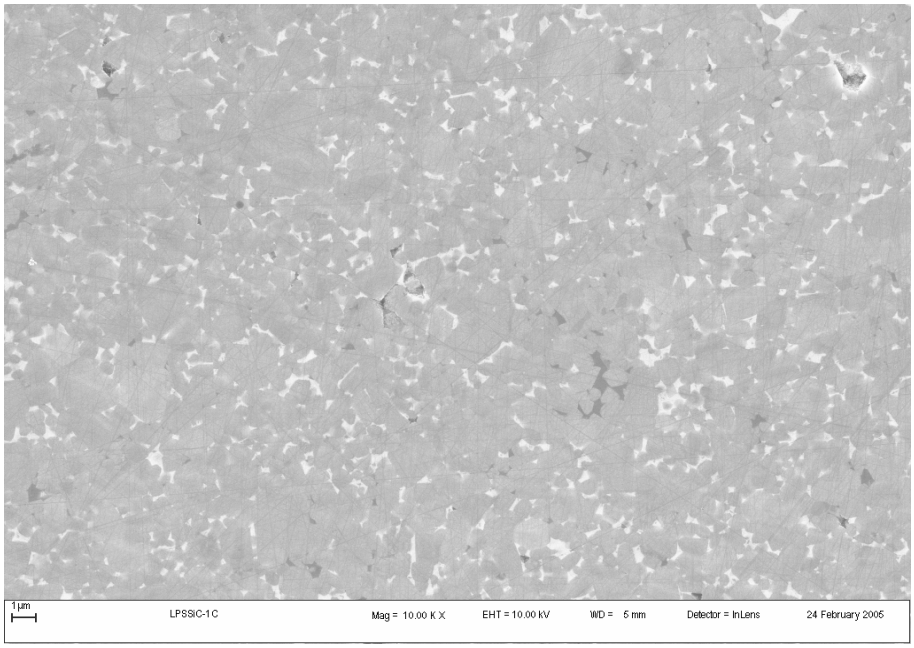


Figure 6.18 Secondary electron SEM micrograph of LPSSiC-1 after holding at +300 mV (vs. SCE) in 1 M HCl for 10 minutes.

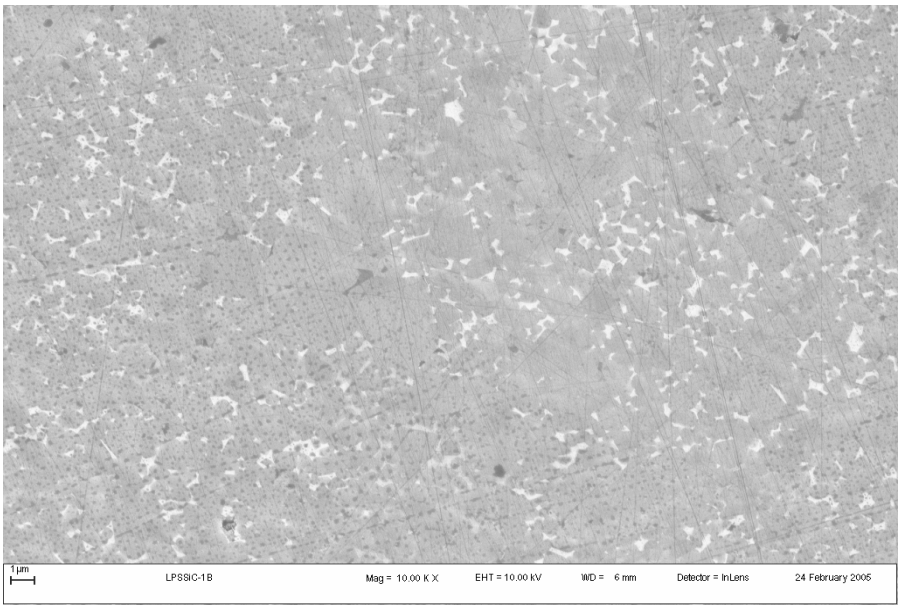


Figure 6.19 Secondary electron SEM micrograph of LPSSiC-1 after immersion in 1 M HCl for 10 minutes showing about the same corrosion damage at the secondary phase as with 10 minutes hold at +300 mV (vs. SCE).

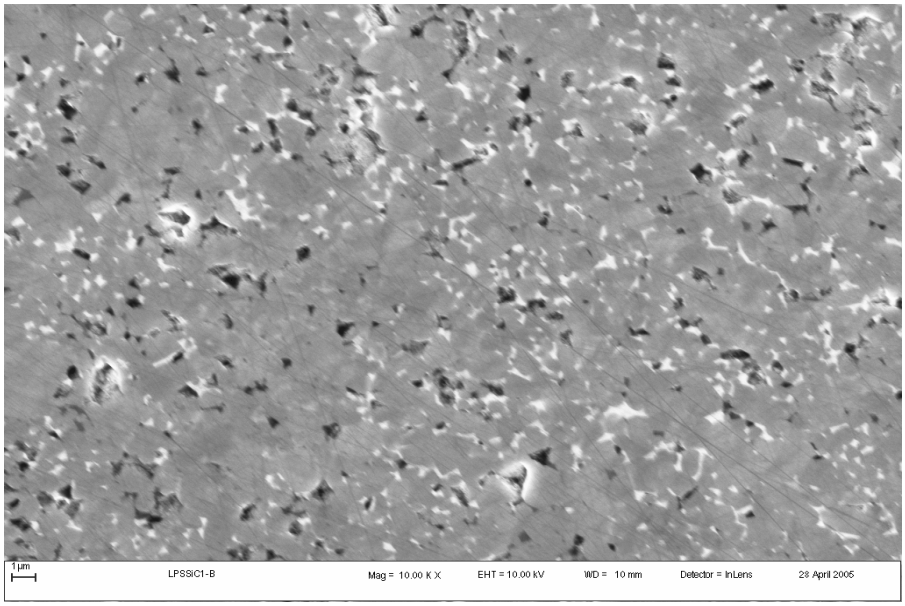


Figure 6.20 Secondary electron SEM micrograph of LPSSiC-1 after holding at +300 mV (vs. SCE) in 1 M HCl for 30 minutes.

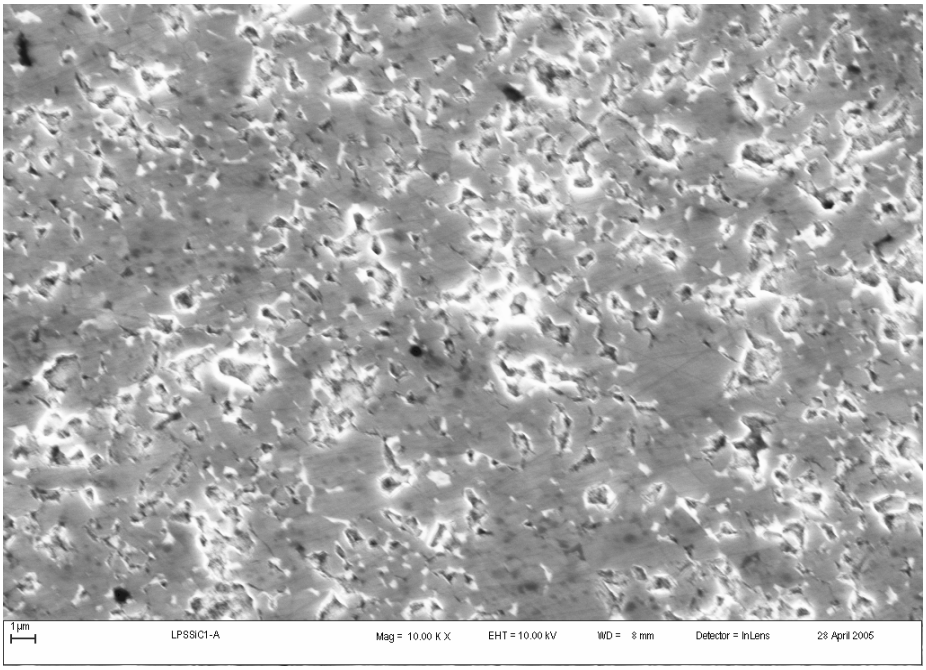


Figure 6.21 Secondary electron SEM micrograph of LPSSiC-1 after immersion in 1 M HCl for 30 minutes showing about the same corrosion damage at the secondary phase as with 30 minutes hold at +300 mV (vs. SCE).

It appears that there were no significant differences after 10 minutes immersion and immersion plus hold at +300 mV in 1 M HCl, nor did the 30 minutes immersion and immersion plus hold at +300 mV in 1 M HCl samples different. However, there was more damage to the secondary phase after longer exposure to HCl, with immersion and with immersion plus hold at +300 mV.

Since there were no significant differences in the surface attack on the immersion and immersion plus hold samples, it suggests that the secondary phase is not contributing to the current densities measured. Hypothesis I is therefore, not likely. The effect of the secondary phase was further investigated through Hypothesis II.

Hypothesis II

If the secondary phase contributes to the current densities measured, then from Le Chattelier's principle, dissolving yttrium chloride (YCl_3) in HCl (electrolyte) would reduce the dissolution of the secondary phase, thereby reducing or eliminating its effect on the measured current densities and subsequently leading to lower measured corrosion current densities.

Both LPSSiC-1 and LPSSiC-2 samples were prepared for potentiodynamic polarisation scans as described in Chapter 3 (section 3.4). 10g of YCl_3 was dissolved in 0.2 litres of 1 M HCl to increase the concentration of the yttrium ions. The scan results are shown in figures 6.22 and 6.24. The SEM micrograph of LPSSiC-1 after scanning is also shown in figure 6.23. The corrosion current densities for both materials were approximately the same but all potentials shifted to more noble values. As can be seen in figure 6.23, the secondary phase appears to be attacked to a lesser extent than in the HCl without YCl_3 (compare to figure 6.2)

This seems to indicate that the dissolution of the secondary phase does not contribute to the current densities measured and therefore Hypothesis II is not probable. The shifts recorded for the open circuit potential may indicate a lower driving force for corrosion in the YCl_3 solution, however, without further investigations it is difficult

to form any qualitative conclusion. On the other hand, the marked shifts for the E_{corr} between the different environments, at the same potential, which could be connected with the scattering of the data measured through liberation of electrons.

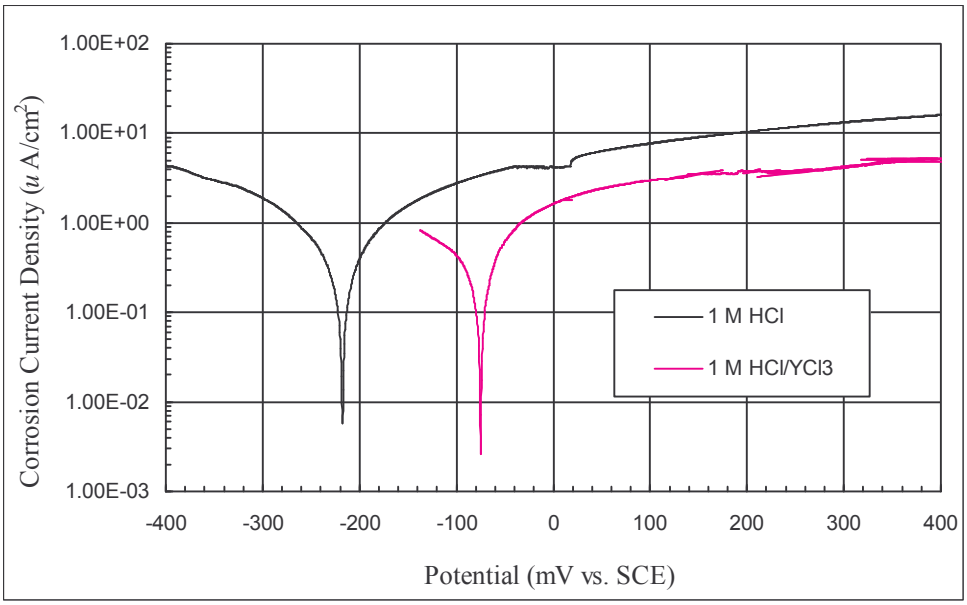


Figure 6.22 Potentiodynamic polarisation scans of LPSSiC-1 in 1 M HCl and 1 M HCl/YCl_3. Corrosion current densities are about the same.

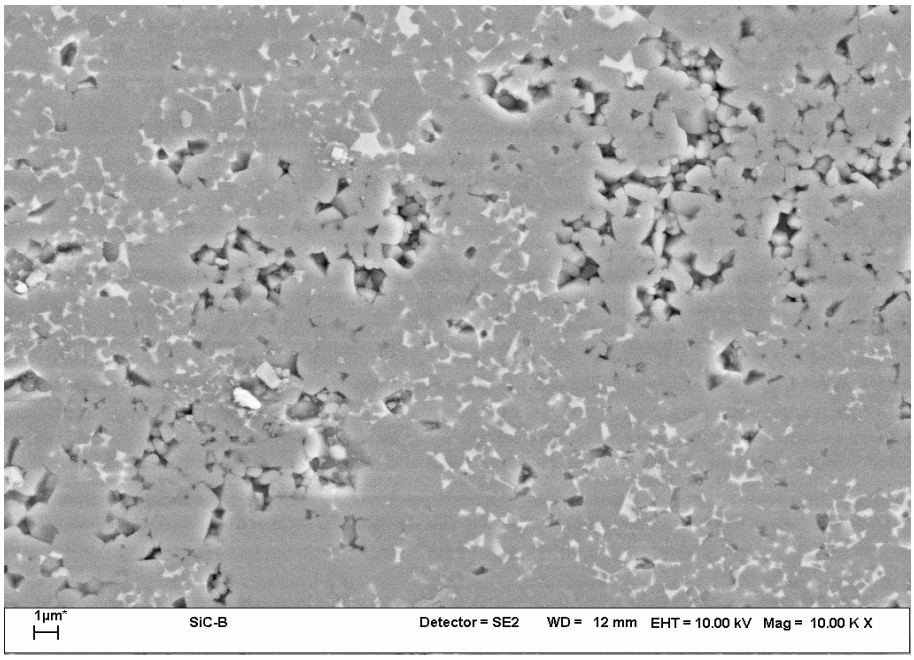


Figure 6.23 Secondary electron SEM micrograph of LPSSiC-1 after full potentiodynamic scan in 1 M HCl/YCl_3. The secondary phase is attacked to a lesser extent than after exposure to 1 M HCl.

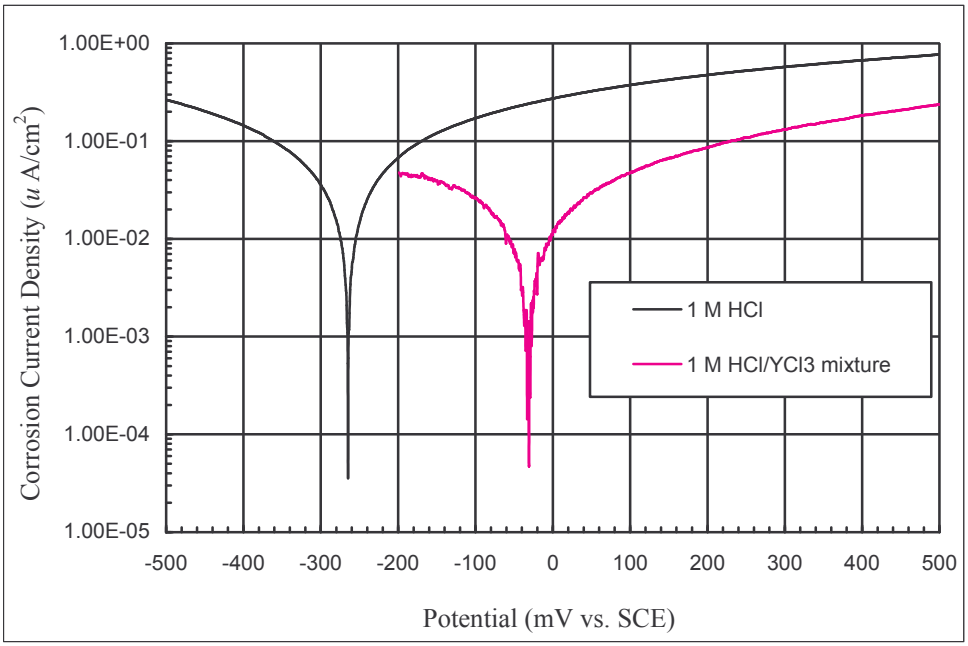


Figure 6.24 Potentiodynamic polarisation scans of LPSSiC-2 in 1 M HCl and 1 M HCl/YCl_3 mixture. Corrosion current densities are about the same.

From the disproval of hypothesis I and II, it appears that the secondary phase most likely dissolves out according to equation 6.1 (acid-base type of reactions), rather than through electrochemical corrosion involving redox reactions. Based on the above results, the corrosion current densities of LPSSiC materials in Section 6.2 were recalculated using the area of the SiC phase alone; however, there were no significant changes since the volume fraction of the SiC phase was more than 90 %. It is clear however, that though the secondary phase is not contributing to the current densities measured, it does affect the reproducibility of the polarisation scans, and the corrosion current densities measured. For example, the current density at high potentials, for instance at +200 mV in 1 M HCl, decreases by an order of magnitude ($100\,\mu A/cm^2$ for SSiC to about 10 $\mu A/cm^2$ for LPSSiC materials) indicating the effect of the secondary phase on the current densities. These results are contrary to what Herrmann *et al*. (2003) found by immersion techniques. Results showed that the weight loss of the SSiC was less than the weight loss of the LPSSiC. The reason for the contradiction could be the preferential dissolution of the secondary phase, as was observed with ICP-OES (see section 6.4), which increased the weight loss of LPSSiC. Therefore it can be concluded that the corrosion currents measured for LPSSiC was due to the dissolution of SiC grains alone and not the secondary phase.

6.4 Relative Dissolution of the Secondary Phase and the Silicon Carbide Phase

In order to establish the relative dissolution of each phase during corrosion, an inductively coupled plasma optical emission spectrometer (ICP-OES) was used to determine the concentrations of Al, Si, and Y cations in the electrolyte before and after corrosion for LPSSiC materials. Figures 6.29 and 6.30 compare the dissolved ion concentrations of Si, Al, and Y in 1 M HCl and 1 M NaOH for both LPSSiC materials after full potentiodynamic scans.

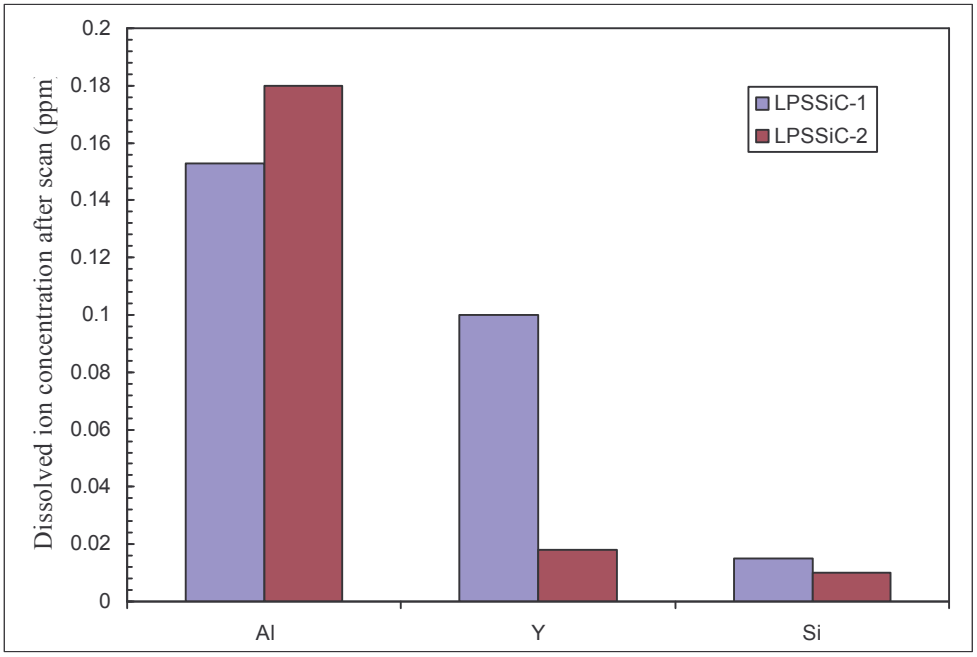


Figure 6.29 Comparison of dissolved ion concentration of Si, Al, and Y after full potentiodynamic scan on LPSSiC-1 and LPSSiC-2 in 1 M HCl.

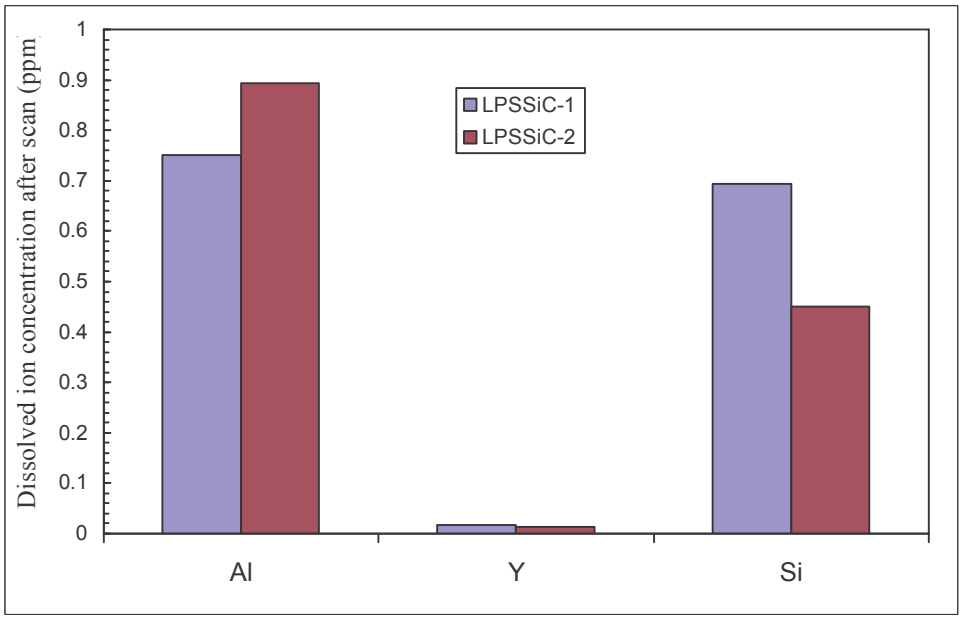


Figure 6.30 Comparison of dissolved ion concentration of Si, Al, and Y after full potentiodynamic scan on LPSSiC-1 and LPSSIC-2 in 1 M NaOH.

The aluminium ion concentration in both HCl and NaOH was higher for LPSSiC-2 than LPSSiC-1, because of the excess alumina in LPSSiC-2. The silicon ion concentrations were higher for LPSSiC-1 than LPSSiC-2, which was also evident in the polarisation scans as higher corrosion densities were recorded (see Section 6.2). The yttrium ion concentration for both materials were very low in NaOH, compared to the Al and Si concentrations. This is probably due to the formation of $Y(OH)_3$ which precipitates on the surface, inhibiting further dissolution of yttrium (Bard *et al*., 1985). Aluminium on the other hand dissolves in strong alkaline environments forming $[Al(OH_6)]^{3-}$ or AlO_2^- ions, and this suggests that the dissolution of the secondary phase is not homogenous: aluminium undergoes intensive dissolution, while yttrium is relatively stable in this alkaline environment, leaving the secondary phase only slightly affected by corrosion. The silicon ion concentration in NaOH was higher than in HCl, and confirms the proposal by Lay (1983) that SiC is resistant to acidic environments but less resistant to alkaline environments.

The relative dissolution of the secondary and the SiC phases were further investigated by XRD analysis on LPSSiC-1 before and after corrosion in 1 M HCl. The intensities of the different compound peaks before and after corrosion are compared in figure 6.31.

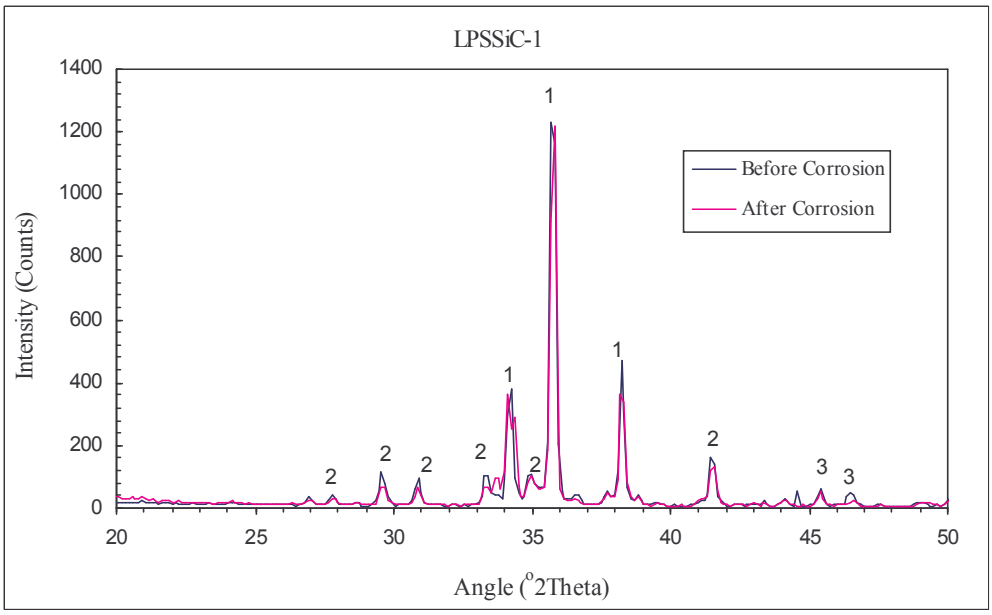


Figure 6.31 XRD pattern comparison of the LPSSiC-1 before and after corrosion in 1 M HCl. 1–SiC; 2–yttrium aluminate (YAG); 3–aluminium yttrium oxide ($Al_2Y_4O_9$)

The XRD pattern detected showed an increase of the ratio *R* (equations 6.2 to 6.4) between heights of SiC (*h,k,l*), YAG (*h,k,l*) and $Al_2Y_4O_9$ (*h,k,l*) peaks before and after corrosion, respectively (see table 6.1):

$$R = h_{SiC(h,k,l)} / h_{YAG(h,k,l)} \quad [6.2]$$

$$R = h_{SiC(h,k,l)} / h_{Al2Y4O9(h,k,l)} \quad [6.3]$$

$$R = h_{YAG(h,k,l)\,/\,Al2Y4O9(h,k,l)} \quad [6.4]$$

where *h,k,l* are specific crystallographic planes on the XRD pattern.

These results indicate that YAG and $Al_2Y_4O_9$ dissolved preferentially in the corroded sample, and confirm the observations in the SEM micrographs (Section 6.2). The degree of dissolution of $Al_2Y_4O_9$ is higher than that of the YAG phase.

Table 6.1 Ratio (R) at different peaks before and after corrosion of LPSSiC-1 in 1 M HCl

	Before Corrosion	**After Corrosion**
$h_{SiC(1,1,6)\,/\,YAG(6,4,0)}$	8.08	50.33
$h_{SiC(1,1,6)\,/\,Al2Y4O9(1,0,1)}$	10.86	13.50
$h_{YAG(6,4,0)\,/\,Al2Y4O9(1,0,1)}$	0.26	1.34
$h_{SiC(1,0,3)\,/\,YAG(5,3,2)}$	22.38	46.97
$h_{SiC(1,0,3)\,/\,Al2Y4O9(2,1,2)}$	4.20	16.25
$h_{YAG(5,3,2)\,/\,Al2Y4O9(2,1,2)}$	0.09	0.71
$h_{SiC(1,1,0)\,/\,YAG(4,2,2)}$	1.23	1.28
$h_{SiC(1,1,0)\,/\,Al2Y4O9(1,1,3)}$	17.39	80.81
$h_{YAG(4,2,2)\,/\,Al2Y4O9(1,1,3)}$	13.60	65.73
$h_{SiC(1,0,4)\,/\,YAG(8,4,2)}$	0.33	0.48
$h_{SiC(1,0,4)\,/\,Al2Y4O9(0,4,0)}$	2.97	5.17
$h_{YAG(8,4,2)\,/\,Al2Y4O9(0,4,0)}$	8.35	11.81

The ICP-OES results did not show which grains were dissolving out; but only gave the degree of dissolution of each ion. The XRD results assisted in elucidating the different phases dissolved into the corrosive solutions, and as a result, understanding the dissolution process of the secondary phase.

6.5 Conclusion

The electrochemical reactions of the SiC grains in LPSSiC were assumed to be as those for SSiC (discussed in the previous chapter) but it appears that the secondary phase is not contributing to the current densities measured. The dissolution of the secondary phase is through acid-base type of reactions, rather than through electrochemical corrosion involving redox reactions. Nevertheless, systematic differences between the current densities of the LPSSiC-1 and LPSSiC-2 were found. This could be due to the secondary phase having an indirect influence by changing the surface layer formed or by changing the diffusion of the silicon atoms in the

material. Table 6.1 summarises the polarisation results obtained for LPSSiC-1 and LPSSiC-2 compared to those of SSiC.

Table 6.2 Summary of the polarisation results of LPSSiC-1 and LPSSiC-2, compared to SSiC

Material	Condition (s)	Average Corrosion Potential (mV vs. SCE)	Corrosion Potential (mV vs. SHE)	Current Density, i_{corr} ($\mu A/cm^2$)
SSiC	1 M HCl	-125	+116	46
	1 M NaOH	+53	+294	33
LPSSiC-1	1 M HCl	-215	+26	2
	1 M NaOH	-846	-605	0.9
LPSSiC-2	1 M HCl	-302	-61	0.07
	1 M NaOH	-402	-179	0.06

From the ICP-OES results, it seems that the corrosion resistance of LPSSiC materials would depend on the composition and amount of the secondary phase present in the matrix. For instance, the LPSSiC-2 material with excess alumina recorded higher aluminium ion concentration in corrosive solution than LPSSiC-1 (with no excess alumina). In strong alkaline environments, Al and Y seem to react forming $[Al(OH)_6]^{3-}$ or AlO_2^- ions, and $Y(OH)_3$, respectively. The $Y(OH)_3$ formed inhibited the dissolution of yttria (Figure 6.30). Even though the secondary phase is not contributing to the current densities measured, it does however, affect the reproducibility of the polarisation scans as well as the values of corrosion current densities.

Based on the three hypotheses proposed in this chapter, it therefore seems likely that the following corrosion reactions of LPSSiC materials are feasible:

Acidic environments:

$$SiC(s) + 2H_2O(l) \rightarrow SiO_2(s) + C + 4H^+(aq) + 4e^- \qquad E^o = -1.07\ \text{V} \qquad [5.9]$$

$$SiC(s) + 3H_2O(l) \rightarrow SiO_2(s) + 6H^+(aq) + CO(g) + 6e^- \qquad E^o = -0.542\,\text{V} \qquad [5.11]$$

Alkaline environments:

$$SiC(s) + 6OH^-(aq) \rightarrow SiO_3^{2-}(aq) + C + 3H_2O(l) + 4e^- \qquad E^o{}_B = -1.874\ \text{V} \qquad [5.13]$$

$$SiC(s) + 12OH^-(aq) \rightarrow SiO_3^{2-}(aq) + 5H_2O(l) + CO_3^{2-}(aq) + 8e^-$$

$$E^o{}_B = -0.076\,\text{V} \qquad [5.14]$$

$$SiC(s) + 8OH^-(aq) \rightarrow SiO_3^{2-}(aq) + 4H_2O(l) + CO(g) + 6e^- \qquad E^o{}_B = -0.8\,\text{V} \qquad [5.15]$$

The secondary phases are dissolving out according to

$$Y_3Al_5O_{12} + 24H^+(aq) \leftrightarrow 3Y^{3+}(aq) + 5Al^{3+}(aq) + 12H_2O \qquad [6.1]$$

Reaction [6.1] is an acid-base type reaction.

The above findings show that the corrosion resistance of LPSSiC materials depends on the composition of the secondary phase. The results of Herrmann *et al*. (2003) showed that the weight loss of the SSiC was less than the weight loss of the LPSSiC. The reason for this behaviour could be the preferential dissolution of the secondary phase, as was observed with ICP-OES, which increased the weight loss of LPSSiC. The corrosion currents measured for LPSSiC was due to the dissolution of SiC grains alone and does not include the secondary phase.

CHAPTER 7

SUMMARY

In conjunction with microstructural examinations, the corrosion of SSiC and LPSSiC ceramic materials have successfully been investigated using electrochemical techniques, and the likely corrosion reactions under certain conditions were established. It therefore seems highly possible to use potentiodynamic techniques to investigate the corrosion behaviour of conducting and semi-conducting ceramics.

The investigation showed that the corrosion behaviour of SSiC ceramics is due to the dissolution of both Si and C present in the SiC compound, and that the residual carbon existing in the material was not contributing to the corrosion behaviour of SSiC materials. The possibility of the electrochemical dissolution of carbon forming CO_2 was ruled out. It seems SSiC was resistant to the HCl and HNO_3 as a result of a protective oxide film (SiO_2) forming on the surface. Soluble silicates or hydrated silica were formed in NaOH as a result of high pH. The rate of formation of silicate ions is proportional to the corrosion rate of SSiC materials in alkaline environments and would therefore play a major role in the kinetics of the process. Thus SSiC materials went through a more severe dissolution in alkaline environments than in acidic environments.

The electrochemical corrosion of LPSSiC was due to the dissolution of SiC, and not the secondary phase. The chemical attack on the secondary phases was by acid-base type of reactions rather than electrochemical corrosion involving redox reactions. The secondary phase (YAG and $Al_2Y_4O_9$) went through a more severe dissolution in acidic environments than in alkaline environments, while the opposite was true for the SiC phase. The degree of dissolution of the aluminium and yttrium was higher than the silicon, but in NaOH, silicon dissolved more than the yttrium and aluminium. The open circuit potential of the LPSSiC materials was much less reproducible in comparison to the SSiC materials. The reason for this behaviour is not completely clear and needs further investigation. The open circuit potentials of LPSSiC

materials were lower than the SSiC materials under the same corrosive conditions, and corrosion current densities of an order of magnitude lower than those of the SSiC were recorded. Thus, even though the secondary phase was not contributing to the current densities being measured, it affects the corrosion rates and the reproducibility of the polarisation scans. The stability of LPSSiC materials in corrosive environments would therefore depend on the nature and composition of the secondary phase. The mechanism by which the secondary phase influences the electrochemical corrosion has to be determined in further investigations.

REFERENCES

Antelman, M.S. (1982), "*The Encyclopedia of Chemical Electrode Potentials"*, New York, Plenum, pp. 101, 183

ASTM G5-94, Annual Books of ASTM Standards (2000), Making Potentiostatic and Potentiodynamic Anodic Polarisation Measurements, Vol. 03.02, pp.57-67

ASTM G3-89, Annual Books of ASTM Standards (2000), Conventions Applicable to Electrochemical Measurements in Corrosion Testing, Vol. 03.02, pp.38-42

Bard, A. J. Parsons, R. and Jordan, J. (1985), *Standard Potentials in Aqueous Solutions*, Monographs in Electroanalytical Chemistry and Electrochemistry, (ed. A.J. Bard), New York, Marcel Dekker, pp. 189 – 206, 566 – 580, 587 – 629

Bellosi, A. Monteverde, F. Mingazzini, C. and Giorgi, M. (2001), Corrosion of Silicon Nitride in Sulphuric Acid Aqueous Solution, *Corrosion Science*, **43**, (10), pp. 1851-1863

Cook, G. S. Little, J.A. and King, J.E. (1994), Corrosion of Silicon Carbide Ceramics using Conventional and Electrochemical Methods, *British Corrosion Journal*, **29**, (3), pp. 183-185

Divakar, R. Seshadri, S. G. and Srinivasan, M. (1989), Electrochemical Techniques for Corrosion Rate Determination in Ceramics, *Journal of American Ceramic Society*, **72,** (5), pp. 780-784

Fett, D. M. T. (1999), *Ceramics: Mechanical Properties, Failure Behaviour, Materials Selection*, Berlin; New York, Springer, pp. 1 – 13

German, R. M. (1996), *Sintering theory and practice*, the Pennsylvania State University, University park, Pennsylvania

Herrmann, M. Schilm, J. Michael, G. and Adler, J. (2003), *Corrosion Behaviour of Different Technical Ceramics in Acids, Basic Solutions and under Hydrothermal Conditions*, in cfi/Ber. DKG, **80**, (4), pp.E27-E34

Izhevskyi, V. A. Genova, L. A. Bressiani, A. H. A. and Bressiani, J. C. (2000), Liquid Phase Sintered SiC. Processing and Transformation, *Materials Research*, **3**, (4), pp. 131–138

Jones, D.A. (1996), *Principles and Prevention of Corrosion*, ed. 2, Prentice-Hall, Inc.

Lay, L.A. (1983), *Corrosion Resistance of Technical Ceramics*, London, HMSO, pp. 23 – 62

Lee, C.-S. Kim, Y.-W. Cho, D.-H. Lee, H.-B. and Lim, H.-Jin (1998), Microstructure and Mechanical Properties of self-Reinforced α - SiC, *Ceramics International,* **24**, (7), pp. 489-495

Liu, D.-M. (1997), Oxidation of Polycrystalline α - Silicon Carbide Ceramic, *Ceramics International,* **23**, (5), pp. 425–436

Magnani, G. Minoccari, G. L. and Pilotti, L. (2000), Flexual Strength and Toughness of Liquid Phase Sintered Silicon Carbide, *Ceramics International,* **26**, (5), pp.495-500

McCauley, R.A. (1995), Corrosion of Ceramics, *Corrosion Science*, **37**, (12), pp. 2099 – 2101

Morrell, R. (1985), *Handbook of Properties of Technical and Engineering Ceramics*, Part 1, An Introduction for the Engineering and Designer, HMSO, London

Nickel, K. G. (1997), Corrosion of Non-Oxide Ceramics, *Ceramics International,* **23**, (2), pp. 127-133

Nickel, K. G. and Seipel, B. (2003), Corrosion of Silicon Nitride in Aqueous Acid Solutions: Penetration Monitoring, *Journal of European Ceramic Society*, **23**, (4), pp. 595-602

Oldham, H.B. and Myland J.C. (1994), Fundamentals of Electrochemical Science, Academic Press, Inc., San Diego, New York, Boston

Pelissier, K. Chartier, T. and Laurent, J. M. (1998), Silicon Carbide Heating Elements, *Ceramics International,* **24**, (5), pp.371-377

Pourbaix, M. Muylder, J. V. Besson, J. and Kunz, W. (1958), *Atlas of Electrochemical Equilibria in Aqueous Solution*, pp. 449 - 463, Houston. TX. NACE

Rahaman, M. N. (2003), *Ceramic Processing and Sintering*, ed. 2, Marcel Dekker, Inc., New York. Basel

Schwetz, K. A. (2000), *Silicon Carbide Based Hard Materials*, in Handbook of Ceramic Hard Materials, edited by Ralf Riedel, Vol.2, pp. 683-748

Scientific Group Thermodata Europe (2001), *Pure Substance Database*

Sharkawy, S. W. and El-Aslabi, A. M. (1998), Corrosion of Silicon Nitride Ceramics in Aqueous HCl and HF Solutions, *Corrosion Science*, **40**, (7), pp. 1119-1129

Steen, M. and Ranzani, L. (2000), Potential of SiC as a Heating Exchanger Material in Combined Cycle Plant, *Ceramics International,* **26**, (8), pp. 849-854

Stobierski, L. and Gubernat, A. (2003a), Sintering of Silicon Carbide I. Effect of Carbon, *Ceramics International,* **29**, (3), pp.287-292

Stobierski, L. and Gubernat, A. (2003b), Sintering of Silicon Carbide II. Effect of Boron, *Ceramics International,* **29**, (4), pp.355-361

APPENDIX A

Thermodynamic calculations of standard potentials of the cell reactions

The standard free energy change, ΔG^o, may be associated with standard electrode potential, E^o, at equilibrium, by the fundamental relationship

$$\Delta G^o = -nFE^0 \qquad [1]$$

where n is the number of electrons (or equivalents) exchanged in the reaction, and F is Faraday's constant, 96485 coulombs per equivalent. The negative (-) in equation 1 is included to conform to the convention hat a positive potential, E, results in a negative free energy change, ΔG, for a spontaneous reaction.

For the reactions in acid environments:

$$C(s) + 2H_2O(l) \rightarrow CO_2(g) + 4H^+(aq) + 4e^- \qquad E^o = +0.206\,\text{V} \qquad [2]$$

$$\Delta G^o = -4 \times 96485 \times (+0.206)$$

$$\Delta G^o = -79503.64 \text{ J/mol}$$

$$C(s) + H_2O(l) \rightarrow CO(g) + 2H^+(aq) + 2e^- \qquad E^o = +0.517 \text{ V} \qquad [3]$$

$$\Delta G^o = -2 \times 96485 \times (+0.517)$$

$$\Delta G^o = -99765.49 \text{ J/mol}$$

$$Si(s) + 2H_2O(l) \rightarrow SiO_2(s) + 4H^+(aq) + 4e^- \qquad E^o = -0.888\,\text{V} \qquad [4]$$

$$\Delta G^o = -4 \times 96485 \times (-0.888)$$

$$\Delta G^o = +342714.72 \text{ J/mol}$$

For the reactions in basic environments:

$C(s) + 3H_2O(l) \rightarrow CO_3^{2-}(aq) + 6H^+(aq) + 4e^-$ $\quad E^o{}_B = +0.48$ V [5]

$\Delta G^o{}_B = -4 \times 96485 \times (+0.48)$

$\Delta G^o{}_B = -185251.2$ J/mol

$6H^+(aq) + 6OH^-(aq) \rightarrow 6H_2O(l)$ $\quad \Delta G^o = -6(79922.1)$ J/mol [6]

For reaction 5.6

$C(s) + 3H_2O(l) \rightarrow CO_3^{2-}(aq) + 6H^+(aq) + 4e^-$ $\quad \Delta G^o{}_B = -185251.2$ J/mol [5]

$6H^+(aq) + 6OH^-(aq) \rightarrow 6H_2O(l)$ $\quad \Delta G^o = -479532.7$ J/mol [6]

$C(s) + 6OH^-(aq) \rightarrow CO_3^{2-}(aq) + 3H_2O(l) + 4e^-$ $\quad \Delta G^o_{5+6} = -664783.9$ J/mol [7]

$E^o = -\Delta G^o_{5+6} / nF = -(-664783.9)/(4 \times 96485) = +1.72$ V

$C(s) + H_2O(l) \rightarrow CO(g) + 2H^+(aq) + 2e^-$ $\quad \Delta G^o = -99765.49$ J/mol [3]

$2H^+(aq) + 2OH^-(aq) \rightarrow 2H_2O(l)$ $\quad \Delta G^o = -159844.2$ J/mol [6]

$C(s) + 2OH^-(aq) \rightarrow CO(g) + H_2O(l) + 2e^-$ $\quad \Delta G^o_{3+6} = -259609.69$ J/mol [8]

$E^o = -\Delta G^o_{3+6} / nF = -(-259609.69)/(2 \times 96485) = +1.345$ V

$Si(s) + 6OH^-(aq) \rightarrow SiO_3^{2-}(aq) + 3H_2O + 4e^-$ $\quad E^o{}_B = -1.69$ [9]

$\Delta G^o{}_B = -4 \times 96485 \times (-1.69)$

$\Delta G^o{}_B = +652238.6$ J/mol

Gibbs free energy change for the formation of SiC (SGTE, 2001)

$$SiC(s) \rightarrow Si(s) + C(s) \qquad \Delta G^o = +70850 \text{ J/mol} \qquad [10]$$

From the above reactions, the standard electrode potentials for the cell reactions were calculated as follows:

For reaction 5.9

$$Si(s) + 2H_2O(l) \rightarrow SiO_2(s) + 4H^+(aq) + 4e^- \qquad \Delta G^o = +342714.72 \text{ J/mol} \qquad [4]$$

$$SiC(s) \rightarrow Si(s) + C(s) \qquad \Delta G^o = +70850 \text{ J/mol} \qquad [10]$$

$$SiC(s) + 2H_2O(l) \rightarrow SiO_2(s) + C + 4H^+ + 4e^- \qquad \Delta G^o_{4+10} = +413564.72 \text{ J/mol}$$

$$E^o = -\Delta G^o_{4+10} / nF = -(+413564.72)/(4 \times 96485) = -1.07 \text{ V}$$

For reaction 5.10

$$Si(s) + 2H_2O(l) \rightarrow SiO_2(s) + 4H^+(aq) + 4e^- \qquad \Delta G^o = +342714.72 \text{ J/mol} \qquad [4]$$

$$SiC(s) \rightarrow Si(s) + C(s) \qquad \Delta G^o = +70850 \text{ J/mol} \qquad [10]$$

$$C(s) + 2H_2O(l) \rightarrow CO_2(g) + 4H^+(aq) + 4e^- \qquad \Delta G^o = -79503.64 \text{ J/mol} \qquad [2]$$

$$SiC(s) + 4H_2O(l) \rightarrow SiO_2(s) + CO_2(g) + 8H^+(aq) + 8e^- \qquad \Delta G^o_{2+4+10} = +334061.08 \text{ J /mol}$$

$$E^o = -\Delta G^o_{2+4+10} / nF = -(+334061.08)/(8 \times 96485) = -0.433 \text{ V}$$

For reaction 5.11

$Si(s) + 2H_2O(l) \rightarrow SiO_2(s) + 4H^+(aq) + 4e^-$ $\Delta G^o = +342714.72$ J/mol [4]

$SiC(s) \rightarrow Si(s) + C(s)$ $\Delta G^o = +70850$ J/mol [10]

$C(s) + H_2O(l) \rightarrow CO(g) + 2H^+(aq) + 2e^-$ $\Delta G^o = -99765.49$ J/mol [3]

$SiC(s) + 3H_2O(l) \rightarrow SiO_2(s) + CO(g) + 6H^+(aq) + 6e^-$

$\Delta G^o_{3+4+10} = +313799.23$ J/mol

$E^o = -\Delta G^o_{3+4+10} / nF = -(+313799.23)/(6 \times 96485) = -0.542$ V

For reaction 5.13

$Si(s) + 6OH^-(aq) \rightarrow SiO_3^{2-}(aq) + 3H_2O + 4e^-$ $\Delta G^o{}_B = +652238.6$ J/mol [9]

$SiC(s) \rightarrow Si(s) + C(s)$ $\Delta G^o = +70850$ J/mol [10]

$SiC(s) + 6OH^-(aq) \rightarrow SiO_3^{2-}(aq) + 3H_2O(l) + C + 4e^-$ $\Delta G^o_{9+10} = +723088.6$ J/mol

$E^o{}_{\mathbf{B}} = -\Delta G^o_{9+10} / nF = -(+723088.6)/(4 \times 96485) = -1.874$ V

For reaction 5.14

$Si(s) + 6OH^-(aq) \rightarrow SiO_3^{2-}(aq) + 3H_2O + 4e^-$ $\Delta G^o{}_B = +652238.6$ J/mol [9]

$SiC(s) \rightarrow Si(s) + C(s)$ $\Delta G^o = +70850$ J/mol [10]

$C(s) + 6OH^-(aq) \rightarrow CO_3^{2-}(aq) + 3H_2O(l) + 4e^-$ $\Delta G^o{}_B = -664783.9$ J/mol [7]

$SiC(s) + 12OH^-(aq) \rightarrow SiO_3^{2-}(aq) + 5H_2O(l) + CO_3^{2-}(aq) + 8e^-$

$\Delta G^o_{7+9+10} = +58304.7$ J/mol

$E^o{}_{\mathbf{B}} = -\Delta G^o_{7+9+10} / nF = -(+58304.7)/(8 \times 96485) = -0.076$ V

For reaction 5.15

$Si(s) + 6OH^-(aq) \rightarrow SiO_3^{2-}(aq) + 3H_2O + 4e^-$ $\Delta G^o{}_B = +652238.6$ J/mol [9]

$SiC(s) \rightarrow Si(s) + C(s)$ $\Delta G^o = +70850$ J/mol [10]

$C(s) + 2OH^-(aq) \rightarrow CO(g) + H_2O(l) + 2e^-$ $\Delta G^o{}_B = -259609.69$ J/mol [8]

$SiC(s) + 8OH^-(aq) \rightarrow SiO_3^{2-}(aq) + 4H_2O(l) + CO(g) + 6e^-$

$\Delta G^o_{8+9+10} = +463478.91$ J/mol

$E^o{}_{\mathbf{B}} = -\Delta G^o_{8+9+10} / nF = -(+463478.91)/(6 \times 96485) = -0.8$ V

APPENDIX B

The results of the surface composition of SSiC with SXPS

Sample	Element	Binding Energy (eV)	Probable Compound(s)
SSiC 1 (Uncorroded)	C	282,9 284,7; 286,2	SiC (59,5%) Adventitious Carbon ; C-(C,H,O) (40,5%)
	O	532,4	Metal Oxides ; O-(C,H)
	Si	100,8 102,5	SiC (90,9%) SiO (9,1%)
SSiC 2 (Corroded)	C	282,9 284,8 ; 286,4	SiC (51,3%) Adventitious Carbon ; C-(C,H,O) (48,7%)
	O	532,6	Metal Oxides ; O-(C,H)
	Si	100,8 102,7	SiC (89,9%) SiO (10,1%)

C – Carbon

O – Oxygen

Si – Silicon

H – Hydrogen

Adventitious carbon is free carbon or carbon bonded with carbon, hydrogen or oxygen.